UC Berkeley
UC Berkeley Electronic Theses and Dissertations

Title
Piezoelectric Micromachined Ultrasonic Transducers for Ultrasonic Fingerprint Sensors

Permalink
https://escholarship.org/uc/item/93c264dx

Author
Jiang, Xiaoyue

Publication Date
2018

Peer reviewed|Thesis/dissertation

Piezoelectric Micromachined Ultrasonic Transducers for Ultrasonic Fingerprint Sensors

by

Xiaoyue Jiang

A dissertation submitted in partial satisfaction of the

requirements for the degree of

Doctor of Philosophy

in

Engineering - Mechanical Engineering

in the

Graduate Division

of the

University of California, Berkeley

Committee in charge:

Professor David A. Horsley, Co-chair
Professor Liwei Lin, Co-chair
Professor Bernhard E. Boser
Professor George C. Johnson

Fall 2018

Piezoelectric Micromachined Ultrasonic Transducers for Ultrasonic Fingerprint Sensors

Copyright 2018

by

Xiaoyue Jiang

Abstract

Piezoelectric Micromachined Ultrasonic Transducers for Ultrasonic Fingerprint Sensors

by

Xiaoyue Jiang

Doctor of Philosophy in Engineering - Mechanical Engineering

University of California, Berkeley

Professor David A. Horsley, Co-chair

Professor Liwei Lin, Co-chair

A variety of physical mechanisms have been exploited to capture electronic images of a human fingerprint, including optical, capacitive, pressure, and acoustic mechanisms. Compared to other technologies, ultrasonic fingerprint sensors have two major advantages (1) they are insensitive to contamination and moisture on the finger (2) they have the ability to measure images at multiple depths hundreds of microns from the sensor surface. With the maturity of the thin film piezoelectric materials technology and MEMS-CMOS eutectic wafer-bonding process, piezoelectric micromachined ultrasonic transducers (PMUTs) arrays with electrical addressing to individual pixel have been proposed and developed for ultrasonic fingerprint sensors.

This research focuses on the modeling and characterization of the PMUT-based ultrasonic fingerprint sensors. First of all, a 51.7% fill-factor, 110×56 rectangular PMUTs array is demonstrated with improved pressure output, receive sensitivity, and image resolution. With a customized CMOS design, time-gated images collected at two imaging depths was demonstrated to construct overlaid patterns separated axially by 127 μm. Using another 65×42 circular PMUTs array ultrasonic fingerprint sensor design, transmit beamforming is implemented. The measured TX pressure output with beamforming is 25 kPa and the 3 dB beam-width is 50 μm, a 1.6 $\times$ increase in pressure and 6.4 $\times$ decrease in beam-width relative to non-beamformed measurements. Beamforming increases the receive voltage by a factor of 1.4 and the SNR by 7 dB. On the other hand, the mode shapes of the dense rectangular PMUTs array with shared mechanical anchors are more compli-

cated than a single-MUT dynamic model. Finite element model was used to model the mode shapes exhibited by the entire array, while experimental measurements of the mode-shape via laser Doppler vibrometry (LDV) was used to compute the volume velocity, which correlates to the measured far field pressure. In order to have an accurate prediction of the 2D near field pressure output from dense transducer arrays, time domain acoustic simulation using k-wave MatLab toolbox and vibration displacement measurements using LDV were utilized. Effects of mechanical crosstalk, acoustic surface waves, and anchor motions were also characterized. To further improve the fingerprint sensors performance, equivalent circuit model of circular PMUTs operating at the same resonant frequency in air is formulated. PMUT displacement is proved to be inversely proportional to the device thickness. Sub-micro thick piezoelectric layer devices were designed and fabricated to demonstrate the thickness scaling benefits.

To my parents: Lian and Yaping

Contents

List of Figures

List of Tables

Acknowledgments

道可道，非常道；名可名，非常名。《道德經》

Words cannot express my gratitude and appreciation of my PhD journey, where I have the luxury of meeting and working with people with different perspectives. I will try my best here to thank my mentors, colleagues, and friends, who have enriched my graduate school life.

Foremost, I would like to thank my research adviser, Prof. David Horsley, for intriguing me with challenging research questions, in-depth technical discussions, and research presentation techniques. I am grateful to Prof. Liwei Lin, my co-adviser, for the support throughout my PhD study. I have also greatly benefited from Prof. Bernhard Boser's input on the ultrasonic fingerprint sensor project. In addition, I would like to express my gratitude to my PhD committee, Prof. George Johnson, Prof. Dorian Liepmann, Prof. Tsu-Jae King Liu, and Prof. Amy Herr, for the valuable feedback. Lastly, I would like to thank Prof. Al Pisano, for starting my PhD journey in MEMS at Berkeley.

No one can do everything. I really appreciate Yipeng Lu, Hao-yen Tang, Julius Tsai, Eldwin Ng, and Mike Daneman for the collaboration on the ultrasonic fingerprint sensor project. I owe my deepest gratitude to Yipeng Lu, who have designed the MEMS for the ultrasonic fingerprint sensor. Meanwhile, I want to thank Guo-Lun Luo, Qi Wang, and Yuri Kusano for the work and input on the thickness optimized PMUT devices, which were fabricated in the UC Berkeley Marvell Nanofabrication Laboratory.

I am particularly grateful for the generous support given by Peter Hartwell. I would also like to offer my thanks to Mei-Lin Chan, Ben Eovino, Nikhil Apte, Lingtao Wang, and Sina Akhbari, for the valuable technical discussions. I would also like to thank the colleagues in MEMS Laboratory at UC Davis for the support and encouragement.

I would like to express my gratitude to Berkeley Sensor and Actuator Center (BSAC) and TDK InvenSense for the project support.

Many thanks to all my friends for the precious time together. Thank you for the journey together, Jing.

My deepest appreciation goes to my family. This thesis is dedicated to my parents, Lian and Yaping.

Chapter 1

Introduction

Micro-electoral-mechanical systems (MEMS) devices can be loosely defined as micro-scale devices and systems that operate mainly via a mechanical or electromechanical means. MEMS devices' performances, including speed, power consumption, and complexity, improve as their size reduces. In addition, the MEMS devices take advantage of the batch fabrication process used in the integrated circuits. This makes MEMS economical, especially for the large demands in the consumer markets. In addition to providing cheap and small form factor alternative solutions, MEMS devices also enabled new applications such as inkjet print heads and digital micro displays.

1.1   Prior Works

With the rapid development of micro-electromechanical systems (MEMS) technology, micromachined ultrasonic transducers (MUTs) based on capacitive (CMUT) and piezoelectric (PMUT) transduction have been demonstrated with significantly reduced device sizes for high resolution applications, low power consumption, and better acoustic impedance matching to the medium [1, 2]. In general, CMUTs suffer from limited vertical deformation, nonlinear drive effects, and high DC bias voltages, but they have high electromechanical coupling factors [3]. With improvements in thin film piezoelectric materials technology, PMUTs are beginning to pose an alternative to CMUTs. The most widely available thin-film piezoelectric materials for PMUTs are lead zirconium titanate (PZT) and aluminum nitride (AlN). PZT has better piezoelectric properties, but it is not CMOS-compatible and may suffer from aging and other material property changes over time [4]. By contrast, AlN is lead-free, has low-temperature ($< 400°C$) deposition, and has demonstrated its stable material properties in the mass production of AlN bulk acoustic-wave (BAW) filters. However, AlN has lower piezoelectric coefficients than PZT.

Fingerprint sensors have become a hot topic in the last few years following the introduction of

a fingerprint sensor in the iPhone 5s in 2013. Many applications in smart phones, such as secure payments and personal health monitoring, lead to a pressing need for improved security without compromised ease-of-use. Fingerprint sensors capture an electronic image of a human fingerprint through various physical mechanisms, including optical, capacitive, pressure, and acoustic mechanisms. Capacitive fingerprint sensors are the standard for identity authentication in numerous applications because of their performance and low cost; the latter is due to the fact that these sensors can be manufactured in a standard integrated circuit manufacturing process.

Ultrasonic fingerprint sensors have many advantages over capacitive sensors, including being insensitive to contamination and moisture on the finger. In addition, fingerprint sensor based on pulse-echo ultrasonic imaging offers the ability to measure images at multiple depths hundreds of microns from the sensor surface [5, 6]. This feature makes the sensor harder to spoof since images can be collected beneath the epidermis and also poses the possibility of placing the sensor beneath the smartphone's glass cover. However, ultrasonic fingerprint sensors previously provided a low resolution or were too difficult to manufacture.

Ultrasonic fingerprint sensor technology has been under investigation for more than a decade, although early systems required mechanical scanning of a single-point ultrasonic transducer [7]. An ultrasonic fingerprint sensor based on a 1-3 piezo-composite array similar to conventional medical ultrasound probes was first demonstrated in 2004 [8], but was incapable of pulse-echo measurement due to the limited bandwidth of the array. Relative to piezo-composite transducers, micromachined ultrasonic transducers (MUTs) are attractive because they can have high bandwidths and, equally important, are well-suited for integration with an application specific integrated circuit (ASIC) for signal processing, enabling them to exceed the price-performance metric of a capacitive sensor.

The first fingerprint sensor based on capacitive micromachined ultrasonic transducers (CMUTs) was presented in 2010 [9]. This sensor used remote electronics to read out a 192-element one-dimensional line-scan array, and mechanical scanning was used to collect a two-dimensional fingerprint image. On the other hand, sensors based on dense 2D MUT arrays require integration with CMOS to enable signal multiplexing to thousands of MUTs in the array. CMUTs have been integrated with CMOS using through-silicon vias (TSVs) and solder-ball flip-chip bonding [10]. However, both TSVs and flip-chip bonding are relatively expensive processes. More importantly, the minimum solder ball diameter is approximately 80 μm [11], making this approach unsuitable for electrical interconnect to individual MUTs in a 500 DPI array, where the pitch between MUTs is 50 μm or less. Previously, a MEMS-CMOS eutectic wafer-bonding process used for high-volume manufacturing of inertial sensors was adapted to produce PMUT arrays, enabling each PMUT to be directly bonded to a dedicated CMOS receive amplifier to minimize electrical parasitics [12]. In an earlier fingerprint sensor designed with this technology, a 17% fill-factor PMUT array achieved 14 kPa peak-to-peak pressure output, 0.6 μV/Pa sensitivity, and 200 μm image resolution [13].

1.2 Dissertation Contributions and Organization

This thesis focuses on the modeling and characterization of ultrasonic fingerprint sensors based on piezoelectric micromachined ultrasonic transducers (PMUTs) . The research of the mechanical aspects of PMUTs based system requires understanding of piezoelectric materials, PMUTs device design, and acoustic performance. Chapter 2 will cover the basic knowledge of thin film piezoelectric material properties, along with their characterization methods. This chapter will also present the analytical modeling of PMUT devices, acoustic impedance, and far field pressure. Chapter 3 will detail the demonstration of a 110×56 rectangular PMUT based ultrasonic fingerprint sensor with 51.7% fill factor. The model and validation of the mechanical and acoustic performance of the individual device and array will be presented. In addition, the axial and transverse image resolution will be characterized. In the end, two time gated images collected at two depths will be demonstrated. Chapter 4 will focus on a 65×42 circular PMUTs based fingerprint sensor with improved performance via transmit beamforming.The improved pressure amplitude, beam width, receive signal, and image contrast will be reviewed. As the fingerprint sensor requires densely packed arrays, the non-idealities and their characterizations will be covered in the next two chapters. Chapter 5 will cover inter-element coupling effects resulting from the sharing of the small eutectic mechanical anchors. The complicated mechanical mode shapes and their influence on the far field pressure will be modeled and measured. As the PMUTs in ultrasonic fingerprint sensors operate with pulsed excitation and images in the near field, more accurate finite element methods (FEM) models and validation methods are required for device understanding and characterization. In chapter 6, time domain acoustic simulation using k-wave MatLab toolbox [14] and measured vibration displacement using LDV were utilized to characterize the 2D pressure output field. Effects of mechanical crosstalk, acoustic surface waves, and anchor motions were also characterized in the LDV measurements of the packaged PMUTs. Chapter 7 discusses further improvements of the individual PMUT's transmit performance. FEM simulation is used to identify that fill factor, area size, and the transducer's peak displacement determine the near field pressure output in pulsed excitation. Through modeling and device fabrication, the displacement of an individual PMUT is proved to inversely scale with the total device thickness. Sub-micro piezoelectric thickness PMUTs were made to further improve the transmit performance of the PMUTs.In the end, the conclusion is offered with some proposed future work.

Chapter 2

Introduction

In this chapter, the thin film piezoelectric material properties and their characterization methods will be introduced. Then an analytical modeling of PMUTs will be presented for an understanding of the important device design parameters. At the end, the acoustic coupling and the classical far field pressure field theories will be reviewed to understand the basic acoustic transducer design.

2.1 Thin Film Piezoelectric Material

2.1.1 Piezoelectric material properties

Bulk piezoelectric materials are commonly used in medical ultrasonic probes. The piezoelectric linear constitutive relations and the bulk material properties have been studied extensively. When measuring thin piezoelectric films on a solid wafer, the observed deformation is constrained by the solid wafer surface. Assuming that the wafer is infinitely stiff, the concept of thin-film piezoelectric coefficients has been developed. The effective $e_{31,f}$ has been introduced as [15].

$$e_{31,f} = \frac{d_{31}}{s_{11}^E + s_{12}^E} = e_{31} - \frac{c_{13}^E}{c_{33}^E}e_{33}, \ where \ |e_{31,f}| > |e_{31}|, \tag{2.1}$$

$$d_{33,f} = \frac{e_{33}}{c_{33}^E} = d_{33} - \frac{2s_{13}^E}{s_{11}^E + s_{12}^E} < d_{33}, \tag{2.2}$$

where $d_{ij}[C/N]$ is the piezoelectric coupling coefficients in Strain-Charge form, $e_{ij}[C/m^2]$ is the piezoelectric coupling coefficients in Stress-Charge form, $c_{ij}^E[N/m^2]$ is the stiffness coefficient matrix with constant electric field, and $s_{ij}^E[m^2/N]$ is the compliance coefficient matrix with constant electric field. In the application of the electric field E_3, the in-plane stress σ_1 and the out-of-plane
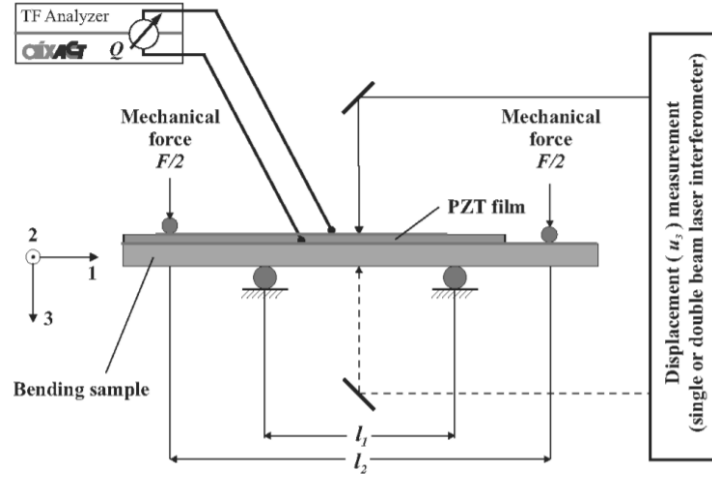
Figure 2.1: Example Four Point Bending Setup [16]

strain ε_3 are induced as

$$\varepsilon_3 = d_{33,f}E_3, \tag{2.3}$$

$$\sigma_1 = -e_{31,f}E_3, \tag{2.4}$$

2.1.2 Thin Film Piezoelectric Material characterizations

To obtain the full piezoelectric coupling coefficients in the bulk piezoelectric materials, different cuts of the samples are required. As mentioned earlier, the most critical coefficient of the film piezoelectric material for MEMS application is $e_{31,f}$. There are several ways to characterize $e_{31,f}$, including four point bending method, inverse Kanno/Muralt method, double beam laser interferometer, and using finite element methods (FEM) simulations.

The four point bending method uses a setup that includes a four-point bending sample holder that allows precise application of an in-plane strain to the film and determine the effective transverse piezoelectric coefficient $e_{31,f}$ by measuring the induced charges [16]. An example setup can be found in Figure 2.1. The $e_{31,f}$ can be calculated as

$$e_{31,f} \cong \frac{Ql_1^2}{4Ahu(1 - v_{Si,f})}, \tag{2.5}$$

where u is the measured displacement, l_1 is the distance between the inner two supports, h is the thickness of the test sample, $v_{Si,f}$ is the Poisson's ratio of the Si substrate, Q is the measured charge, and A is the electrode area.

For the inverse Kanno/Muralt method, the effective transverse piezoelectric coefficient $e_{31,f}$ of piezoelectric films was calculated by measuring the tip displacement δ of unimorph cantilevers with piezoelectric thin films on Si substrates [17, 18]. The corresponding relationships are

$$d_{31} = \frac{1 - \upsilon_p}{1 - \upsilon_s} \frac{h_s^2 E_s \delta}{3 E_p L^2 V}, \tag{2.6}$$

$$as \ e_{31,f} = \frac{d_{31}}{s_{11}^E + s_{12}^E}, \tag{2.7}$$

$$e_{31,f} = \frac{E_s}{1 - \upsilon_s} \frac{h_s^2 \delta}{3 L^2 V}, \tag{2.8}$$

where E_p and E_s are the Young's modulus of the piezoelectric film and the substrate, υ_p and υ_s are the Poisson's ratio of the piezoelectric film and the substrate, h_s and L are the thickness and length of the cantilever test structure, and V is the applied voltage. Note only the Si material property needs to be assumed in Equation 2.8.

The DBLI method is based on that the measured longitudinal effective piezoelectric coefficient, $d_{33,f,meas}$, is related to the true $d_{33,f}$ and the transverse effective piezoelectric coefficient $e_{31,f}$ through the substrate material elastic properties and the ratio of the electrode size to the substrate thickness, as shown in Figure 2.2 [19].By measuring the $d_{33,f,mea}$ with different electrode size over substrate thickness ratio r, the $e_{33,f}$ and $d_{33,f}$ can be extracted as:

$$e_{31,f} = \frac{1}{s_{13,s}} \frac{d_{33,f,meas}(r_1) - d_{33,f,meas}(r_1)}{f(r_1) - f(r_2)} \tag{2.9}$$

$$d_{33,f} = \frac{f(r_2) d_{33,f,meas}(r_1) - f(r_1) d_{33,f,meas}(r_2)}{f(r_1) - f(r_2)} \tag{2.10}$$

where $f(r)$ is the relative magnitudes of the in-plane and out-of-plane stress in the substrate extracted from FEA simulation, which only depends on the Poisson's ratio of the substrate.

Lastly, the $e_{31,f}$ can be be extracted on the designed MEMS structure by comparing FEM simulation results with the measurements assuming different material properties. In the case of PMUTs, resonance frequency and static displacement are the two key parameters that can be used for material property extrapolation.

2.1.3   Figure of Merit

PMUTs operate in a flexural vibration mode, where out-of-plane vibration is excited by in-plane piezoelectric film stress. For this reason, the relevant piezoelectric coefficient is the 31 (transverse) coefficient. The figure of merit (FOM) to compare piezoelectric thin films for different applications
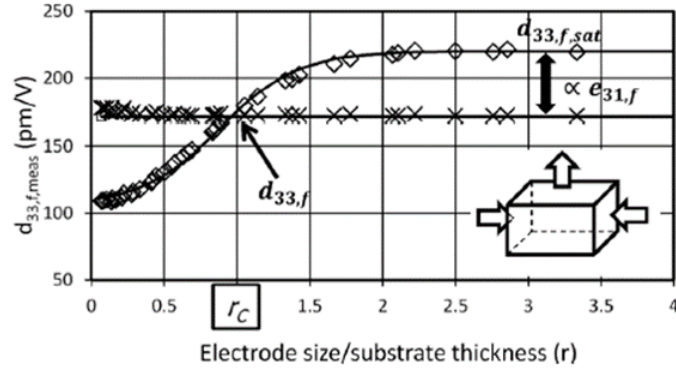
Figure 2.2: Simulated values of $d_{33,f}$ that would be measured by DBLI as a function of the electrode size to substrate thickness ratio, r [19]

can be introduced. The FOMs are $e_{31,f}$ for actuators , $\dfrac{e_{31,f}}{\epsilon_{33}}$ for sensors , and $k_t^2 \propto \dfrac{e_{31,f}^2}{\epsilon_{33}}$ for the electromechanical coupling coefficient [20, 21, 22]. Using the published material properties of PZT ($e_{31,f} = -14.7\ C/m^2, \epsilon_{33} = 1200$) and AlN ($e_{31,f} = -1.08\ C/m^2, \epsilon_{33} = 10.5$) , the electromechanical coupling coefficient of PZT is only about 50% greater than that of AlN, despite the fact that the piezoelectric coefficient for PZT is 13 times higher than that of AlN. Based on the value from [15], AlN, and PZT thin film can be compared in Table.2.1. Compared to AlN, PZT has about $14\times$ larger $e_{31,f}$ and $100\times$ larger ϵ_{33}, resulting in a $14\times$ better transmit performance, $2\times$ better pulse echo performance, and $8\times$ worse receive performance.

FOM	AlN	PZT
$-e_{31,f}$	1.05	14.7
ϵ_{33}	11	1200
$-e_{31,f}/\epsilon_{33}$	0.095	0.012
$e_{31,f}^2/\epsilon_{33}$	0.1	0.18

Table 2.1: Comparison of PZT and AlN based on different figure of merits (FOMs)

2.2 PMUTs Analytical Model

PMUTs are flexural piezoelectric resonators, whose modeling has been thoroughly explained in [23]. In this chapter, the key parameters will be reviewed. Then a model to compare the circular PMUTs' performance at same resonant frequency in air, which leads indirectly to their resonant frequency in acoustic medium, will be detailed.
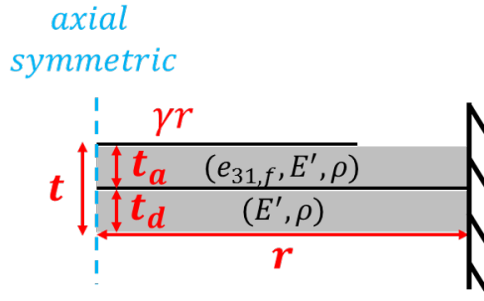
Figure 2.3: Schematic of the modeled circular PMUT

The equivalent circuit of PMUTs include electrical, mechanical, and acoustical domain, as shown in Figure 2.4. The state variables are electrical voltage V and current i_m in the electrical domain, force F and peak displacement w_p in the mechanical domain, as well as pressure p and volume velocity V_v in the acoustical domain. The electrical domain is coupled to mechanical domain via electromechanical coupling constant η, and output force in mechanical domain is converted to an output pressure by dividing by the effective area A_{eff}.

The modeling of a PMUT composed of a single layer of piezoelectric film, a uni-morph PMUT, is detailed in this section. The device and elastic layers are assumed to have the same material properties. As shown in 2.3, assume that the total thickness of the film is t, the piezoelectric layer thickness is t_a, and the elastic layer thickness is t_d, where the thickness ratio is defined as $\beta = t_a/t_d$. The electrode thickness is considered to be thin enough to be neglected here. In the mechanical domain, PMUT is a 2nd order linear system, the key parameters for PMUT performance are resonant frequency f, static displacement w_s, and peak displacement w_p. Based on the equivalent circuit model, $w_s = \eta/k$ and $w_p = Q\eta/k$, where k is the stiffness of the membrane and Q is the quality factor of the system. In the electrical domain, the capacitance C_0 is

$$C_0 = \frac{\varepsilon(\gamma r)^2}{t} \tag{2.11}$$

where ε is the dielectric constant of the piezoelectric material, γ is the electrode coverage, r is the radius of the membrane, and t is the thickness of the piezoelectric material. In the mechanical domain, the flexural rigidity of the membrane D is

$$D = \frac{1}{12}E't^3 \tag{2.12}$$

where E' is the plate modulus defined as

$$E' = \frac{E}{1 - \upsilon^2} \tag{2.13}$$

where E and υ are the Young's modulus and Poisson's ratio of the material. The mass per unit area of the plate μ is

$$\mu = \rho t \tag{2.14}$$
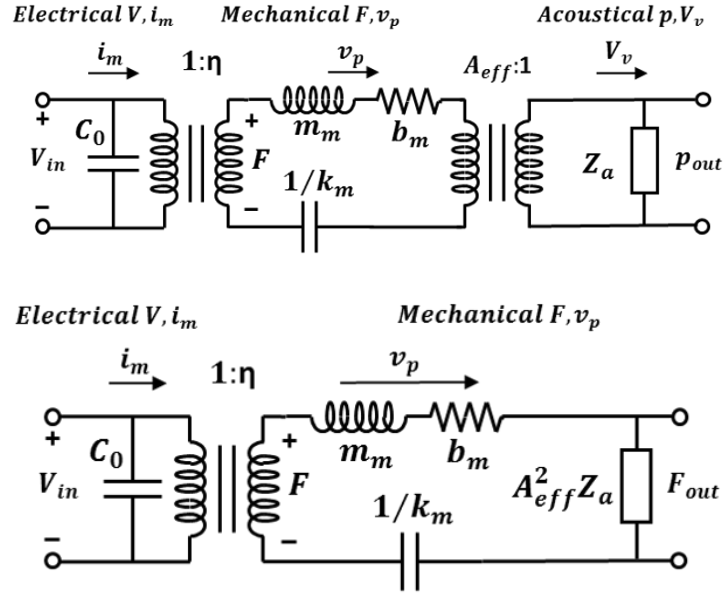
Figure 2.4: PMUT equivalent circuit model

where ρ is the density of the material. The natural frequency of a circular plate f is [23]

$$f = \frac{10.327}{2\pi r^2}\sqrt{\frac{D}{\mu}} = \frac{10.327}{2\pi}\sqrt{\frac{E'}{3\rho}}\frac{t}{r^2} \tag{2.15}$$

Based on this relationship, the ratio of t/r^2 is fixed for a given frequency and should be accounted for in the modeling of the PMUT's displacements. As for PMUTs, the electromechanical coupling constant η is determined by the distance from the middle of the piezoelectric layer to the neutral axis z_p and piezoelectric integral I_{piezo}

$$\eta = \frac{1}{2}e_{31,f}z_p I_{piezo}, \tag{2.16}$$

where $I_{piezo} = 8\pi\gamma^2(\gamma^2 - 1)$ [23] and $z_p = t_d/2 = t/(2(1+\beta))$. The stiffness k of the membrane is

$$k = 64\frac{\pi D}{3r^2}, \tag{2.17}$$

Putting all these together for the transmit performance, the static displacement per voltage input is

$$\frac{w_s}{V_{in}} = \frac{\eta}{k} = \frac{9}{32\sqrt{3}}\frac{10.327}{\pi}[\sqrt{\frac{1}{\rho E'}}e_{31,f}]\frac{\gamma^2(\gamma^2 - 1)}{(1+\beta)t}\frac{1}{f} \tag{2.18}$$

Based on Equation 2.18, static displacement is related to the material properties, electrode coverage, thickness, thickness ratio, and frequency. Moreover, static displacement inversely scales with device thickness and frequency.

Defining kd^2 to quantify the efficiency of the electromechanical coupling for flexural mode resonators, as $\dfrac{\eta^2}{k} << C_0$, we have

$$kd^2 = \frac{\dfrac{\eta^2}{k}}{C_0 + \dfrac{\eta^2}{k}} \approx \frac{\dfrac{\eta^2}{k}}{C_0} = \frac{9}{(2(1+\beta))^2} \frac{(\gamma^2(\gamma^2-1))^2}{\gamma^2} \frac{e_{31,f}^2}{E'\varepsilon} \tag{2.19}$$

The kd^2 is about 8% of $k_{31}^2 = \dfrac{e_{31,f}^2}{E'\varepsilon}$ for a device with optimized electrode coverage (60%) on a equal piezoelectric and elastic thickness stack.

2.3 Acoustic Impedance

The acoustic impedance, defined as the ratio of acoustic pressure p to the volume velocity V_v, has been introduced to model the acoustic wave propagated into the fluid from the acoustic source:

$$Z_a = \frac{p}{V_v} = \frac{\rho_0 c}{A_{eff}}[r_r + jx_r] \tag{2.20}$$

where p is the generated pressure, ρ_0 and c are the density and speed of sound of the medium, and A_{eff} is the effective area based on the device's mode shape. For a circular piston acoustic source, the unit-less specific resistance r_r and reactance x_r components can be simplified as

$$r_r(2ka) = 1 - \frac{2J_1(2ka)}{2ka} \approx \frac{1}{2}(ka)^2 \; (for\ ka << 1) \; or \; \approx 1 \; (for\ ka >> 1), \tag{2.21}$$

$$x_r(2ka) = \frac{2H_1(2ka)}{2ka} \approx \frac{8}{3\pi}(ka) \; (for\ ka << 1) \; or \; \approx 2ka/\pi \; (for\ ka >> 1) \tag{2.22}$$

where $J_1(x)$ is the first order Bessel function and $H_1(x)$ is the first order Struve function. Using effective area, we can convert the output pressure and volume velocity to the mechanical domain as output force and particle velocity as shown in Figure 2.4, where

$$\frac{F_{out}}{v_p} = \rho_0 c A_{eff}[r_r + jx_r] \tag{2.23}$$

The reactive component x_r of the acoustic impedance is an inertial term that represents an additional acoustic mass m_r

$$m_r = \frac{F_{out}}{\dot{v}_p} = \rho_0 c A_{eff} \frac{x_r}{w} \tag{2.24}$$

Meanwhile, the specific acoustic impedance that relates pressure and particle velocity can be defined as [24]

$$z_a = \frac{p}{v} = Z_a \times A_{eff} = \rho_0 c[r_r + jx_r] \tag{2.25}$$

Most of the time, the acoustic coupling of a piston with a uniform displacement at the surface is discussed. However, for a flexural mode acoustic device, the non-uniform displacement at the interface of the membrane and the acoustic medium needs to be accounted for. For a circular flexural mode MUT, the average displacement is about 1/3 of the peak displacement w_p. Therefore, the average pressure output at the transducer surface operating at frequency f can be modeled as

$$p_{av} = z_a v_p/3 = z_a(2\pi f)w_p/3 \tag{2.26}$$

2.4 Far Field Pressure

The classical far field pressure $p_{ax}(\theta, r)$ at a distance r from a single circular flexural mode acoustic source with radius a is

$$p_{ax}(\theta, r) = jp_{av}D(\theta)\frac{R_0}{r}e^{j(2\pi f - kr)}e^{-\alpha r} = jp_{av}D(\theta)\frac{A}{\lambda r}e^{j(2\pi f - kr)}e^{-\alpha r} \tag{2.27}$$

$$D(\theta) = \frac{48J_3(kasin\theta)}{(kasin\theta)^3} \tag{2.28}$$

where A and $D(\theta)$ are the area and the directivity of the transducer, $\lambda = c/f$ is the wavelength in the medium, R_0 is the Rayleigh distance ($R_0 = \frac{A}{\lambda}$), $k = \frac{2\pi}{\lambda}$ is the wavenumber, and α is the acoustic attenuation in the medium expressed in $[Nepers\ per\ cm]$ and is converted to dB/cm by multiplying with 8.686, namely $\alpha[Np/cm] = \hat{\alpha}[dB/cm]/8.686$.

This analytical model assumes continuous wave operation in the far field. As the MUTs device size and package height become comparable to the wavelength, the pressure field cannot be captured by the classical pressure analytical model accurately. In this case, the classical model only provides an intuitive understanding of the factors impacting the pressure output. In these cases, finite element methods are needed to accurately predict the acoustic performance. There are several FEM simulation tools available including OnScale (previously PZFlex), COMSOL Multiphysics, and k-Wave MATLAB Toolbox. The OnScale offers a relatively fast simulation of the device performance and the generated acoustic field, where the interaction of the membrane and acoustic field can be captured. COMSOL Multiphysics is relative slow for large array simulation, but is capable of modeling both the device and acoustic performance. The k-Wave MATLAB Toolbox offers a relatively fast acoustic simulation with pre-described transducer displacements, however the device performance as well as the device/acoustic interactions cannot be captured.

2.5   MUTs Array Mechanical Crosstalk

In this section, the major mechanical crosstalk will be reviewed to advice MUT array design. The two major mechanical crosstalk mechanisms are at the membrane / medium interface as well as in the substrate. At the fluid-solid interface, leaky Rayleigh and Scholte wave has been identified [25, 26]. On the other hand, Rayleigh waves below the MUT structure have also be found [27].These mechanical crosstalk mechanisms will lead to non-ideal beam pattern and extended ringdown time in pulse-echo operations.

Chapter 3

Monolithic Ultrasound Fingerprint Sensor

3.1 Introduction

A monolithic ultrasonic fingerprint sensor based on an 8×24 AlN piezoelectric micromachined ultrasonic transducer (PMUT) array with 254-DPI pitch has recently been demonstrated [28, 13]. However, the standard for fingerprint sensors in consumer electronics is 500 DPI, requiring a dramatic reduction in the PMUT size to < 50 μm, risking both low acoustic output and reduced fill-factor because the active acoustic area shrinks while the area needed for anchors and interconnect does not. This section presents a systematic design study of the individual AlN PMUT and array parameters to resolve these issues. In this study, a 51.7% fill-factor, 591 × 438 DPI, 110 × 56 array of rectangular PMUTs is demonstrated, an increase of 140% pressure output per input voltage along with over 200% in sensitivity and image resolution.

3.2 Materials and Methods

A cross-section schematic of an individual PMUT is shown along with photographs of the 110× 56 sensor chip in Figure 3.1a. Each PMUT is a piezoelectric unimorph composed of 1 μm thick AlN sandwiched between 300 nm Al and 200 nm Mo electrodes on a single crystal silicon layer with 1.6 μm nominal thickness (Figure 3.1b). Al Ge eutectic bonds on SiO_2 standoffs provide the mechanical anchor and electrical contact to the PMUT [12]. The deformation of a PMUT with an external electrical field applied to the AlN is shown in Figure 3.1c. The PMUTs are formed on an SOI MEMS wafer that is bonded to a CMOS wafer that provides the signal processing electronics, which includes the 24V charge pump, high voltage transmit amplifiers, low voltage receive amplifiers and multiplexing circuitry. Details regarding the design of the signal processing circuitry are provided in [29]. Following CMOS and MEMS wafer bonding, the PMUTs are

released by a through wafer DRIE etch that removes the MEMS handle wafer in a 4.6mm by 3.2 mm region at the center of each 5.4 by 4.6 mm die. Two 110×56 element array designs, composed of 35 μm diameter circular and $30\mu m \times 43\mu m$ rectangular PMUTs, were fabricated. The optical images in Figure 3.1d show the layout of the rectangular and circular PMUT arrays. Each of the 6,160 PMUTs in the array has a dedicated receive (RX) amplifier that is connected to the Al bottom electrode during the receive phase. The 56 PMUTs in each column share a common Mo top electrode that is connected to a 24V transmit amplifier (TX) during the transmit phase. To protect the RX amplifier from the high voltage signal, a TX/RX switch connects each bottom electrode to ground (GND) during the transmit phase.

3.3 Individual PMUT Design

The electrical-mechanical-acoustic equivalent circuit model for the PMUT that takes account of the different material properties of the thin films, shown in Figure 3.2a, is used to understand the resonant frequency in air and in fluid, peak velocity, and peak pressure at the center of the PMUT [2, 20]. In the mechanical domain, equivalent circuit parameters are derived to represent the mass m_m and stiffness k_m for a particular vibration mode. The mechanical parameters, force F and velocity v_P (measured at the center of the PMUT), can be converted to the electrical domain using the electromechanical coupling constant η. The output force is converted to an output pressure by dividing by the effective surface area A_{eff}, which is one-third of the total area for a circular PMUT. In the acoustic domain, the acoustic impedance Z_a relates the acoustic pressure P to the volume velocity V_v as $F = Z_a V_v$.

The parameters of the equivalent circuit model are derived as follows. A schematic and SEM cross-section of the PMUT are shown in 3.2b. While the Al bottom electrode does not span the entire PMUT surface, this layer is thin and the Young's Modulus of Al is low relative to that of the other (Si, Mo, AlN) layers, so we neglect it in the following derivations. For a unimorph PMUT composed of three layers, the neutral axis for the PMUT laminate, shown in Figure 3.2b, can be calculated as [2]

$$z_{NA} = \frac{\sum_{n=1}^{3} t_n z_n E'_n}{\sum_{n=1}^{3} t_n E'_n}, \tag{3.1}$$

where n is the layer index (Si, Mo, AlN), $E'_n = \dfrac{E_n}{1 - v_n^2}$ is the plate modulus, E_n and v_n are the Young's modulus and Poisson's ratio of each layer, z_n is the distance between the layer's middle plane to the bottom of the laminate, and t_n is the layer thickness. The mass per unit area μ is [2]

$$\mu = \sum_{n=1}^{3} t_n \rho_n, \tag{3.2}$$
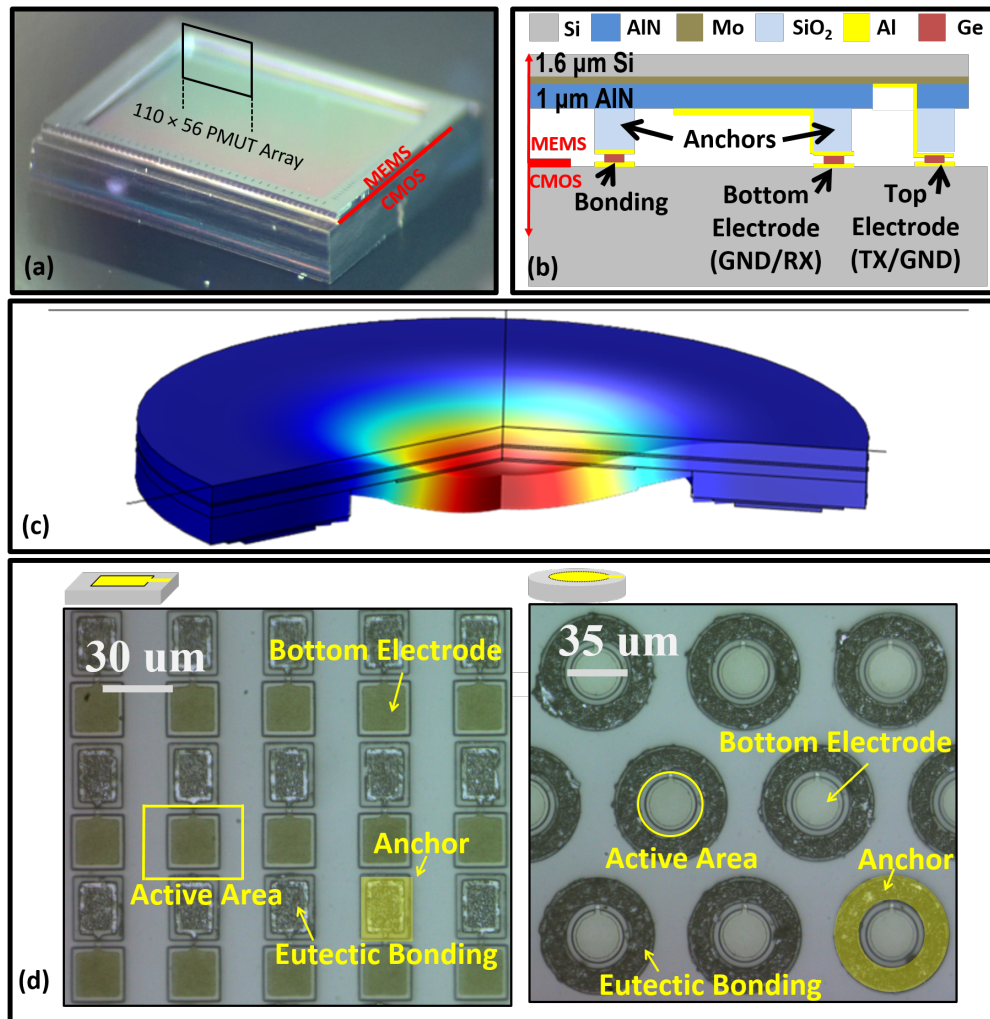
Figure 3.1: (a) Photograph of the sensor. The 110x56 PMUT array is located in the 4.64 mm by 3.36 mm recessed region in the center of the die. (b) PMUT cross-section schematic. c) FEM simulated mode shape of a circular PMUT with an applied electric field across the AlN piezoelectric thin film. d) Optical images of the two PMUT arrays after debonding from the CMOS wafer. In the rectangular design (left), a single Al-Ge anchor (highlighted in yellow) mechanically isolates PMUTs in adjacent rows, while PMUTs in adjacent columns are not mechanically isolated. The circular design (right) sacrifices fill factor for more anchor area and increased spacing between the Al-Ge bonding rings.

where ρ_n is the density of the nth layer. Meanwhile, the flexural rigidity D of a laminate is defined as [30]

$$D = \frac{1}{3}\sum_{n=1}^{3} E'_n(\hat{h}_n^3 - \hat{h}_{n-1}^3), \tag{3.3}$$

where $\hat{h}_n = h_n - z_{NA}$ is the distance between the top the nth layer to the neutral axis.

Assuming a circular plate vibrating in the first mode, the modal stiffness, modal mass, and electromechanical coupling constant are given by

$$k_m = \frac{64\pi D}{3a^2}, \tag{3.4}$$

$$m_m = \frac{\pi a^2 \mu}{5}, \tag{3.5}$$

$$\eta = 4\pi\gamma^2(\gamma^2 - 1)e_{31,f}\hat{z}_p, \tag{3.6}$$

where a is the radius of the PMUT, γ is the ratio of the Al bottom electrode radius to the PMUT radius, $e_{31,f} = 1.08\ C/m^2$ is the effective thin-film piezoelectric coefficient of AlN [31], and $\hat{z}_p$ is the distance from the middle of the piezoelectric layer to the neutral axis. In this chapter, we use the velocity at the center of the PMUT as the mechanical velocity variable because this value is measurable in experiments. In other works, the average velocity $\hat{v} = v_P/3$ is often chosen, a choice that yields $\hat{k}_m = 9k_m$ and $\hat{m}_m = 9m_m$, values that are consistent with Mason's approach [32]. In the acoustic domain, the acoustic impedance Z_a for a clamped radiator can be found as [33]

$$Z_a = \frac{\rho c}{A_{eff}}(r_r + jx_r) \tag{3.7}$$

where r_r and x_r are the resistive and inductive acoustic terms, respectively. The imaginary part of the acoustic impedance behaves as a mass m_a added to the PMUT mass in the mechanical domain.

Circular PMUTs with dimensions from 35 μm to 70 μm were modeled, fabricated, and characterized. For a unimorph PMUT with total thickness t and characteristic length l (diameter or side length), the resonant frequency of the fundamental flexural vibration mode in air is given by

$$f_{0,air} = \sqrt{\frac{k_m}{m_m}} \propto \frac{t}{l^2} \tag{3.8}$$

The resonant frequency of a PMUT immersed in fluid can be estimated from [34]

$$\frac{f_{0,fluid}}{f_{0,air}} \approx \frac{m_m}{m_m + m_a} \approx 1/\sqrt{1 + 0.344\frac{\rho_{0,fluid}l}{\mu}} \tag{3.9}$$
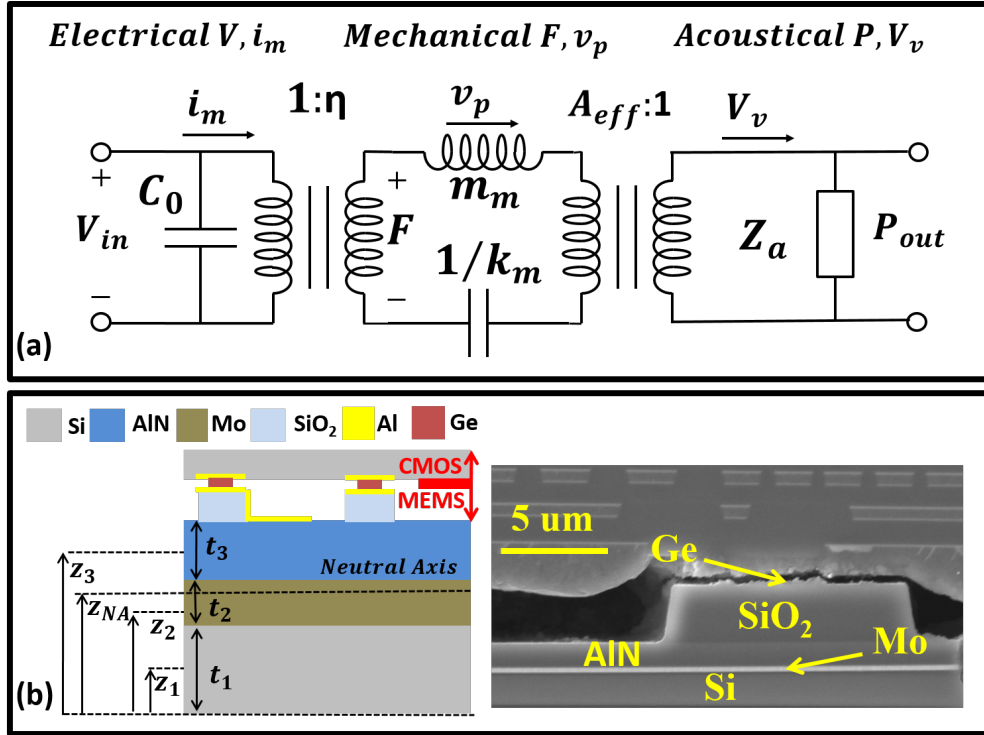
Figure 3.2: a) Electrical-mechanical-acoustic model. Voltage V and current i_m, force F and velocity at the center of the PMUT v_P, and pressure P and volume velocity V_v are the variables for the electrical, mechanical, and acoustical domains, respectively. b) Schematics (left) and SEM image (right) of a PMUT cross-section. The Ge bond in the SEM image was broken during sample preparation.

where $\rho_{0,fluid}$ is the fluid's density. The resonant frequencies predicted by (8) and (9) agree well with resonant frequencies from a finite element method (FEM) model of the PMUT in air and in the non-conducting fluid Fluorinert FC 70 (COMSOL Multiphysics), as shown in Figure 3.3a. The results show that the first resonance frequency $f_{0,fluid}$ of a PMUT immersed in a fluid scales as $\frac{1}{l^2}$, as predicted by the analytical models. Meanwhile, the displacement at the center of the PMUT d_p is given as [35]

$$d_p = Qd_s \propto \frac{e_{31,f}z_nBW}{Df_0} \propto \frac{l^2}{t^4} \tag{3.10}$$

where Q is the quality factor, d_s is the static displacement, and BW is the 3 dB bandwidth of the PMUT. The velocity at the membrane center is

$$v_p = 2\pi f_{0,fluid}d_p \propto \frac{1}{t^3} \tag{3.11}$$

while Equation 3.11 suggests that the velocity should be independent of diameter, and the calculated velocity, shown in Figure 3.3a, shows that the velocity increases by 20% with a 200% increase in diameter.

Lastly, the pressure output scales with the effective area, velocity, and acoustic impedance as

$$P_p = Z_a v_p A_{eff} \tag{3.12}$$

The resistive and inductive acoustic impedance terms are functions of the product of the wave number k and radius a, shown in Figure 3.3b. For an individual PMUT with 1 μm AlN and a 1.6 μm silicon device layer, when the diameter is doubled, the output pressure and peak velocity increase by less than 25%, while the resonant frequency in fluid decreases by 75%.

3.4 Array Design

On an individual basis, there is little difference between the circular and rectangular PMUTs when designing for output pressure. However, when individual PMUTs are arranged into an array, scaling the PMUT causes the active acoustic area to shrink while the area needed for anchors and interconnects does not. Defining the fill factor F to quantify the active acoustic area and comparing designs that can achieve a 50 μm pitch, a 35 μm circular PMUT results in a 17.6% fill-factor, while a 30 $\mu m \times$ 43 μm rectangular PMUT results in a 51.7% fill-factor, a factor of three better. A simple model for the ideal surface pressure generated by a surface oscillating with amplitude d_p at frequency f_0 is given as [13]

$$P = (2\pi f_0 d_p) Z_a A_{eff} \sqrt{F} \tag{3.13}$$

where F is the fill factor of the array. Figure 3.3c shows the best possible fill factor calculated for PMUTs with different sizes and the computed surface pressure based on simulated peak displacement. The calculated pressure output suggests that the rectangular PMUT array design can achieve twice the pressure output of the circular PMUT array.

For pulse echo based ultrasound imaging, lateral resolution depends on the beam width, while the axial resolution is determined by the product of the wavelength and number of cycles in the transmitted pulse [36]. The total pressure output at a point of interest is the superposition of the pressure output from all the PMUTs [37],

$$P_{tot} = \sum \frac{P^{av}}{r_i} \frac{ka^2}{2} D_i(\theta_i) e^{-jkr_i} \phi(t) \tag{3.14}$$

$$D_i(\theta_i) = \frac{48 J_3(kasin\theta_i)}{(kasin\theta_i)^3} \tag{3.15}$$

where P^{av} is the average output pressure, $D_i(\theta_i)$ is the directivity, $\phi(t)$ is the normalized pulse signal, and θ_i and r_i are the angle and radial distance between the PMUT and the point of interest. The schematic of the superposition of the pressure outputs from the PMUT array is shown in Figure 3.4a. In experiments, the PMUTs are covered by a 250 μm thick layer of poly-dimethylsiloxane
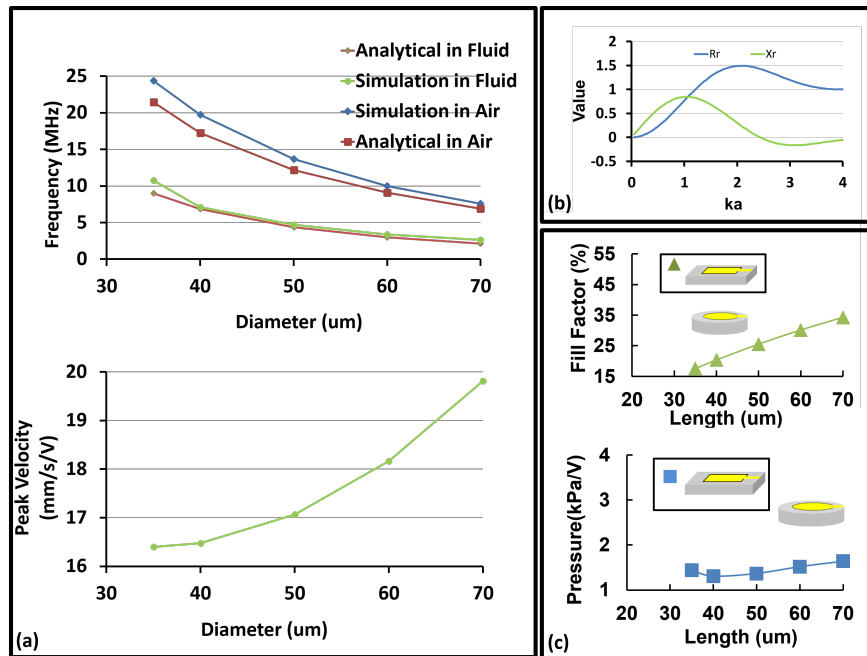
Figure 3.3: a) (Top) Frequency response in air and fluid from the simulation and analytical solution (Bottom) Peak velocity from the analytical solution. b) The resistive r_r and inductive x_r terms in the acoustic radiation impedance plotted versus ka. c) Fill-factor (top) and computed pressure output (bottom) versus PMUT size.

(PDMS) (Sylgard 184 Dow Corning, Midland, MI, USA), and the speed of sound of PDMS ($c = 1000\ m/s$) is used to calculate the wave number in the model, $k = 2\pi f/c \approx 10^5 m^{-1}$ at 16 MHz. The PMUTs in each column of the array share a common top electrode, which is excited with the transmit voltage. Because the column length in the vertical (y) axis is much greater than its width in the horizontal (x) axis (3.2 mm vs. 70 microns/column), the x-axis beam width is of most significance. Therefore, the expected beam width in x-direction at the imaging plane (which is the surface of the PDMS layer), 250 μm above the transducer array, is calculated for a column of PMUTs operating in PDMS with the expected frequencies for seven PMUT diameters ranging from 25 to 70 μm, as shown in Figure 3.4a. As the frequency increases, the beam width decreases dramatically, leading to better lateral resolution. Beam-width calculations were performed for single column excitation, as well as for cases where three columns and five columns are transmitting together. As shown in Figure 3.4b, the increased aperture when transmitting with three columns and five columns without beamforming results in greater resolution. The calculated beam width for this design at 16 MHz is 104 μm with three columns transmitting and 84 μm with five columns transmitting.
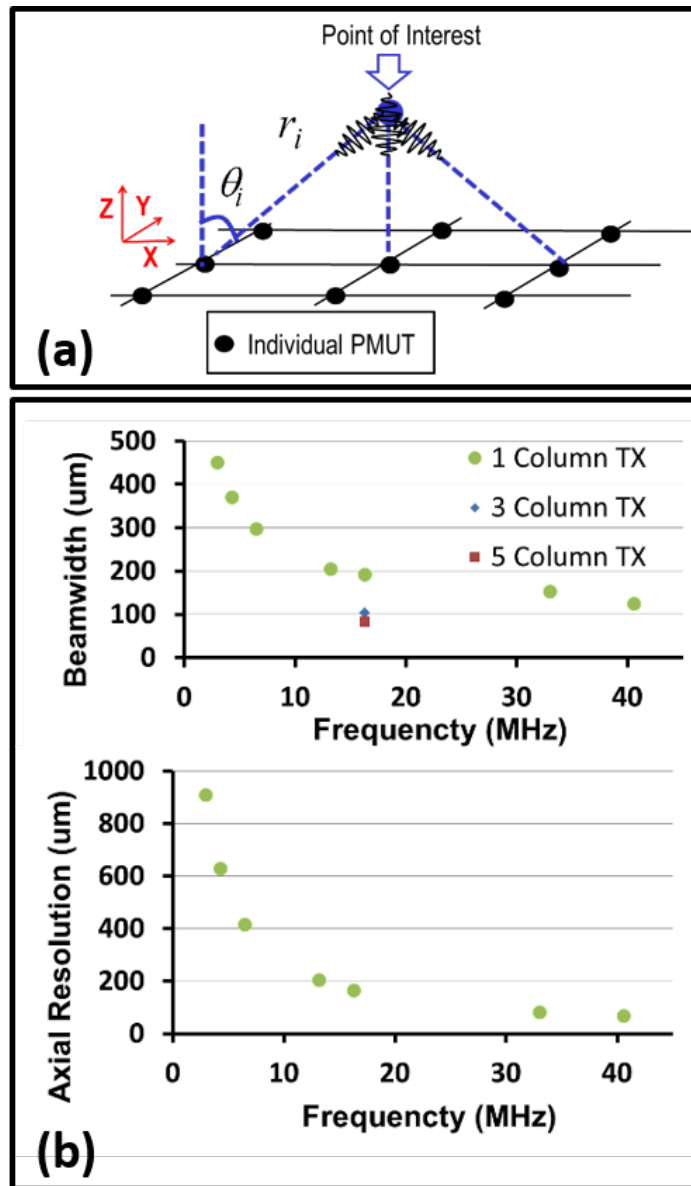
Figure 3.4: a) Schematic of the superposition of the pulsed pressure outputs from the excited PMUTs in the array. b) Beam width (top) and axial resolution (bottom) versus the operating frequency of PMUT in fluid. Beam width calculations were performed when a single column is used to transmit, as well as when three columns and five columns are used.

3.5 Results

Circular PMUTs with five different diameters ranging from 35 to 70 μm were fabricated and measured in air and fluid (Fluorinert FC-70, 3M) using a Laser Doppler Vibrometer (LDV, OFV-5000, Polytec, Inc., Campbell CA, USA). The measured frequencies in air and fluid are in good agreement with the predictions from models, where $f_{0,air}$ scales as $1/l^2$, as shown in Figure 3.5a. The measured displacement at resonance in air, when divided by the measured quality factor, yields a normalized displacement that can be compared with the static displacement d_s calculated from the analytical solution in Figure 3.5a. However, the static displacement d_s for a 35 μm PMUT is two times higher than the predicted value. As shown in 3.5b, the measured peak displacement d_p for circular PMUTs with five different diameters is well predicted by the product of the static displacement d_s and the estimated quality factor. The measured displacement d_p scales as l^2, in good agreement with the model in Equation 3.10.

To quantify the die to die variability, five chips selected from locations across a 200 mm wafer were characterized, and the frequency and peak displacement response in air were recorded. The die-to-die variation in resonant frequency was small, varying by approximately 4%. However, the displacement variation was much greater, with an approximately 20% die-to-die difference in the peak amplitude observed for 50 μm PMUTs. Some of the amplitude variation may be measurement error due to imperfect placement of the LDV laser spot. Cross-section SEM images revealed the Si elastic layer of the PMUT varied by approximately 10% from die to die. Based on Equation 3.8 and Equation 3.10 where $f_0 \propto t$ and $d_p \propto 1/t^4$, the maximum frequency difference due to Si thickness variation is calculated to be 5%, while the amplitude variation is 30%. As a result, the frequency and peak displacement variations can be mostly attributed to Si layer thickness variation.

Acoustic tests were conducted with the PMUT array immersed in fluid with a 40 μm diameter needle hydrophone (Precision Acoustics, Inc.) used to measure the pressure output. As shown in Figure 3.1d., the $30\mu m \times 40\mu m$ rectangular PMUTs were on a $43\mu m \times 58\mu m$ grid, while the 35 μm diameter circular PMUTs were on a $70\mu m \times 80\mu m$ grid. Driving a single column of PMUTs with two 24 V cycles at 14 MHz resulted in 9.4 kPa for the rectangular design measured with the hydrophone 220 μm away from the PMUT chip and 1.62 kPa for the circular design measured with the hydrophone at a 400 μm distance, as shown in Figure 3.5c. These pressure measurements correspond to acoustic surface pressures of 70.8 kPa and 41.9 kPa for the rectangular and circular designs, respectively. This 1.7 factor of difference in the surface pressure agrees with the calculation from Equation 3.13, as the two PMUT designs have similar amplitude responses but differ primarily in that the rectangular design has a 3 $\times$ higher fill factor. The measured pressures are also in good agreement with the modeled pressure calculated from the measured displacement and frequency. The pressure variation due to die-to-die differences is estimated to be less than 50%, while the pressure was measured to vary by only 20% when the hydrophone distance was changed by 200 μm, both of which are relatively small compared to the measured difference in

output pressure of the two designs.

The beam width was measured by laterally translating the hydrophone at a distance of 500 μm away from the PMUT chip. The measured pressure profile, shown in Figure 3.5d, shows that the 3dB beam-width is 200 μm and 150 μm when transmitting with one column and three columns, respectively. The measured beam-width is in reasonable agreement with the analytical calculation from Equation 3.14, with differences resulting from the physical size of the hydrophone needle and errors in the tilt and positioning of the array.

The rectangular PMUT array demonstrated to have the best performance was further characterized to understand its sensitivity, electromechanical coupling coefficient k_t^2, and insertion loss. Based on the equivalent circuit model in Figure 3.6a, the receiving sensitivity S_{RX} is

$$S_{RX} = \frac{V_{RX}}{P_{RX}} = \frac{GA_{eff}}{\eta} \frac{\eta^2 Z_{ele}}{\eta^2 Z_{ele} + Z_{tot}} \tag{3.16}$$

where V_{RX} and P_{RX} are the received voltage and pressure on the PMUT surface, G is the gain of the front-end amplifier, Z_{ele} is the electrical impedance of the PMUT, and Z_{tot} is the sum of the mechanical and acoustic impedance of the PMUT. Pulse echo experiments were conducted with the chip packaged with a 250 μm thick layer of PDMS and an imaging phantom placed on top of the PDMS layer. Using the acoustic pressure output measured with the hydrophone together with the received signal amplitude from pulse-echo measurements, the pressure sensitivity was determined to be 2 mV/kPa, which agrees with the sensitivity computed from Equation 3.16. The electromechanical coupling coefficient k_t^2 is estimated to be 0.3% from [34]:

$$k_t^2 \cong \frac{\pi^2 \eta^2}{8 k_m C_0} \tag{3.17}$$

where $\eta = k d_s$ is the electromechanical coupling, while k_m and C_0 are the mechanical stiffness and electrical capacitance of the PMUT, respectively. Considering the partial electrode coverage of the AlN thin film and that the AlN thickness is only 40% of the entire device thickness, the calculated k_t^2 is consistent with the value calculated from [20, 38] for an AlN piezoelectric thin film (k_t^2=1.49%). The array insertion loss was measured by exciting a column of PMUTs with a 2 cycle 24 V_{pp} 14 MHz pulse and measuring the voltage from the reflected echo. The measured insertion loss is 90 dB from the transmit voltage and receive voltage, which includes approximately 8 dB of the spreading and absorption loss over the 500 μm round-trip path. The absorption coefficient of PDMS is 16 dB/cm or 0.8 dB for the 500 μm round-trip, much less than the spreading loss.

Axial and transverse image resolution experiments were conducted using two different phantoms. In each experiment, pulse-echo measurements are collected from each of the 110 columns in sequence, with a complete image formed in 2.6 ms. In each column's TX cycle, five adjacent columns (N-2, N-1, N, N+1, N+2) of 56 PMUTs are excited without beamforming, and the center column (N) is used as receivers. Figure 3.6b shows a 2D pulse-echo ultrasonic image of a fingerprint sensor resolution test pattern fabricated by the National Institute of Standards and Technology
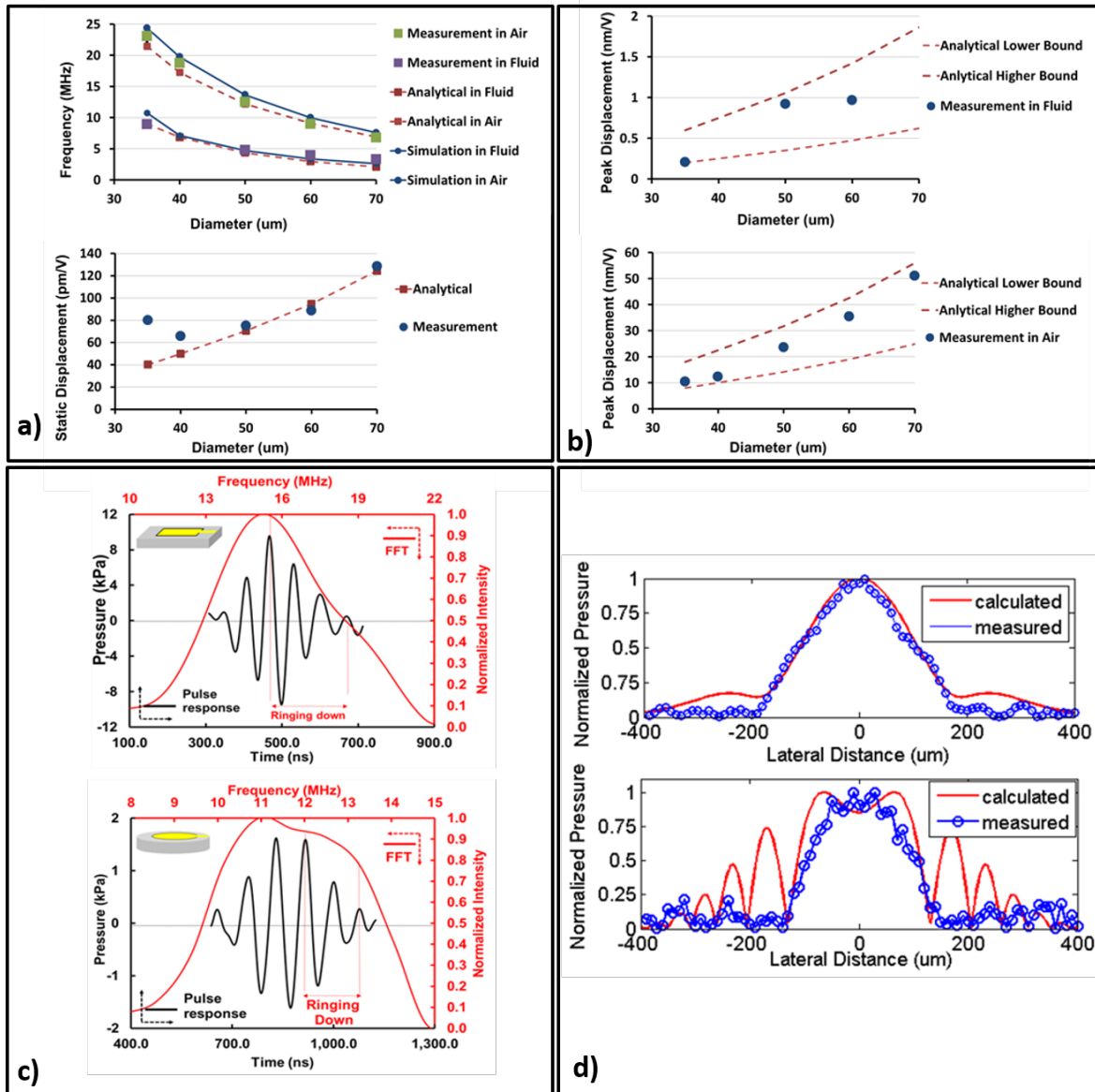
Figure 3.5: a) Modeled and measured resonance frequency in air and fluid (top). Modeled and measured static displacement (bottom). b) Modeled and measured peak displacement in fluid (top) and in air (bottom) c) Pressure output of the rectangular (top) and circular (bottom) PMUT arrays measured with a hydrophone 220 μm and 400 μm from the PMUT array. Black: time-domain; Red: FFT. d) The normalized pressure field at a 500 μm distance from the PMUT array measured by translating the hydrophone along the y-axis when transmitting with one column (top) and three columns (bottom).

(NIST), (Figure 3.6b), demonstrating a 5:1 contrast ratio over the 4.6 mm $\times$ 3.2 mm ultrasound image. A separate test, not shown here, characterized the lateral resolution to be 80 μm, consistent with the 80 μm beam width computed using the acoustic model. The discontinuous image pattern is due to a non-flat PDMS surface. To demonstrate the axial resolution, a phantom was constructed consisting of two overlaid patterns separated axially by 127 μm. Time-gated images collected at these two imaging depths clearly show the two patterns, (Figure 3.6b). Similarly, human skin is composed of several layers, and ultrasonic images can be collected at the finger surface and at the dermal layer beneath the finger surface. Two time-gated fingerprint images collected at two depths are shown in Figure 3.6c. The sub-surface image matches the negative of the surface image. The two collected fingerprint images match the anatomy from [39]. The characteristics of the 110 $\times$ 56 rectangular PMUT array are summarized in Table 3.1.

Center Frequency f_0	14 MHz
Pressure at the Imaging Plane (5 Column TX Drive)	15 kPa
Receive Sensitivity	2 mV/kPa
Electromechanical coupling coefficient k_t^2	0.3%
Insertion Loss	90 dB
Number of Pixels	110×56
Pixel Size	$43 \times 58 \mu m$
Lateral/Axial Image Resolution	75/150 μm
Contrast Ratio	5:1

Table 3.1: Ultrasonic fingerprint sensor characteristics

3.6 Conclusions

This chapter presented a single-chip ultrasonic fingerprint sensor that meets the resolution requirements for consumer electronics applications. A high fill-factor array of rectangular PMUTs was shown to achieve the best acoustic performance. The array produces an output pressure of 15 kPa at 24V input to five columns of 56 PMUTs. The fractional bandwidth is 37%, sufficient to resolve images separated by an axial distance of 127 μm. Further optimization of the PMUT design may improve the fractional bandwidth to enable higher axial resolution.
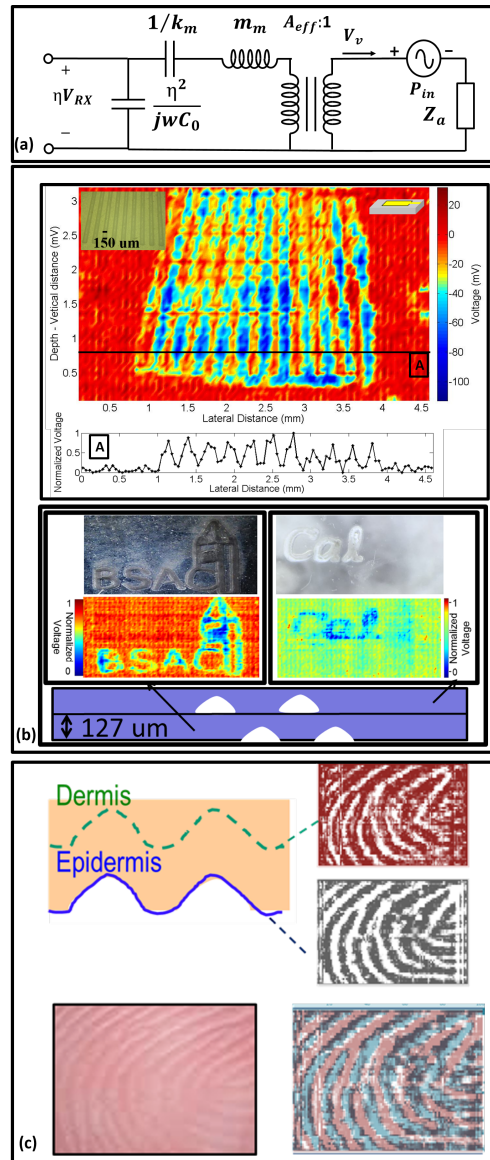
Figure 3.6: a) Equivalent circuit model for receiving. b) Pulse-echo images. Top: NIST fingerprint resolution test composed of converging parallel lines. Bottom: axial resolution demonstration using two overlaid patterns separated by 127 μm in depth. c) Ultrasound fingerprint image collected at the epidermis and sub-epidermis layer (top). Good agreement is observed between the ultrasonic images and the optical fingerprint image.

Chapter 4

Ultrasonic Fingerprint Sensor With Transmit Beamforming Based on a PMUT Array Bonded to CMOS Circuitry

4.1   Introduction

In this chapter, a single-chip 65×42 elements ultrasonic pulse-echo fingerprint sensor with transmit beamforming based on PMUTs directly bonded to a CMOS readout ASIC is presented. The earlier implementation of a smaller 8×24 element array is described in [13, 29], while the basic performance of a larger 110×56 array is described in Chapter 3 [22]. This latter array had a high fill factor (52%), which resulted in relatively high crosstalk between neighboring PMUTs in the array. In the array studied here, the PMUTs have greater spacing and therefore lower cross-talk, enabling us to demonstrate an increase in signal-to-noise ratio (SNR) and lateral image resolution using transmit (TX) beamforming. TX beamforming has been demonstrated at 8 MHz using AlN PMUTs without integrated electronics [40] and in a 256 element 2D CMUT array flip-chip bonded to an integrated circuit [41]. Here we use a column based TX beamforming scheme where the ultrasound image is collected by scanning across the 65 columns of the array. Using 5 adjacent columns to beamform, the measured TX pressure output is 25 kPa and the 3 dB beam-width is 50 μm, a $1.6 \times$ increase in pressure and $6.4 \times$ decrease in beam-width relative to non-beamformed measurements. Beamforming increases the receive voltage by a factor of 1.4 and the SNR by 7 dB. Because beamforming reduces the beam-width, the image resolution is improved compared to non-beamformed case, demonstrated through improved contrast in images of 2D grating phantoms and real fingerprint images.
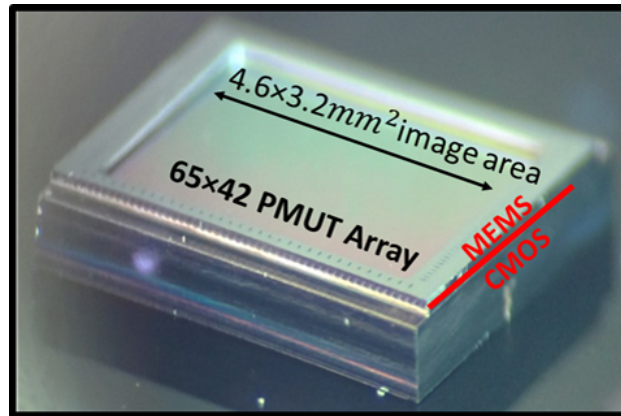
Figure 4.1: Photograph of the fingerprint sensor die, composed of a MEMS die bonded on top of a CMOS die. The Si handle wafer in a 4.6×3.2 mm^2 region in the middle of the MEMS die is etched via DRIE, exposing the thin-film PMUT array and leaving a 250 μm thick Si frame at the boundary of the die.

4.2 Sensor Architecture and Design

An image of the fingerprint sensor die is shown in Figure 4.1. The sensor was fabricated on a multi-project wafer using a commercial foundry manufacturing process where a standard CMOS wafer is bonded to a MEMS wafer using Al-Ge eutectic bonding [12]. The MEMS wafer containing the PMUT array is fabricated from an engineered silicon-on-insulator (SOI) substrate with a 1.7 μm thick Si device layer bonded to a 650 μm thick handle wafer. After the PMUT layers (described below) are deposited and patterned, the MEMS wafer is bonded to the CMOS wafer. Bonding is accomplished through Ge pads on 2.35 μm thick SiO_2 standoffs on the MEMS wafer that contact exposed Al pads on the CMOS wafer. After bonding, the MEMS handle wafer is thinned to 250 μm by grinding, after which deep reactive ion etching (DRIE) is used to remove the handle Si from a 4.6 mm × 3.2 mm region in the middle of the MEMS wafer, exposing the PMUT array.

4.2.1 PMUT Design

A detailed design study was conducted to compare PMUT designs of various diameters and geometries [5]. A rectangular 30×43 μm^2 PMUT design having high fill-factor was studied in [22, 6]. Here, we focus on a 35 μm diameter circular PMUT design that has greater mechanical isolation between neighboring PMUTs, shown in Figure 4.2. Each PMUT is anchored by a 13 μm wide annular Al-Ge eutectic bond and has a 24 μm diameter circular Al top electrode, designed to have the maximum electromechanical transduction [20]. The Al-Ge bonding is performed in vacuum and hermetically seals the gap between the two dice. The hexagonal layout of the array
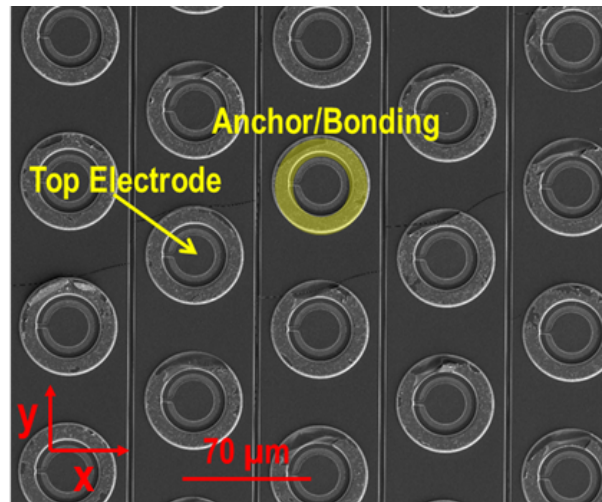
Figure 4.2: SEM image of the PMUT array, viewed from the top electrode side after debonding from the CMOS die. The 35 μm diameter circular PMUTs are arranged on a 70 $\times$ 80 μm grid and have a 24 μm diameter circular top electrode. Al-Ge eutectic bonds on 2.35 μm thick SiO$_2$ standoffs provide the mechanical anchor and electrical contact to the PMUT. The spacing between neighboring PMUTs, d, is equal to 25 μm. The lines between the PMUT columns show where the AlN and Mo bottom electrode layers are etched to electrically isolate each column.

enables close packing of the circular PMUTs, which are spaced on a 70 $\times$ 80 μm grid, resulting in a resolution of 376 $\times$ 318 dpi.

Each PMUT is a piezoelectric unimorph composed of 1 μm thick AlN sandwiched between top and bottom metal electrodes on a single-crystal silicon layer with 1.7 μm nominal thickness, shown in cross-section in Figure 4.3. The Mo bottom electrode layer is patterned to electrically isolate each column of PMUTs. This enables the PMUTs to be used as 2-port devices, with the bottom electrode connected to high-voltage TX circuitry and the top electrode connected to low-voltage RX circuitry. Al-Ge eutectic bonds on SiO$_2$ standoffs provide the mechanical anchor and electrical contact to the PMUT. Since there are no anchors between the columns, the unsupported AlN/Si membrane between the anchors of neighboring columns is the main origin of mechanical crosstalk. For comparison, the vibration amplitude of this unsupported region is -2.7 dB relative to the transmitting PMUT's amplitude in the 110$\times$56 array described in [42] and is -17dB in the 65$\times$42 array described here.
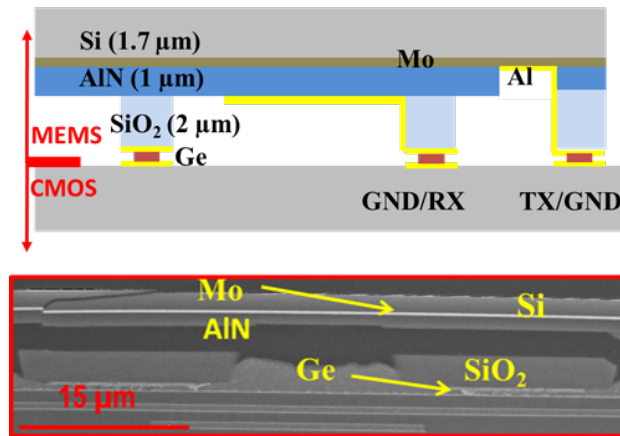
Figure 4.3: Cross-section of a single PMUT. Top: schematic layout. AlGe bonds connect the Al top electrode to a TX/RX switch and the Mo bottom electrode to the TX amplifier on the ASIC. Bottom: cross-section SEM image. The AlGe bond at the base of the SiO_2 standoff broke during cross-sectioning.

4.2.2   Circuit Architecture

A schematic of the array and associated circuitry is shown in Figure 4.4. Pulse-echo measurements are performed sequentially, column-by-column, beginning with the TX phase, during which an ultrasound pulse is transmitted from a selected column, followed by the RX phase, where the returning echoes are received by the same column. The measurement is complete after 65 pulse-echo cycles, when all columns have been read out. Each single-column pulse-echo measurement takes 24 μs, and readout of the entire 65 column array takes 1.56 ms.

A 0.18 μm CMOS wafer with 24V high-voltage transistors provides signal-processing electronics, described in detail in [6]. The 42 PMUTs in each column share a common Mo bottom electrode that is connected to a high-voltage (24V) TX amplifier, and have individual top electrodes that are bonded to low-voltage (1.8V) receive circuitry. The TX waveform is a unipolar 24V, 2-cycle, 20 MHz pulse. To protect the low-voltage RX amplifiers from the high voltage TX signal, switches connect the top electrodes to ground (GND) during the transmit phase. During the RX phase, these switches connect the 42 PMUTs in the selected column to individual RX amplifiers. A column-select multiplexer (not shown in Figure 4.4) connects the outputs of the RX amplifiers to the envelope detectors and sample-and-hold amplifiers used to demodulate and sample the RX signal from the selected column. The sample-and-hold time can be varied to record echoes returning at different times, thereby recording images at different depths. A second multiplexer connects the outputs of the 42 on-chip sample-and-hold amplifiers to an off-chip 8-bit analog-to-digital converter (ADC).

When TX beamforming is used, the measurement cycle is the same as described above, except
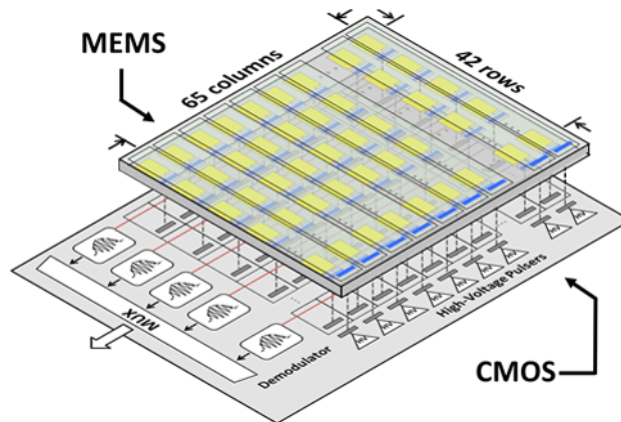
Figure 4.4: Cross-section of a single PMUT. Top: schematic layout. AlGe bonds connect the Al top electrode to a TX/RX switch and the Mo bottom electrode to the TX amplifier on the ASIC. Bottom: cross-section SEM image. The AlGe bond at the base of the SiO_2 standoff broke during cross-sectioning.

that the TX signal is applied to five adjacent columns, with the center column used to receive the returning echo. The TX signal is delayed symmetrically about the center column with a delay pattern $(0, \Delta t_1, \Delta t_2, \Delta t_1, 0)$, where Δt_1 and Δt_2 are time delays programmable in 10 ns increments and selected to give a desired focal distance.

4.2.3   Sensing Mechanism

The fingerprint image is measured based on the reflection of ultrasound from the surface of the finger. To achieve high contrast ratio, the sensor surface was first coated with a 220 μm thick layer of poly-dimethylsiloxane (PDMS) (Sylgard 184, Dow Corning) to provide an acoustic coupling layer with similar acoustic impedance to human tissue, as illustrated in Figure 4.5. The acoustic reflectance at the finger-PDMS interface is given by $R = \dfrac{(Z_T - Z_C)}{(Z_T + Z_C)}$, where $Z_T = \rho_T \times c_T$ is the acoustic impedance of the target (fingerprint) and $Z_C = \rho_C \times c_C$ is the impedance of the coupling layer (PDMS, 1.04 MRayls). Where the fingerprint has a ridge, the target impedance is that of human tissue ($Z_T = 1.63\ MRayls$ [42]) and the reflectance is low (R = 22 %); where the fingerprint has a valley, the target impedance is that of air ($Z_T = 0.43\ kRayls$) and the reflectance is high (R = 99%). Because the sensing mechanism is based on the acoustic impedance mismatch between the coupling layer and the finger, the sensor is significantly less sensitive to oil or moisture on the finger than either capacitive or optical fingerprint sensors, as demonstrated in [6].
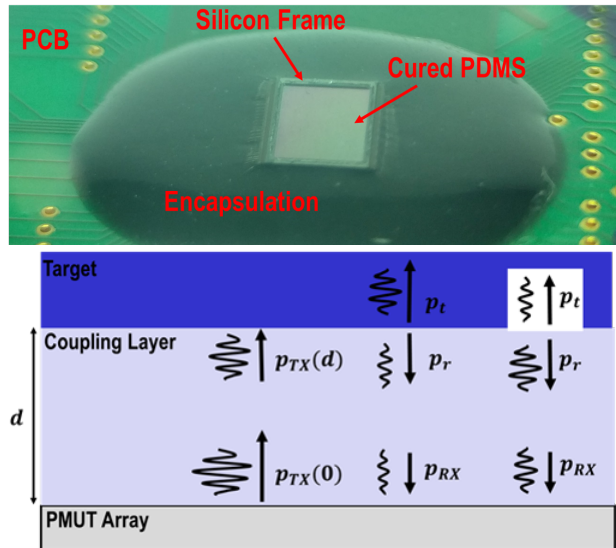
Figure 4.5: Image of the packaged fingerprint sensor (top) and illustration of fingerprint imaging (bottom). A 215 μm thick PDMS coupling layer coats the PMUT array. A pressure pulse arriving at the surface of the coupling layer is partially reflected (p_r), resulting in an echo that is received by the PMUT array. The image contrast is determined by the relative intensities of the returning echoes from regions of the target fingerprint where there are ridges and valleys, illustrated as dark and light sections of the target.

4.3 Results

This section describes the model and experimental results for the peak pressure and beam-width when transmitting with one column and five columns both with and without transmit beamforming. The signal to noise ratio (SNR) is calculated based on the RX voltage amplitude for beamformed and non-beamformed cases.

4.3.1 Pressure Output

Following [5], we model the pressure output from the PMUT using a two-port electromechanical model in which the PMUT dynamics are modeled as a 2nd order system with 19.2 MHz resonance frequency and quality factor Q=1.5. The vibration amplitude of the model was adjusted so that it agreed with experimental measurements of the PMUT's pulse response, measured using a laser Doppler vibrometer (LDV, UHF-120, Polytec, Inc.). Figure 4.6 shows that the model accurately matches the experimentally-measured pulse response.
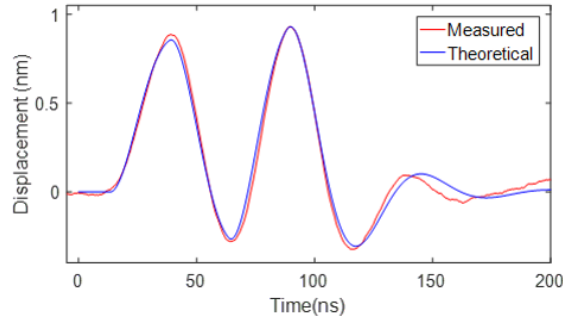
Figure 4.6: Measured time-response of a single PMUT to a 24V two-cycle 20 MHz pulse input along with the response predicted by the 2nd order

The measured pulse response was used to develop a model for the array's acoustic pressure field. A simplified schematic for the array geometry used to calculate the pressure field is shown in Figure 4.7. The theoretical surface pressure p_i^{av} of a circular PMUT with peak velocity u_p in PDMS (density ρ= 1040 kg/m^3 and speed of sound c_0= 1000 m/s) is calculated as

$$p_i^{av} = \frac{1}{3}(\rho_0 c_0 u_p), \tag{4.1}$$

Using $\varphi(t - \Delta t_i)$ to denote the PMUT's normalized time-response to a pulse delayed by Δt_i, the total peak pressure at the focal point is calculated based on superposition [16]

$$p_{tot} = max|\sum \frac{R_0 p_i^{av}}{r_i}D(\theta_i)e^{-jkr_i}\varphi(t - \Delta t_i)|, \tag{4.2}$$

where r_i and θ_i are the distance and angle of the ith PMUT to the focal point, k is the wavenumber, $R_0 = \frac{ka^2}{2}$ is the Rayleigh distance for a circular PMUT with radius a, and $D(\theta_i)$ is the directivity of a single PMUT,

$$D(\theta_i) = \frac{48J_3(kasin\theta_i)}{(kasin\theta_i)^3}, \tag{4.3}$$

where J_3 is a third-order Bessel function.

The time delays for transmit beamforming are calculated as $\Delta t_i = \Delta r_i/c_0$, where Δr_i is the difference in the pathlength of the i_{th} column relative to the pathlength of the outermost column used in beamforming. To focus at the surface of the 215 μm thick PDMS layer, the time delays are (0 ns, 30 ns, 40 ns, 30 ns, 0 ns) for the (N-2, N-1, N, N+1, N+2) columns. In Equation 4.2, we neglect the absorption loss from the PDMS layer, which is calculated as $L = af^\beta$, where $a = 0.4$ dB/cm/MHz, β=1.4 , and f is the frequency in MHz [43]. At 20 MHz, this model yields an absorption coefficient of 26.5 dB/cm, or 0.5 dB for a 215 μm thick layer of PDMS, much less than the acoustic spreading loss.
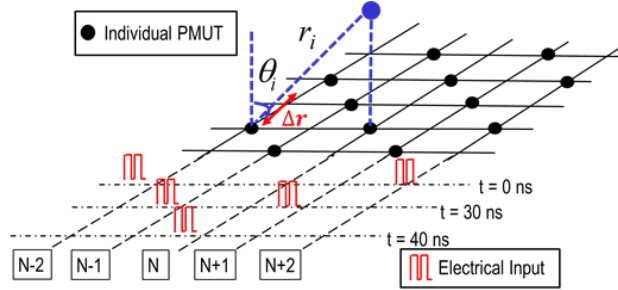
Figure 4.7: Array geometry used for pressure superposition calculations. The distance r_i and angle θ_i between an individual PMUT (black dot) to the focal point (blue dot) are labeled.

This model was first used to study how the peak pressure and beam-width vary as a function of the PMDS thickness to determine how the fingerprint imaging resolution degrades as the distance to the imaging plane is increased from 100 μm to 800 μm. The results of these simulations are shown in Figure 4.8. With a 100 μm PDMS layer, the minimum 3 dB beam-width was approximately 50 μm and the maximum pressure was nearly 50 kPa. With an 800 μm PDMS layer, the beam-width increases to 240 μm, approximately 5 times greater than the desired $\lambda = 50 \mu m$ needed to achieve 500 DPI image resolution. With a 70 μm pitch, the aperture of the 5 columns is only 350 μm. To achieve the minimum (50 μm) beam-width at long distances, the aperture must be increased proportionally, e.g. to 25 columns (1750 μm aperture) for imaging at an 800 μm distance.

To validate the model, the two-dimensional pressure field at the PDMS surface was imaged by measuring the ultrasonic deformation of the PDMS surface using a scanning LDV. The pressure field is computed from the measured deformation image by multiplying the measured velocity by the acoustic impedance of PDMS,

$$p(x, y) = \rho_0 c_0 u(x, y)/2, \tag{4.4}$$

where the factor of two in the denominator corrects for the free boundary at the PDMS surface. The measured and modeled pressure fields for single-column TX with 2 cycle 20 MHz input are shown to have excellent agreement in Figure 4.9. The measured and modeled pressure fields for 5-column TX both with and without beam-forming are shown in Figure 4.9. The measured peak pressure with beamforming is 25 kPa and the 3dB beam-width is 50 μm, a 1.6$\times$ increase in peak pressure and 6.4$\times$ decrease in beam-width compared with non-beamformed results. The measured pressure field agrees with the field predicted by the model except that the measured pressure is approximately half the predicted value. We attribute this difference to cross-talk between the columns of the array, which results in unpredicted variations in the phase and amplitude of the vibration of the 5 columns. Cross-talk arises both from Rayleigh-Bloch waves traveling at the PDMS-silicon interface [43] and due to mechanical coupling in the thin AlN-Si layer between neighboring PMUTs [42].
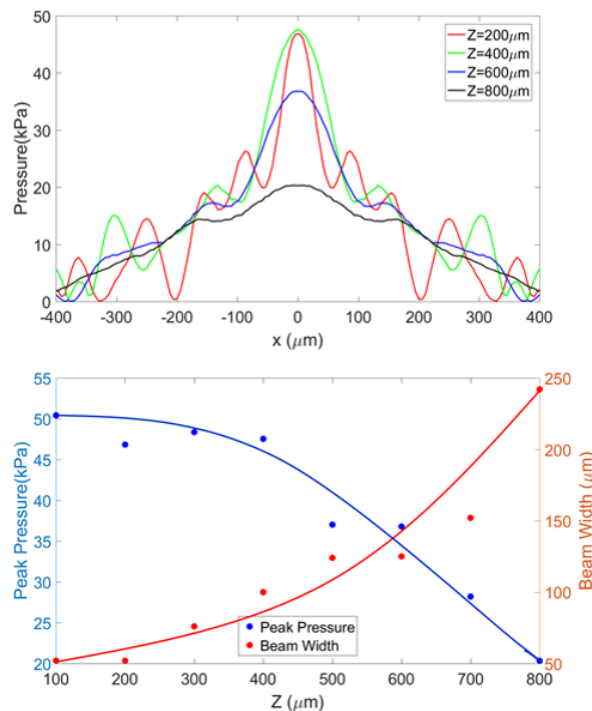
Figure 4.8: Simulated pressure field for 5-column TX beamforming when focused on the surface of a PDMS layer with thickness varying from 100 μm to 800 μm. Absorption loss in PDMS is neglected. Top: simulated pressure field along the beam-formed axis. Bottom: peak pressure and beam-width as a function of PDMS thickness. The lines are drawn to guide the eye.

4.3.2 Receive Signal

Described in detail in [6], during the receive phase, the received piezoelectric charge is amplified by a charge amplifier followed by a gain stage. The total effective voltage gain of the RX signal-chain is 22 dB. The echo returned from the sensor's PDMS-to-air interface was used to characterize the RX signal when the TX signal was generated with 1 column, 5 columns, and 5 beamformed columns. The measured time domain RX signals for these three cases are shown in Figure 4.10. The peak RX voltage from 5 column beamformed TX is 1.4 times greater than the result with 1 column TX, consistent with the measured increase in peak TX pressure. Secondary echoes can be seen in the RX signal because the PDMS surface is close relative to the column length (2.94 mm). As a result, the PDMS surface is not in the far-field and the TX signals from the PMUTs in the column do not arrive simultaneously. This effect can be reduced by 2D beamforming.

The signal to noise ratio was calculated as

$$SNR = 20log_{10}(V_{air}/V_N), \tag{4.5}$$

where V_{air} is the RMS RX amplitude (before any amplification) from the PDMS-to-air interface,
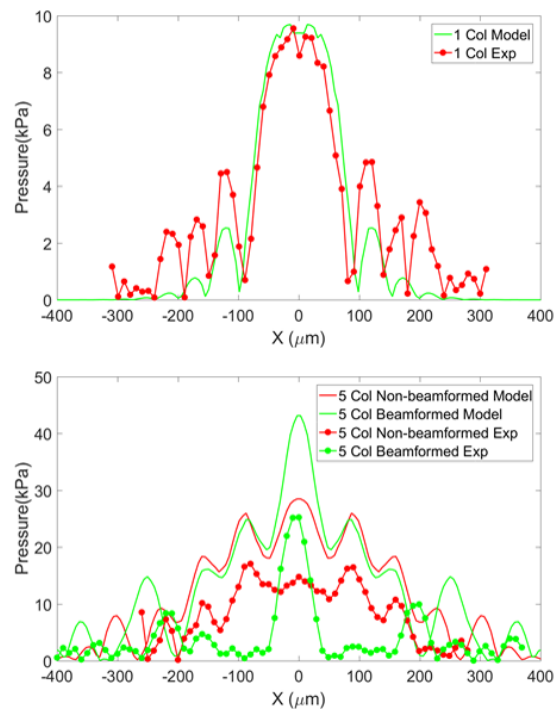
Figure 4.9: Modeled and measured pressure output on top a 215 μm thick PDMS when 1 column (top) and 5 columns (bottom) of 42 PMUTs were exited with 2 cycle 20 MHz electrical pulse input.

and $V_N = 46 \mu V$ is the RMS input-referred noise. Shown in Figure 4.10, the SNR for beamformed TX is 7 dB higher than the non-beamformed case.

4.3.3 Imaging

A PDMS phantom was molded using a Si wafer etched with a pattern of 150 μm wide lines and spaces. The pattern was imaged using 5 column TX with and without beamforming, and the resulting images are shown in Figure 4.11. In each experiment, pulse-echo measurements were collected from each of the 65 columns in sequence, with a complete image formed in 2.6 ms. In each column's measurement cycle, five adjacent columns (N-2, N-1, N, N+1, N+2) of 56 PMUTs were excited during the TX phase and the center column (N) was used as receiver. The average contrast in the beamformed image is 2.2 mV, a 1.5 times increase over the non-beamformed result. In addition, the 150 μm wide line pattern is better resolved as a result of the beamformed 50 μm 3 dB beam-width.

Real fingerprint images were collected by pressing the author's finger on the PDMS-coated
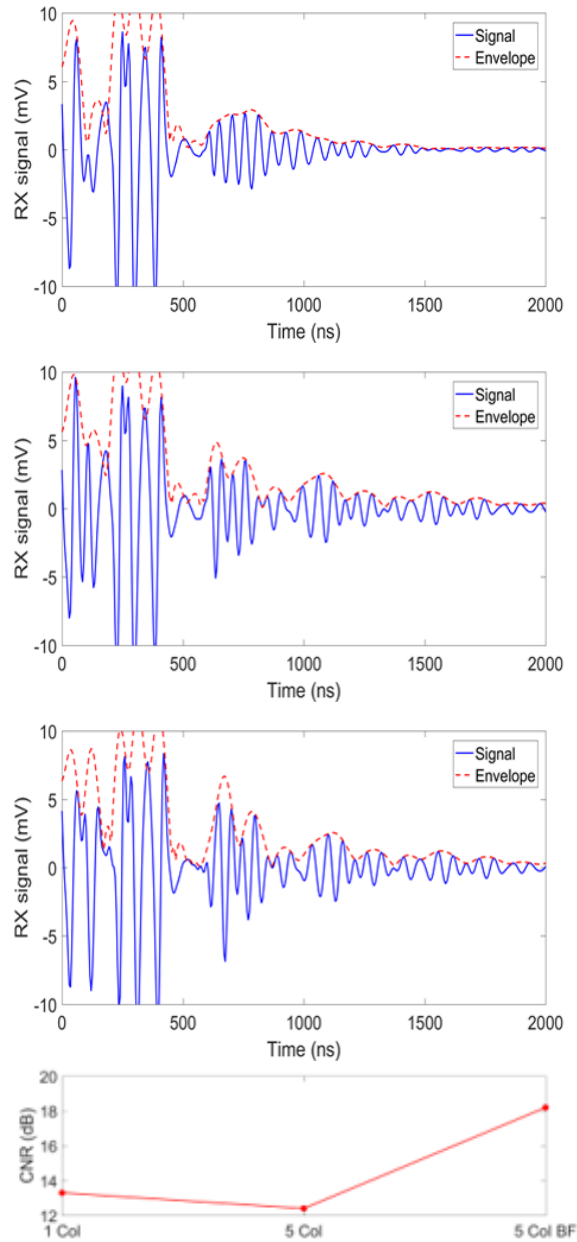
Figure 4.10: Measured RX voltage for: (a) 1 column TX; (b) 5 column non-beamformed TX; and (c) 5 column beamformed TX. (d) The SNR calculated for the three cases, showing that beamforming increases the SNR by 7 dB.
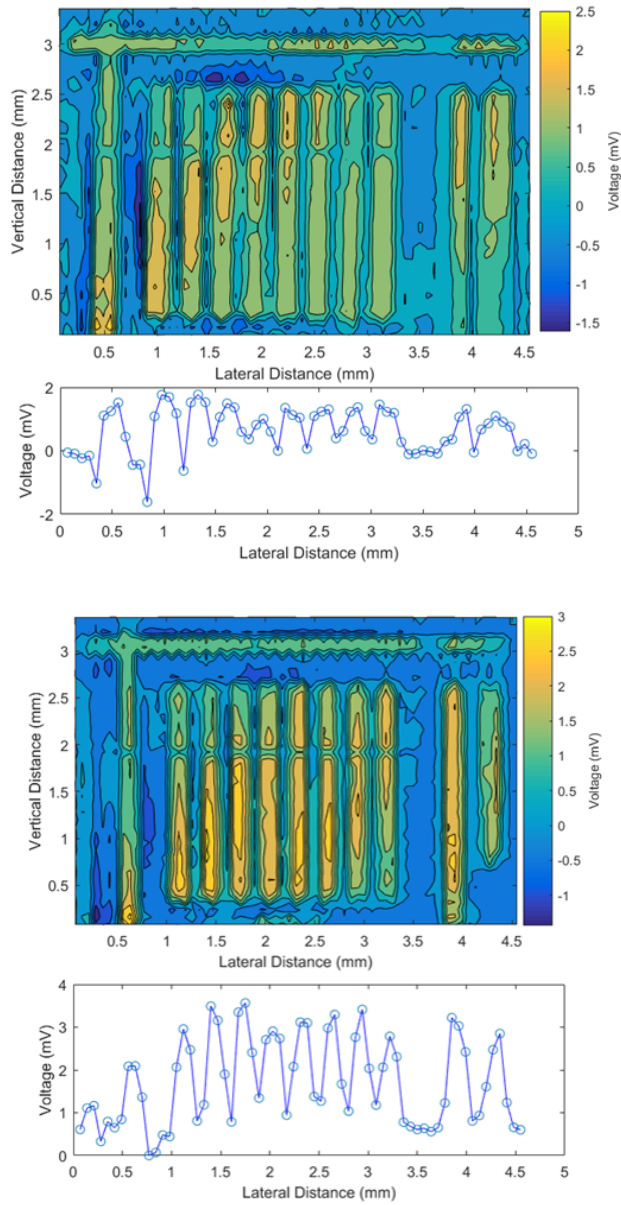
Figure 4.11: Ultrasonic images and x-axis line-scans measured from 150 μm line and space PDMS grating phantom. Top: non-beamformed results. Bottom: beamformed results. Beamforming increases the contrast by a factor of 1.5 and improves the resolution of the grating pattern.
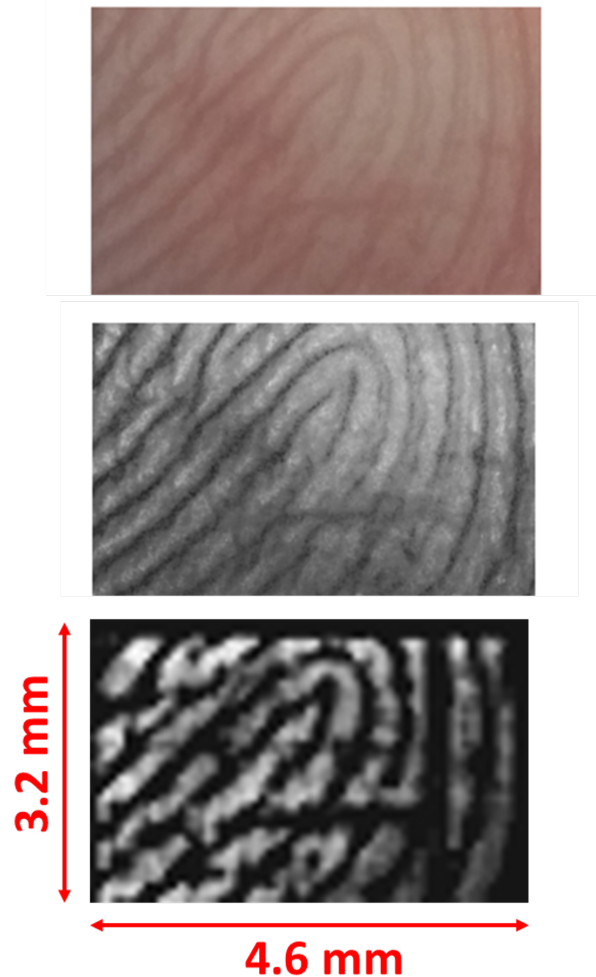
Figure 4.12: Optical, enhanced optical, and ultrasonic fingerprint images. The average ridge width is 400 μm. Dark spots in the ridges are sweat pores. A dark vertical stripe in the image corresponds to a failed column in the sensor.

surface of the sensor. A 4.6 mm $\times$ 3.2 mm ultrasonic image of a real fingerprint is shown next to an optical image of the same fingerprint in Figure 4.12. The dark vertical line on the right of the image is due to a failed column in the sensor. The average ridge width is about 400 μm and ridges and valleys are clearly resolved in this image. The figure pattern, a right loop, is captured. Some sweat pores and minutia points are visible in the ultrasonic image.

4.4   Conclusion

This chapter demonstrated a 65×42 element ultrasonic fingerprint sensor based on PMUTs bonded to CMOS. The sensor's TX acoustic pressure field was modeled starting from the measured pulse response of a single PMUT. The pressure field predicted using the model agrees well with measurements of the pressure field collected using a scanning LDV. The sensor is capable of multi-channel TX beamforming to improve the SNR and resolution of the fingerprint image. Using 5-column TX beam-forming, the peak pressure, receive voltage, and image contrast all increase by a factor of 1.5. In addition, the beam-width decreases by a factor of 6.4, and the SNR increases by 7 dB. The measured pressure using TX beamforming was approximately half the value predicted by the model, a difference we believe is due to mechanical and acoustic cross-talk in the array. Modeling and experiments are currently underway to better understand and mitigate the sources of cross-talk so that the sensor's imaging characteristics can be further improved.

Chapter 5

Inter-element Coupling Effect In Pulse-echo Ultrasonic Fingerprint Sensors

Ultrasonic fingerprint sensors based on micromachined ultrasound transducers require very fine pitch to achieve high resolution imaging. We consider again the 110×56 PMUT array based on monolithic eutectic bonding to CMOS, which was descussed in Chapter 3. To achieve high fill-factor, the PMUTs are anchored through small eutectic pillars, resulting in a high degree of mutual coupling between neighboring PMUTs. As a result, the mode shape is more complicated than a single-MUT dynamic model. We created a finite element model that better models the mode shapes exhibited by the entire array. Experimental measurement of the mode-shape via laser Doppler vibrometry allows us to compute the volume velocity, which correlates to the measured far field pressure.

5.1   Introduction

To meet the 500 DPI resolution standard for fingerprint sensors in consumer electronics, ultrasonic fingerprint sensors based on micromachined ultrasound transducers (MUTs) require a dramatic reduction in the PMUT size to $< 50 \mu m$. However, when the spacing between MUTs is small, cross-talk from mechanical and acoustical coupling is greatly increased [44, 45]. Consequently, the sensor's pulse-echo performance is not accurately modeled using single-MUT dynamic models. Instead the array dynamics must be understood. Here, we investigate a 110×56 piezoelectric MUT (PMUT) array based on monolithic AlGe eutectic bonding of a PMUT wafer to a CMOS wafer [5]. To achieve high ($> 50\%$) fill-factor, the PMUTs are anchored through small AlGe pillars, resulting in a high degree of mutual coupling between neighboring PMUT cells as well as displacement outside the designed PMUT region. We developed a finite-element method (FEM) model of the array that captures the array's fundamental mode shapes. Scanning laser Doppler vi-

brometry (LDV) was used to experimentally measure the mode-shape when the array is immersed in fluid (Fluorinert FC-70, 3M), allowing us to compute the volume velocity at two different frequencies of operation. The resulting volume velocity allows the transmit pressure to be predicted and compared with experimental pressure measurements.

5.2 Design

A cross-section schematic of an individual PMUT is shown along with photographs of the 110×56 sensor chip in Figure 5.1. Each PMUT is a piezoelectric unimorph composed of 1 μm thick AlN on a single-crystal silicon layer with 1.7 μm nominal thickness. Al-Ge eutectic bonds on SiO_2 standoffs provide the mechanical anchor and electrical contact to the PMUT [12]. The PMUTs are formed on an SOI MEMS wafer that is bonded to a CMOS wafer. Following wafer bonding, the MEMS handle wafer is mechanically thinned to 200 μm thickness and the PMUT array is exposed by through-wafer DRIE etch that removes the MEMS handle wafer in a 4.64 mm by 3.36 mm region at the center of each 5.36 by 4.58 mm die. The array consists of 43 μm x 30 μm PMUTs on a 43 μm x 58 μm grid, resulting in a resolution of 591 $\times$ 438 DPI. As shown in Figure 1, the PMUTs in the same column are separated by 28 $\mu m \times$ 30 μm SiO_2 anchors. The spacing between anchors defines the 30 μm vertical dimension of the PMUT, while the horizontal dimension of the PMUT is equal to the 43 μm column pitch. To increase the fill-factor, there are no anchors between PMUTs in adjacent columns, but the AlN layer is removed between columns to reduce mechanical coupling. The fact that there are no anchors between the columns, and the presence of unsupported AlN/Si membrane between the anchors of neighboring columns is the main origin of the mechanical cross-talk behavior observed in the experiments reported here.

A 0.18 μm CMOS wafer with 24V high-voltage transistors provides signal-processing electronics, described in detail in [6]. Each of the 6,160 PMUTs in the array has a dedicated receive (RX) amplifier that is connected to the Al top electrode during the receive phase. The 56 PMUTs in each column share a common Mo bottom electrode that is connected to a 24V transmit amplifier (TX) during the transmit phase. To protect the RX amplifier from the high TX voltage signal, a TX/RX switch connects each top electrode to ground (GND) during transmit.

5.3 Mechanical Model

To model the transmit-receive behavior of the array, we begin with the connection between vibration amplitude and acoustic pressure. The theoretical surface pressure of a PMUT unit cell p_0 is given by the product of the volume velocity V_v and the acoustic impedance of the surrounding
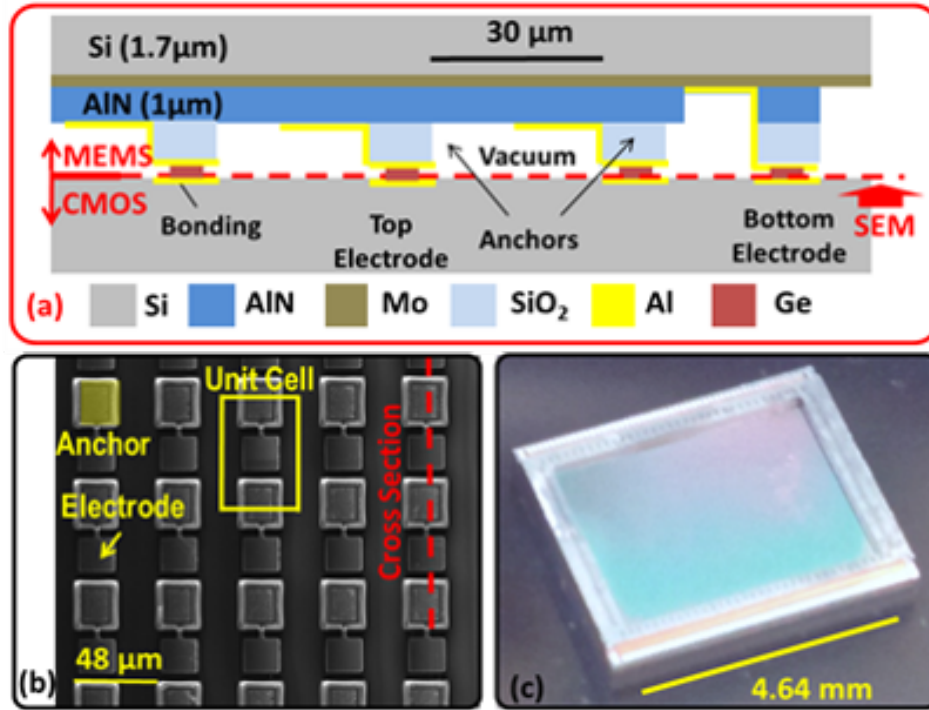
Figure 5.1: Fingerprint sensor diagrams: (a) schematic cross-section of 3 PMUTs and the contact
to the Mo bottom electrode; (b) SEM image of the PMUT array, viewed from the top electrode
side after debonding from CMOS; (c) photograph of the 4.6 mm by 3.2 mm sensor.

medium Z_f,

$$p_0 = V_v Z_f \tag{5.1}$$

The volume velocity is the average velocity of the unit cell multiplied by the area, A, which we
write as

$$V_v = 2\pi f_0 d_{eff} A \tag{5.2}$$

where f_0 is the vibration frequency and $d_{eff} = (\iint d_i dA)/A$ is the average displacement over the
unit cell. To predict the value of d_{eff} at a given excitation frequency, we created a finite element
method (FEM) simulation. The first four mode-shapes and their corresponding undamped natural
frequencies in vacuum are shown in Figure 5.2. The 31 MHz mode-shape exhibits the expected
shape, where the dominant vibration amplitude occurs beneath the top electrode of each PMUT
in the array. The other modes exhibit unanticipated behavior: at 17 MHz most motion occurs in
the space between PMUTs in adjacent columns; at 34 MHz the entire region between columns
vibrates; and at 41 MHz, the un-electroded space between anchors vibrates.

To identify the mode that produces the largest surface pressure, we then simulated the volume
velocity of an immersed array as a function of input frequency. The simulated volume velocity
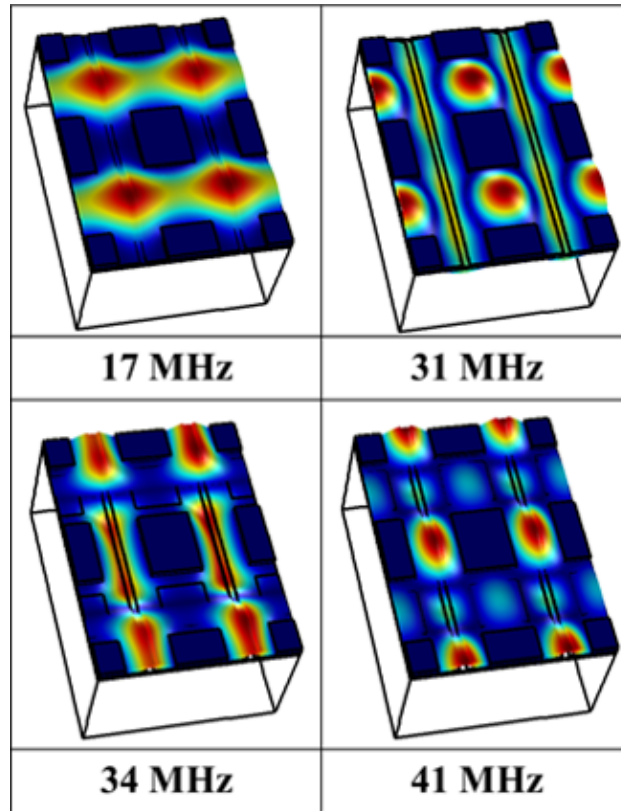
Figure 5.2: FEM simulated mode-shapes of the PMUT array, viewed from the top electrode side. The simulated area includes two PMUTs in the same column, separated by a SiO_2 anchor (blue rectangle) at the center. The vertical bars between the columns show the region where the AlN layer is removed.

in response to a 1 V sinusoidal input with varying frequency is shown in Figure 5.3, along with the mode-shapes corresponding to the two peaks at 14.75 MHz and 19.25 MHz. The immersed mode-shape at 14.75 MHz resembles the undamped mode-shape at 34 MHz, whereas the 19.25 MHz response appears to be a combination of modes. Note that the peak amplitude at the center of each PMUT is much larger at 14.75 MHz than it is at 19.25 MHz (0.41 nm/V versus 0.17 nm/V). However, there is significant anti-phase vibration in the region between columns, reducing the total volume velocity of both modes.

5.4   Experimental Results

PMUTs were measured in fluid (Fluorinert FC-70, 3M) using a Laser Doppler Vibrometer (LDV, UHF-120, Polytec, Inc.) with a precision xy positioning stage. The full-field, time-domain vi-
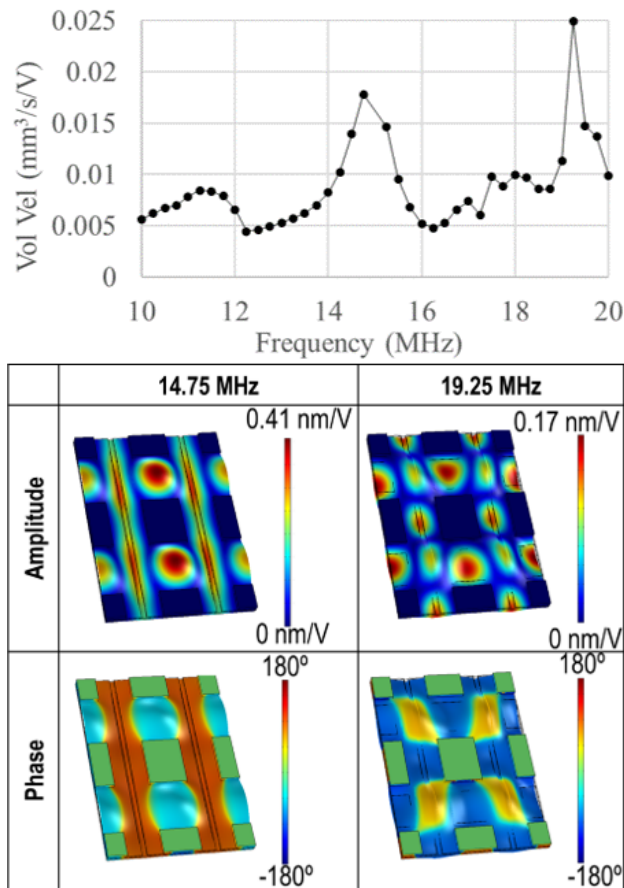
Figure 5.3: Simulated volume velocity response with a 1 Volt input (top). Amplitude and phase
mode-shapes observed at the frequencies with peak volume velocity (bottom).

bration of the PMUT array in response to pulsed inputs was measured with a 4 μm scanning grid.
During the experiment, the laser was focused on the PMUT plane and the refractive index of FC-70
is used to correct the measured amplitude. Limited by the CMOS design, 24V pulsed inputs at 14
MHz and 20 MHz were used to drive five columns of PMUTs. The measured mode shape of 5
columns of PMUTs excited with a 2 cycle 14 MHz pulse input is shown in Figure 5.4. The time-
domain displacement at three characteristic locations, PMUT center (A), between PMUT columns
(B), and between PMUT rows (C), are plotted to show their different decay envelopes and fre-
quencies. At 14 MHz, the displacements at points A and B have opposite phase. The mode shape
and phase difference agree well with the FEM simulations shown in Figure 5.3. In addition, the
magnitude of the displacement at point A is consistent with the simulation at 14 MHz input, where
a peak displacement of 0.16 nm/V is predicted.

The measured mode shape of 5 columns of PMUTs excited with a 2 cycle 20 MHz pulse input
is shown along with the time-domain displacement and volume velocity plots in Figure 5.5. The
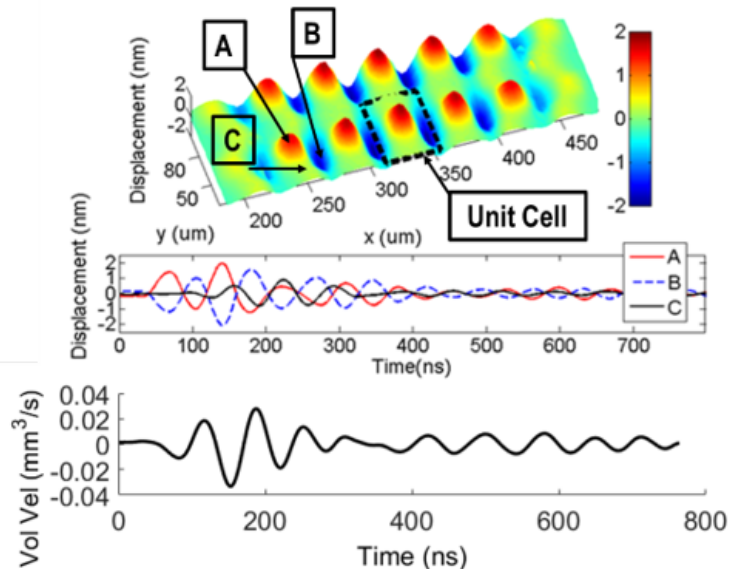
Figure 5.4: Top: measured TX mode shape following 2 cycle 14 MHz pulse input. Bottom: time-domain displacement at PMUT center (A), between PMUT columns (B), and between rows (C). Bottom: computed volume velocity of a unit cell.

displacement at point A is in-phase with point C, but antiphase with point B. The mode shape and phase difference are as modeled in simulation. In addition, the magnitude of the displacement at point A is consistent with the peak displacement of 0.12 nm/V predicted by FEM. Comparing the results in Figure 5.4 and Figure 5.5, the peak displacement at the PMUT center at 14 MHz input is twice that at 20 MHz input. Moreover, the ring-down times are different at the two different frequencies. A shorter ring-down will lead to higher axial resolution, since the axial resolution AR scales as

$$AR \sim \lambda(N_t + N_r)/2 \tag{5.3}$$

where λ is the radiating wavelength, N_t is the number of input pulse, and N_r is the number of ring down pules. N_r linearly scales with the quality factor Q [24]. Since the immersed Q is determined by the mode's acoustic radiation, we attribute the difference in ring-down time of the two modes to a difference in the acoustic radiation of these modes. The mode-shapes measured via scanning LDV allow the volume velocity to be computed. The volume velocity computed from the mode shapes is 0.033 mm^3/s at 14 MHz and mm^3/s at 20 MHz. Note that the volume velocities are similar despite the fact that the peak displacements differ by a factor of 2. Comparing to the FEM model shown in Figure 5.3, the predicted volume velocity with a 24V input is 0.096 mm^3/s at 14 MHz (3x greater than the experimental result) and 0.12 mm^3/s at 20 MHz (4x greater than the experimental result). Some of the difference between experiment and model is due to fabrication variation and some is due to the fact that the pulsed input used in experiments does not produce the full steady-state amplitude. We note that both modes suffer from reduced volume velocity due to anti-phase motion between the columns. For comparison, the volume velocity predicted using
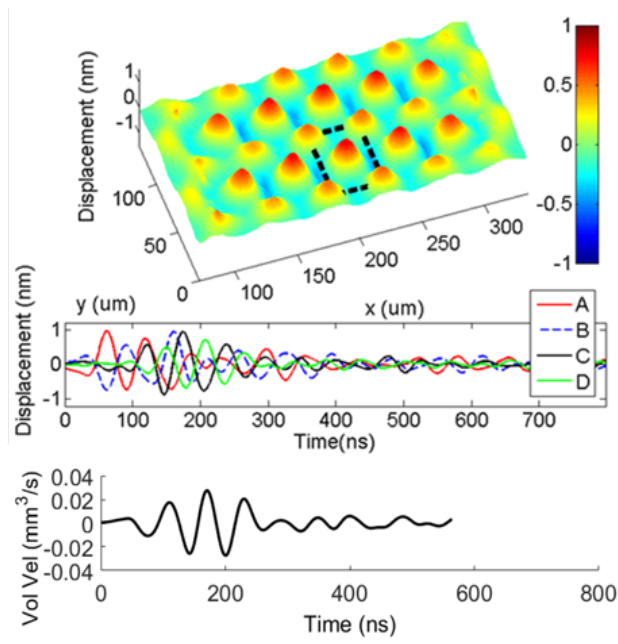
Figure 5.5: Top: measured TX mode shape following 2 cycle 20 MHz pulse input. middle: time-domain displacement at PMUT center (A), between PMUT columns (B, C), and between rows (D). Each point exhibits different decay envelopes and frequencies. Bottom: computed volume velocity of a unit cell.

a simple model based on a single circular PMUT with the same area is 0.073 mm^3/s at 14 MHz (2.2x greater than the experiment) and 0.05 mm^3/s at 20 MHz (1.8x greater than the experiment).

The pressure of the TX pulse was measured using a 40 μm diameter hydrophone (Precision Acoustics) at a distance 800 μm away from the array. The measured TX pressure wave, shown in Figure 5.6, has a peak pressure of 9.0 kPa at 14 MHz and 7.1 kPa at 20 MHz when 5 columns were excited with a 2-cycle pulse. To compare this with the pressure predicted from the volume velocity computed from the measured mode-shapes, we relate the theoretical surface pressure to the pressure at a distance r from the array by summing the effective PMUTs with a pulsed input:

$$p(r) \sim \sum p_0 R_0 r^{-1} \tag{5.4}$$

where $R_0 = S/\lambda$ is the Rayleigh distance for a source with surface area S radiating at an acoustic wavelength λ. Using the area of one PMUT cell, the Rayleigh distance for a single PMUT unit cell is 25 μm at 14 MHz and 35 μm at 20 MHz. Substituting the volume velocities computed from the LDV measurements into the surface pressure in Equation 5.1, the theoretical surface pressure is 33 kPa at 14 MHz and 28 kPa at 20 MHz for one PMUT unit cell. Substituting these surface pressures into Equation 5.4 and accounting for the pulsed operation, the expected pressure at 0.8 mm from the array is about 10 kPa at 14MHz and 12 kPa at 20 MHz, close to the values measured with the hydrophone.
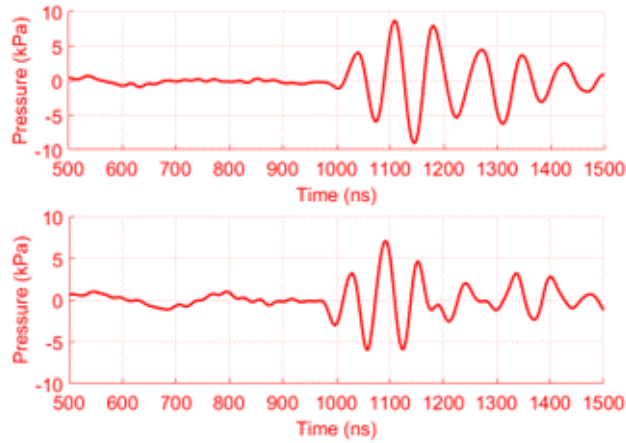
Figure 5.6: Measured pressure in response to 14 MHz (top) and 20 MHz (bottom) pulse inputs.

The performance of the array at 14 MHz and 20 MHz is summarized in Table 1 which shows the measured peak displacement d_p, computed volume velocity V_v from LDV mode-shape, pressure calculated from the mode-shape p_c, and measured pressure output p_m. Note that the volume velocities of the two modes are quite similar, because the ratio of the displacement amplitudes (2:1) is almost the inverse of the frequency ratio (14:20) of the two modes. As a result, the TX pressure is roughly the same from both modes. While the model predicts slightly higher TX pressure from the 20 MHz mode than the 14 MHz mode and the experiment shows the opposite result, the difference is within the measurement error due to uncertainties in position of the hydrophone.

Mode	d_p	V_v	Computed p_c	Hydrophone p_m
14 MHz	2 nm	0.033 mm^3/s	10 kPa	9 kPa
20 MHz	1 nm	0.028 mm^3/s	12 kPa	7.1 kPa
Ratio	2	1.2	0.8	1.3

Table 5.1: Performance summary

5.5 Conclusion

This chapter studied the mechanical behavior of a 56×110 array PMUT ultrasonic fingerprint sensor. Using FEM models, we have shown there are two distinct deflection of motion at different input frequency. However, the pressure output from the two deflection of motion are compatible. Moreover, significant vibration occurs in regions between the PMUTs. Because this vibration is in antiphase with the vibration of the PMUTs, the volume velocity is reduced by roughly a factor of two relative to the value that would be predicted from the PMUT motion alone. We

have verified that the measured TX pressure is in reasonable agreement with the value predicted from the LDV-measured volume velocity, leading us to conclude that the TX performance could be improved by a factor of two or more through improved mechanical design. Because a PMUT is a reciprocal transducer, improvements to TX performance usually produce an equal increase in RX performance, suggesting that the improved design could achieve a 4-fold increase in pulse-echo signal-to-noise ratio.

Chapter 6

Two-dimensional Pressure and Motion Characterization of the Ultrasonic Fingerprint Sensor

6.1 Introduction

The pressure fields due to transient or pulsed excitation are different from those of continuous sinusoidal excitation, approximate analytical solutions, numerical calculations, and experiments have been attempted to understand the acoustic nearfields of the pulsed excited transducers [46, 47]. Based on the attempt of an accurate numerical calculation of the pressure field generated by the pulsed piston transducer with different excitation pulses [47], the pulsed sonic field close to the piston surface consists of an essentially plane wave replication of the piston motion, at the far field, the pulse amplitude is more similar to the CW case without the distinct nulls as the complete interference is not possible. At the same time, theoretical near-field field patterns for arrays of different geometries excited with pulses has been investigated for medical ultrasound transducer array designs [48]. The near field pattern generated by the pulsed transducers arrays is found to be space-variant, unlike the continuous wave radiation. Also, the radiation pattern of the pulsed array is found to be fall smoothly outside the main beam. From another aspect, the pressure field of the pulsed transducers have been experimentally validated and compared to the theoretically prediction [49], where the computed and measured on axis intensity is proved to be inconsistent with the continuous computation. Therefore, case by case numerical simulations are required to understand the pulsed transducer's operation in the near-field.

On the other hand, the characterization of the pressure field, including peak pressure and beam width, are of great significance in understanding the ultrasonic transducers and arrays. Visualization and mapping of the ultrasonic fields have been a research field itself for years. Schlieren

system [50, 51] is an optical system that has been widely used to visualize the ultrasound pressure field. In this method, the parallel beam of light diffracts as it travels through a medium with refractive index gradient produced by the propagation of an ultrasound wave. However, this method is limited to measure the pressure field normal to the light and the capabilities of the optical image analysis. Alternatively, using unidirectional and broadband microprobe or hydrophone to scan the pressure field is well-established, but it is time-consuming. Moreover, in these measurements, the instrument should be small in size to avoid disturbing the pressure field and averaging over a large transducer surface [52].

With the development of high frequency ultrasound array based on micromachining process, there has been an increasing demand to characterize the motions and pressure output of the micromachined transducers with high spatial resolution. However, limited by the hardware choices and available techniques, pulse-echo measurements have been frequently used to understand the signal amplitude and bandwidth of transducers. To understand the fluid coupled transducers, single point hydrophone measurement in fluid combined with motion stage have been the widely adapted to characterize the pressure field generated by capacitive micromachined ultrasonic transducers (CMUTs) , piezoelectric micromachined ultrasonic transducers (PMUTs), and micromachined bulk piezoelectric transducers [49, 50, 51]. However, transducers are packaged in coupling materials in real applications. These coupling layers have different material properties than the fluid used in measurements. Moreover, as the size of the surface of the hydrophones became comparable with the beam width of the pressure field generated by high frequency miniaturized transducers, the accuracy of the pressure amplitude and beam width will be largely affected. With the development of micromachined high frequency ultrasound systems, there is a pressing demand to accurately measure the time domain 2D pressure output at the surface of the high frequency miniaturized transducers package.

In this chapter, the acoustic performance of the PMUTs based ultrasonic fingerprint sensors operating in the near field with pulsed excitation were studied. The size of the PMUTs are comparable to the acoustic wavelength in the package and the package thickness [53, 6]. Here, k-Wave MATLAB toolbox [14] is used to model the output pressure field in the near field, taking the size of the acoustic source with pulsed excitation into account. Then LDV with a precision stage is used to measure the displacement on the surfaces of the package to characterize the motions to calculate the two-dimensional pressure field at the imaging plane of the ultrasound fingerprint sensor based on PMUTs. The model and measurements are consistent, leading to a reliable way to model and characterize the near field pressure generated by a PMUT array. Moreover, the crosstalk has been discovered in the LDV measurements at the transducers' plane, which helped to understand the crosstalk mechanism.

6.2   Method

In this section, we will first introduce the ultrasound fingerprint sensors fabricated with AlN MEMS bonded to CMOS process. Then the measurement instruments, measurement method, and the calculation used for 2D pressure and displacement mapping based on LDV measurements will be described. At the end of this section, the acoustic model using k-Wave MATLAB toolbox will be detailed.

6.2.1   Ultrasonic Fingerprint Sensors

The sensor was fabricated on a multi-project wafer using a commercial foundry manufacturing process where a MEMS wafer is bonded to CMOS wafer using Al-Ge eutectic bonding [12]. In this work, as shown in Figure 6.1, 35 μm diameter circular PMUT design was anchored by a 13 μm wide annular Al-Ge eutectic bond and has a 24 μm diameter circular Al top electrodes. Each PMUT is a piezoelectric unimorph composed of 1 μm thick AlN sandwiched between top and bottom metal electrodes on a single-crystal silicon layer with 1.7 μm nominal thickness, shown in Figure 6.1. The hexagonal layout of the array, as shown in Figure 6.1, enables close packing of the circular PMUTs, which are spaced on a 70×80 μm grid, resulting in a resolution of 376×318 dpi. In each sensor die, there are 65 columns with 42 PMUTs in each column. The Mo bottom electrode layer is patterned to electrically isolate each column of PMUTs. This enables the PMUTs to be used as 2-port devices, with the bottom electrode connected to high-voltage TX circuitry and the top electrode connected to low-voltage RX circuitry. Al-Ge eutectic bonds on SiO_2 standoffs provide the mechanical anchor and electrical contact to the PMUT. The detailed design study can be found in previous works [12, 53].

A 0.18 μm CMOS wafer with 24V high-voltage transistors provides signal-processing electronics, described in detail in [6]. The 42 PMUTs in each column share a common Mo bottom electrode that is connected to a high-voltage (24V) TX amplifier, and have individual top electrodes that are bonded to low-voltage (1.8V) receive circuitry. The TX waveform is a unipolar 24V, 2-cycle, 20 MHz pulse. One to five adjacent columns can be driven with and without beamforming. When beamforming is implemented, the TX signal is delayed symmetrically about the center column with a delay pattern (0, Δt_1, Δt_2, Δt_1, 0), where Δt_1 and Δt_2 are time delays programmable in 10 ns increments and selected to give a desired focal distance.

As shown in the optical image in Figure 6.2, the sensor is wire bonded onto a customized PCB, where the wire bonds were protected by glob top. The fingerprint image is measured based on the reflection of ultrasound from the surface of the finger. To achieve a high contrast ratio, the 4.6 mm $\times$ 3.2 mm bonded sensor surface was coated with a 250 μm thick layer of poly-
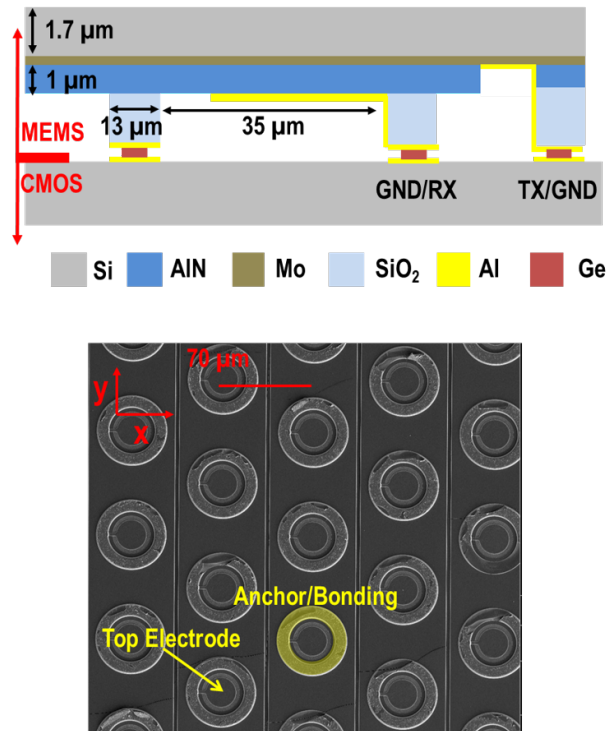
Figure 6.1: The schematic layout of the cross-section of a single PMUT (top) and the SEM image of the PMUT array (bottom), viewed from the top electrode side after debonding from the CMOS die. The 35 μm diameter circular PMUTs are arranged on a 70×80 μm grid and have a 24 μm diameter circular top electrode. Al-Ge eutectic bonds on $2.35\mu m$ thick SiO2 standoffs provide the mechanical anchor and electrical contact to the PMUT. The lines between the PMUT columns show where the AlN and Mo bottom electrode layers are etched to electrically isolate each column.

dimethylsiloxane (PDMS) (Sylgard 184, Dow Corning) to provide an acoustic coupling layer with similar acoustic impedance to human tissue. During pulse-echo fingerprint imaging, each PMUT is driven electrically and acts as an individual acoustic source, transmitting pressure into PDMS. At the finger-PDMS interface, the acoustic reflectance at finger valley-PDMS interface is significant larger than that at finger ridge-PDMS interface. The pressure under finger valley-PDMS is reflected back onto PMUT surface exciting PMUT and generate an electrical output. This work focuses on the acoustic domain characterization, the detailed electrical and pulse-echo measurements can be found in [6, 53].
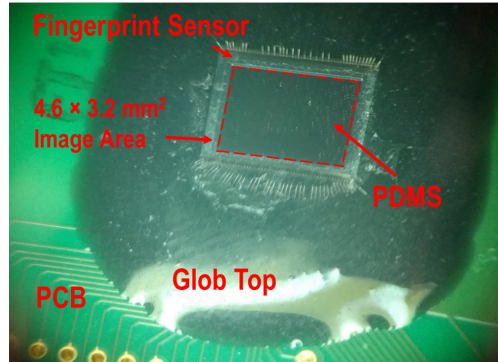
Figure 6.2: The optical image of the packaged fingerprint sensor. A 250 μm thick PDMS coupling layer coats the PMUT array.

6.2.2 Measurement System

In this chapter, UHF-120 Ultra-High-Frequency Vibrometer (UHF-120, Polytec) with a precision positioning stage (A-PST-200P, Polytec) were used. UHF-120 is an interferometer and laser doppler vibrometer (LDV) to measure out-of-plane vibration up to 1.2 GHz. UHF-120 consists of a sensor head, a controller, an oscilloscope, and a personal computer to operate the data management system for signal processing. With a 20 times zoom factor lens, the spot diameter of the green laser is 2.5 μm. As illustrated in Figure 6.3, during the measurements, the precision positioning stage would move the device under test following a preset grid set by the user and record the coordinates of each single point measurement. At each location, the laser doppler vibrometer will measure, digitize, signal process, and record the time domain displacement. Combining all the single point displacement measurements with their coordinates, a 2D time domain displacement map of a preset grid can be reconstructed for the surface where the laser is focused on. The laser can be focused on either the PDMS surface or the PMUTs surface of the fingerprint sensor, which makes it possible to measure the 2D deformation over time at both the PMUTs surface and PDMS surface. After the displacement measurements at the top of PDMS, the pressure field can be computed from the measured deformation by multiplying the measured velocity by the acoustic impedance of PDMS (density ρ_0= 1040 kg/m_3 and speed of sound c_0= 1000 m/s),

$$p(x, y) = \rho_0 c_0 u(x, y)/2, \tag{6.1}$$

where the factor of two in the denominator corrects for the free boundary at the PDMS surface. For the measurements through PDMS and focusing on the PMUT surface, the reflective index of PDMS was used to correct the measurements. The noise floor of the displacement measurements is around 10 pm, corresponding to an error of 1.5kPa calculated pressure.
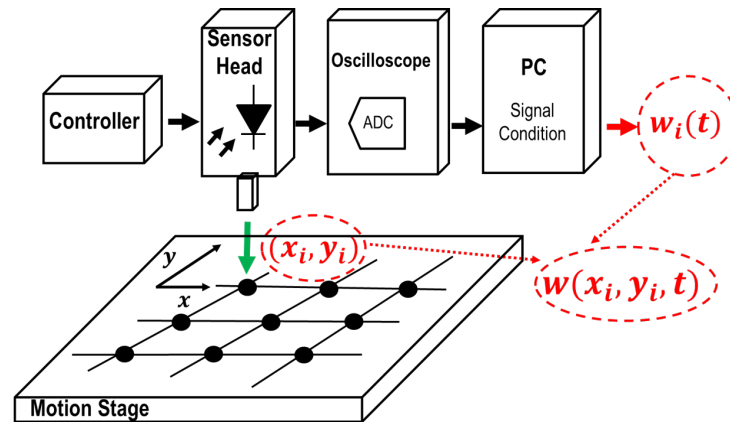
Figure 6.3: Optical image of Polytec's UHF-120 Ultra High Frequency Vibrometer (top) and the block diagram of the LDV measurement cycle (Bottom). Using all the single point displacement measurements with their coordinates, a 2D displacement map of a preset grid on the optically focused surface can be reconstructed.

6.2.3 Acoustic Field Modeling

k-Wave MATLAB Toolbox is used to simulate the pressure field [14] In the k-Wave simulation, 250 μm thick PDMS acoustic domain were modeled. On the bottom of the acoustic domain, the 35 μm diameter PMUT is modeled as a 35 μm × 35 μm rectangular piston acoustic source on a 70×80 μm grid with uniform displacement of $\frac{1}{3} w_p$, where w_p is the peak displacement of the PMUT operating in the PDMS. Each rectangular piston is assigned a 2-cycle 20 MHz displacement with time delay. The time gated pressure field with the maximum pressure field output on top of the 250 μm thick PDMS layer is extracted to compare with the experiment measurements. Using the k-wave model, the effect of the spacing of the PMUT array on the near-field acoustic field is studied. The pressure field along one column of equally spaced 20 MHz PMUT array in PDMS with difference spacing is plotted in Figure 6.4. Pressure outputs from one column of PMUTs with one to seven times wavelength spacing were compared to a continuous array and individual PMUT transducer. As shown in Figure 6.4, the individual 15 μm radius transducer with $ka < 1$ is very directional and has side lobes. The different spacing of the transducer will lead to different interference of the main lobe and side lobes. In general, the pressure output amplitude decreases as the spacing increases, where the maximum amplitude is from zero spacing or a continuous linear array. As a result of the individual PMUT's finite size and PDMS package height when compared to the wavelength, the pressure field will present a periodic pattern on top of the package. Constraint by the design rule, the PMUTs array spacing used in this fingerprint sensor is designed to be between one to two wavelengths.
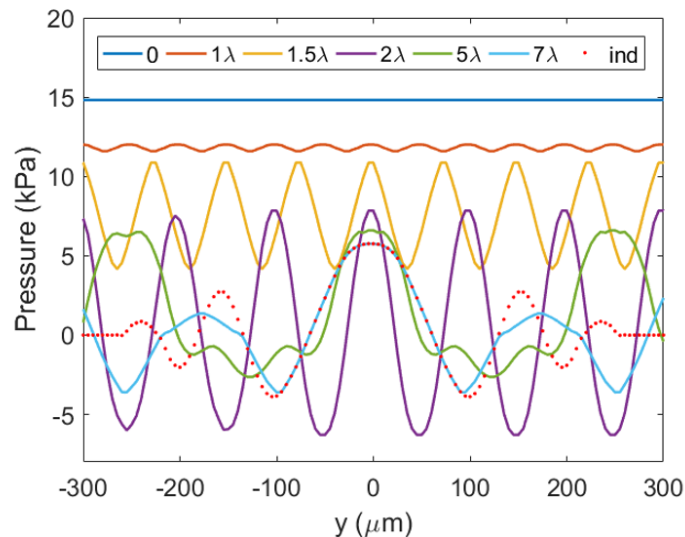
Figure 6.4: k-Wave MATLAB Toolbox is used to model the pressure field on top of the PDMS
package along one column of equally spaced 20 MHz PMUTs with difference spacing.

6.3   Results

In this section, the pressure calculated from displacements measured by LDV was first validated
with hydrophone measurements. After the validation, 2D fingerprint sensor pressure measure-
ments were used to characterize the pressure field at the top of PDMS surface with and without
beamforming. Then the displacement measurements at PMUTs surface were used to understand
the motion of transmit PMUTs, adjacent PMUTs, unsupported membranes, and PMUTs anchors.

6.3.1   LDV Based Pressure Measurements Validation

The pressure measurements based on displacement measurements via LDV is first validated by
comparing to the pressure measurements using a calibrated 40 μm diameter needle hydrophone
(Precision Acoustics) for a fingerprint device without PDMS package operating in non-conducting
fluid FC-70 (Fluorinert, 3M). In each measurement, the same 5 columns of PMUTs were driven
with unipolar 24V, 2-cycle, 14 MHz pulses without beamforming. The pressure outputs at around
750 μm away from the PMUT array were measured and compared. In the hydrophone measure-
ments, the needle hydrophone is immersed and moved to 750 μm away from the PMUT array.
Then the pressure field was measured on a 100 μm scan grid with a motion stage (NSC-G3 New-
mark Systems, Inc). In the LDV measurements, the fluid level of FC-70 was adjusted to be around
750 μm above the PMUT array. A 50 μm scan grid was used in the scanning LDV measure-
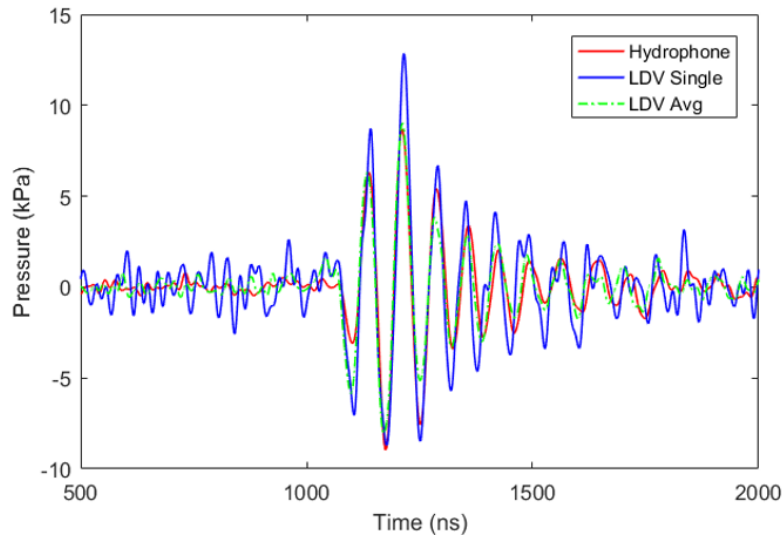
Figure 6.5: Pressure measurements in FC-70 at 750 μm away with hydrophone and LDV. The single point LDV measurements (LDV Single) is 40% higher than the hydrophone measurements, while the averaged pressure from nine points measured with LDV (LDV Avg) was consistent with single point hydrophone measurement.

ments. The maximal pressure outputs of the maximum single point pressure measurements were time shifted and compared in Figure 6.5, labeled as hydrophone and LDV Single. To understand the 40% difference, nine scan points measured with LDV on a 50 μm grid centered around the maximum pressure point were then used to calculate the averaged pressure and labeled as LDV Avg in Figure 6.5. The averaged pressure amplitude and waveform was very close to the single point hydrophone measurements, which validated the accuracy of the LDV based pressure measurements. However, as the beam width of the pressure field is comparable to the size of the hydrophone sensing surface, the measured pressure is an average of the pressure of the total area, which becomes non-neglectable for high frequency pressure field characterization. In this case, the 2.5 μm laser spot used by the LDV lead to a high resolution to characterize the pressure field on top of a packaged dense high frequency transducer array.

6.3.2   2D Fingerprint Sensor Pressure Measurements

The two-dimensional pressure field at the PDMS surface was modeled and characterized as descripted in the previous sections. The measured and modeled pressure fields for single-column TX with 2 cycle 20 MHz input are shown in Figure 6.6. The measured pressure field showed an around 10 kPa peak pressure and -5 kPa pressure on the first side lobe, which is about 80% of that from the model. However, the measured 110 μm 3 dB beam width along x axis, a side lobe about 110 μm

Figure 6.6: Modeled (top) and measured (middle) pressure output on top a 250 μm thick PDMS when 1 column 42 PMUTs were exited with 2 cycle 20 MHz electrical pulse input. The measured and modeled pressure field along x axis (bottom) are consistent.

away from main lobe along x axis, and a pressure field with about 80 μm periodicity along y-axis are consistent with that of the model. Here the 80 μm periodicity along y-axis is due to the near field pressure output from directive ultrasound transducers with about two wavelengths spacing, which is consistent with the results in Figure 6.4.

The measured and modeled pressure fields for 5-column TX with beamforming is shown in Figure 6.7. The measured peak pressure is 26 kPa with about 60 μm 3 dB beam width along x axis, which is consistent with that from the model. However, the amplitude and the location of the side lobe along the x axis as well as the continuous pressure field along the y axis is different from that from what the model predicts. The difference could be explained by the additional membrane motion from crosstalk that will be discussed in detail in the later sessions.

Figure 6.7: Modeled (top) and measured (middle) pressure output on top a 250 μm thick PDMS
when 5 columns 42 PMUTs were exited with 2 cycle 20 MHz electrical pulse input with beam-
forming. The measured and modeled pressure field along x axis (bottom) showed a consistent
main lobe.

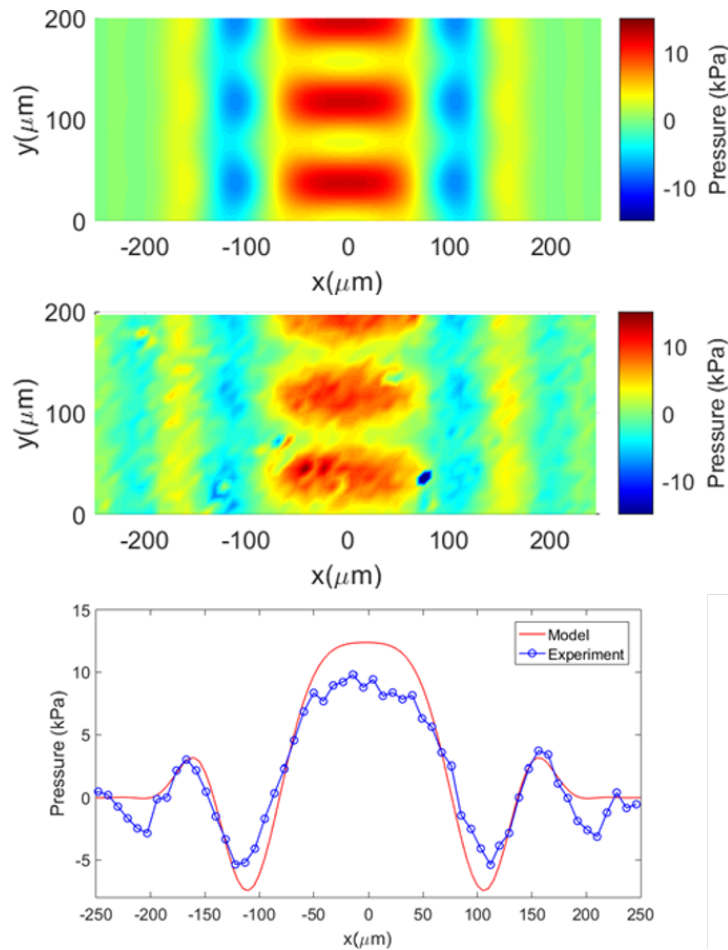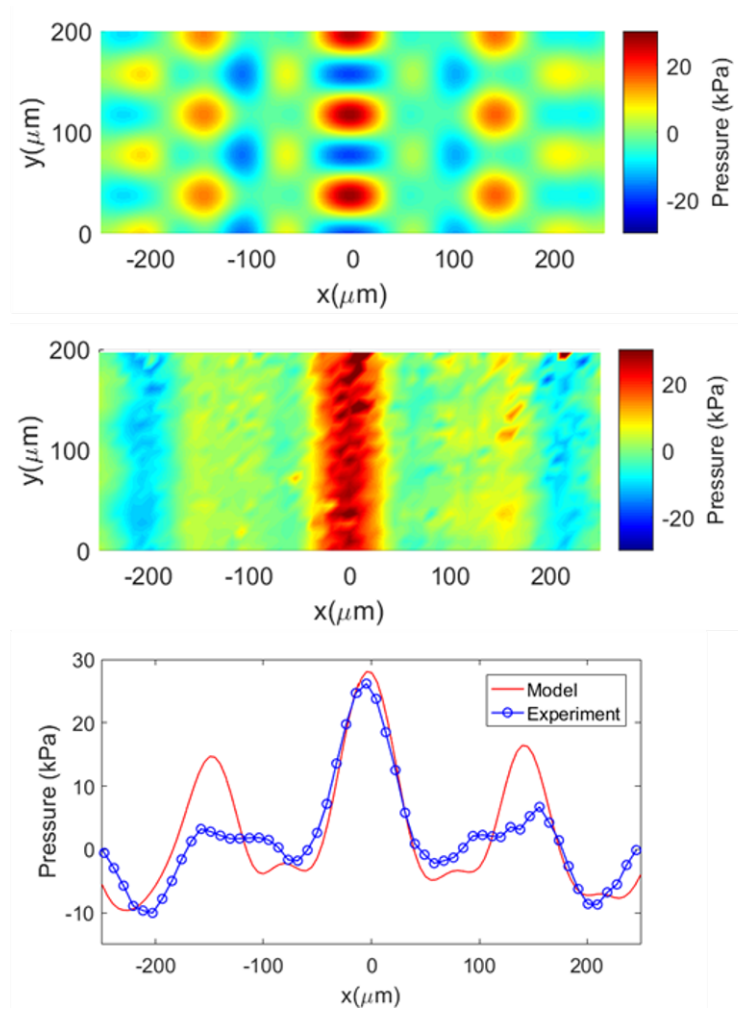The measured and modeled pressure fields for 5-column TX without beamforming is shown in Figure 6.8. The measured pressure field, Figure 6.8d, showed a large difference to the modeled pressure field, Figure 6.8b. The modeled pressure field predicts periodical localized pressure, where the measured pressure field is rather uniform. The difference can be attributed to crosstalk. Crosstalk arises both from Rayleigh-Bloch waves traveling at the PDMS-silicon interface [12] and due to mechanical coupling in the thin AlN-Si layer between neighboring PMUTs [42]. The crosstalk leads to additional acoustic pressure generated from the motion of the adjacent PMUTs and unsupported membranes. These motions lead to additional acoustic source that are not modeled. More discussion of these crosstalk mechanism will be in next section. In order to understand the effect of the additional membrane motion, 15 μm size equivalent piston acoustic source were added at the location of the free membrane between the individual PMUTs, as shown in Figure 6.8a. The modeled pressure field with crosstalk, shown in Figure 6.8d, shows a uniform pressure output similar to the measured pressure in Figure 6.8c. Moreover, as shown in Figure 6.8e, the modeled pressure field with crosstalk along the x axis has the same profile along the x axis as that from measurement, where the difference in amplitude can be attribute to the grouping of the acoustic crosstalk to rectangular equivalent acoustic source being excited at the same time. The addition of the equivalent acoustic sources in the model make the difference between the modeled and measured pressure field smaller. This proves that crosstalk from additional membrane motion will influence the pressure field significantly. The effect of the crosstalk on pressure output can only be accurately captured with simulations including the interaction of the Si membrane and PDMS package.

6.3.3   Characterization of Packaged PMUTs

The motion at the PMUT plane was measured by focusing the laser point on the silicon surface through PDMS to understand the transmit, crosstalk, and the receive characteristics. The change of the optical path measured through the PDMS package is both a result of the PMUTs motion and photoealstic effect of the generated pressure field in the PDMS. The estimated displacement resulting from photoelastic effect is calculated using stress optic law to be around 5 pm using the surface pressure generated by PMUTs. This is negligible in this chapter when compared to the measured displacements on the PMUT surface. For measurements on silicon plane, the focus is on the motions of the transmit PMUT, adjacent PMUT, and the unsupported membrane between the two PMUTs, as illustrated in Figure 6.9a. The 2D displacements of four time slices were plotted in Figure 6.9b, including the time slice of the maximum displacements of the transmit PMUTs (t=114.8 ns), the unsupported membrane (t=133.4 ns), the adjacent PMUTs (t=206.8 ns), and the receive PMUTs (t=587.6 ns). From the first three 2D displacements during and after PMUTs' TX, we can clearly see that the unsupported membrane and the adjacent PMUTs were excited. The time domain displacements at the center of the cells enclosing the transmitting PMUT, adjacent PMUT, and the unsupported membrane were plotted in Figure 6.9c. The peak displacement of the unsupported membrane and adjacent membrane are 2% and 15% that of transmitting PMUT and
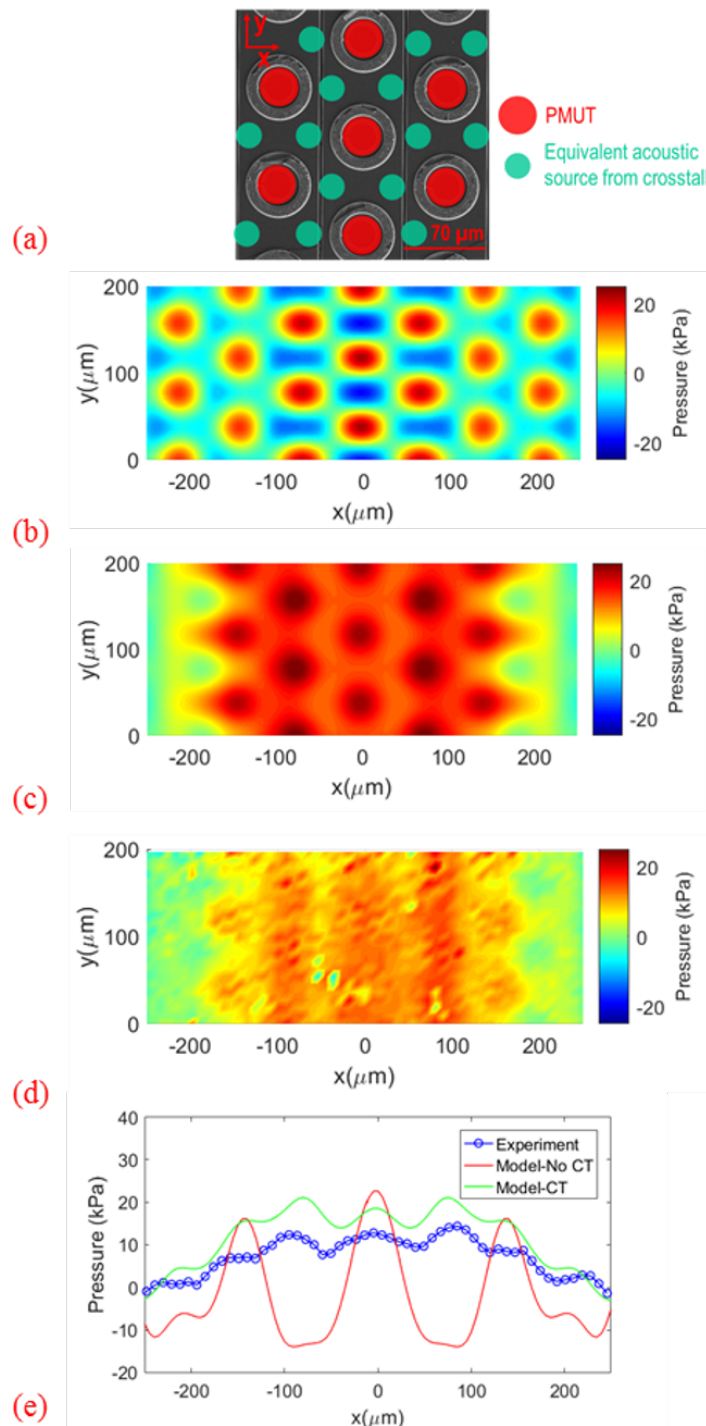
Figure 6.8: Illustration of the modeled transducer array with and without equivalent acoustic source from crosstalk (a). Modeled pressure output at 250 μm thick PDMS without (b) and with crosstalk(c). Measured pressure output with LDV(d). Measured and modeled pressure field along x axis (e.).

were about 20 ns and 90 ns delayed respectively. Meanwhile, the 2D displacements at receiving
(t=587.6 ns) were plotted in Figure 6.9b. The unsupported membranes seem to have a similar
amplitude and mode shape with the circular PMUTs. Based on the FEM model, shown in Figure
6.10, the unsupported membranes between the ring anchors have an effective diameter of 36.5 μm,
which lead to an eigen mode at 25.1 MHz. This eigenfrequency is close to that of the circular
PMUTs at 28.2 MHz. As the quality factor of the packaged transducers is around two, both mode
shapes were excited by the returned pressure.

The crosstalk from the adjacent PMUTs and the free membranes were further characterized
by driving a single column of PMUTs. The PMUTs motion in PDMS for single-column trans-
mission with 2 cycle 20 MHz 24V input were measured and shown in Figure 6.11. As labeled
in Figure 6.11, number one PMUT is the transmitting PMUT, while number two, three, and four
PMUTs were adjacent PMUTs in the next few columns. Number three PMUT, 140 μm away
from the transmitting PMUT, has 7% peak displacement of that of transmitting PMUT. The mo-
tion of number three PMUT is 206 ns later than that of the number one PMUT, suggesting a wave
travelling at PDMS and silicon interface with a speed of sound of 680 m/s. This speed of sound
is smaller than the speed of sound in bulk PDMS, which agrees with the characteristics of the
Rayleigh-Bloch waves reported in [54]. The behavior of the adjacent PMUTs and unsupported
membrane were further characterized in air for single-column transmission with 2 cycle 20 MHz
24V input as shown in Figure 6.12. The locations of the transmitting PMUTs, adjacent PMUTs,
and the unsupported membrane were labeled in Figure 6.12a. The 2D displacements of PMUTs at
the transmitting (t=160 ns) and crosstalk (t=1877 ns) phases were shown in Figure 6.12b. The time
domain displacements for the transmit PMUT, adjacent PMUT, and the unsupported membrane
were plotted in Figure 6.12c. The transmitting PMUT started to ringdown after the two-pulse in-
put, while the adjacent PMUT in air started to ring up 300 ns later. The adjacent PMUTs in air
were excited 200 ns later than that in fluid, suggesting a three times slower speed of sound. The
adjacent PMUTs' peak displacement after fully ring up is about 20% of that of transmit PMUT.
Meanwhile, the unsupported membrane's average displacement without package is around 16 pm,
close to the noise in these measurements. This agrees with our previous reasoning as there is no
fluid and solid surface for Rayleigh-Block waves to propagate.

The anchor motions were discovered for PMUTs packaged in PDMS, shown in Figure 6.13.
The peak and anchor displacement comparison in air and in PDMS is shown in Figure 6.13. In
these plots, the displacement of the anchor at 25 μm away from the center of the PMUT circular
membrane was used. As shown in Figure 6.13, the anchor displacement in PDMS is about 15%
of that of transmit PMUT in PDMS, while the average anchor displacement for anchor in air is
negligible. Using the anchor displacements, the pressure field on top of the anchor can be estimated
as 6 kPa. This agrees with the expected pressure amplitude at the silicon and PDMS surface.
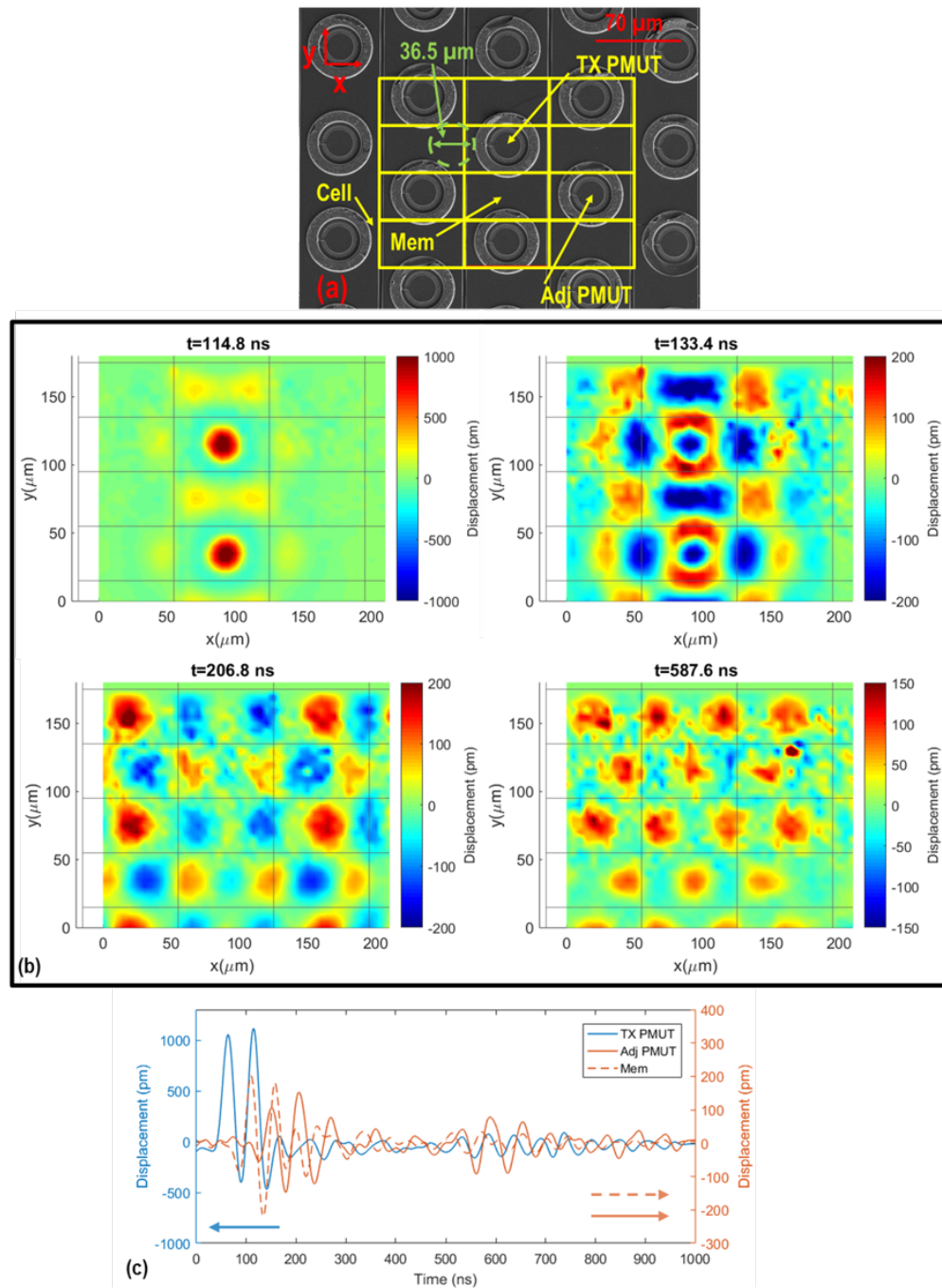
Figure 6.9: The motion of the transmit PMUT, adjacent PMUT, and the unsupported membrane between the two PMUTs in PDMS were characterized. (a) The locations were labeled on the SEM image (b) The 2D displacements of four time instances with the maximum displacements of the transmit PMUTs (t=114.8 ns), the unsupported membrane (t=133.4 ns), the adjacent PMUTs (t=206.8 ns), and the receive PMUTs (t=587.6 ns) (c) Time domain displacements of the transmit PMUT, adjacent PMUT, and the unsupported membrane
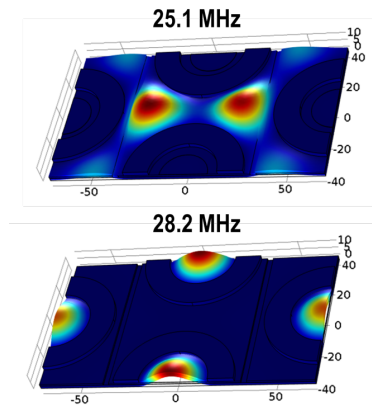
Figure 6.10: FEM simulation of the eigen frequencies and mode shapes of the PMUTs array. The unsupported membrane between the ring anchors with an effective diameter of 36.5 μm leads to a eigen mode at 25.1 MHz (top), while the eigenfrequency of the circular PMUTs is 28.2 MHz (bottom).
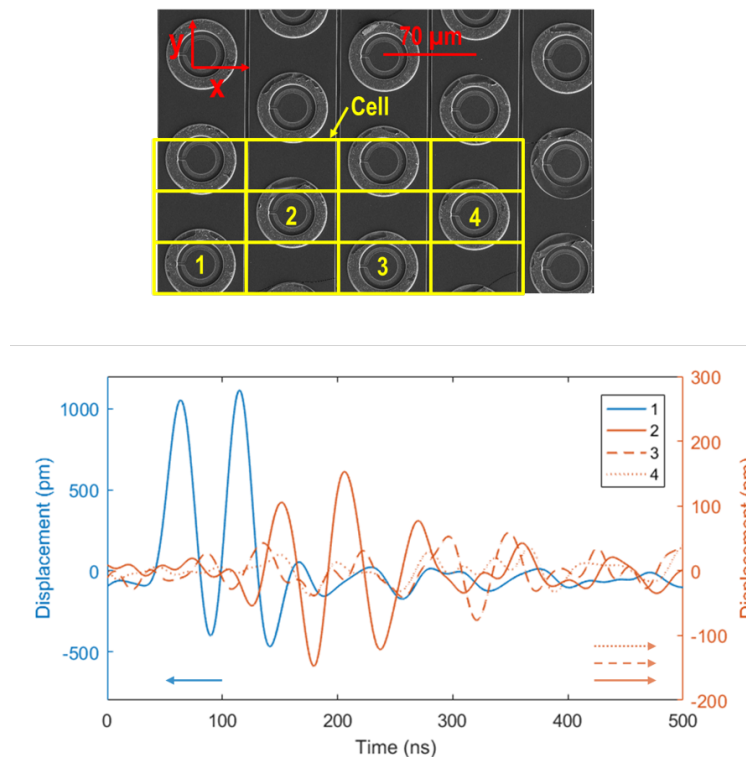
Figure 6.11: The motion of three adjacent PMUTs next the transmitting PMUT were characterized. (Top) The location of the four PMUTs labeled on the SEM image (Bottom) Displacement of the four PMUTs.
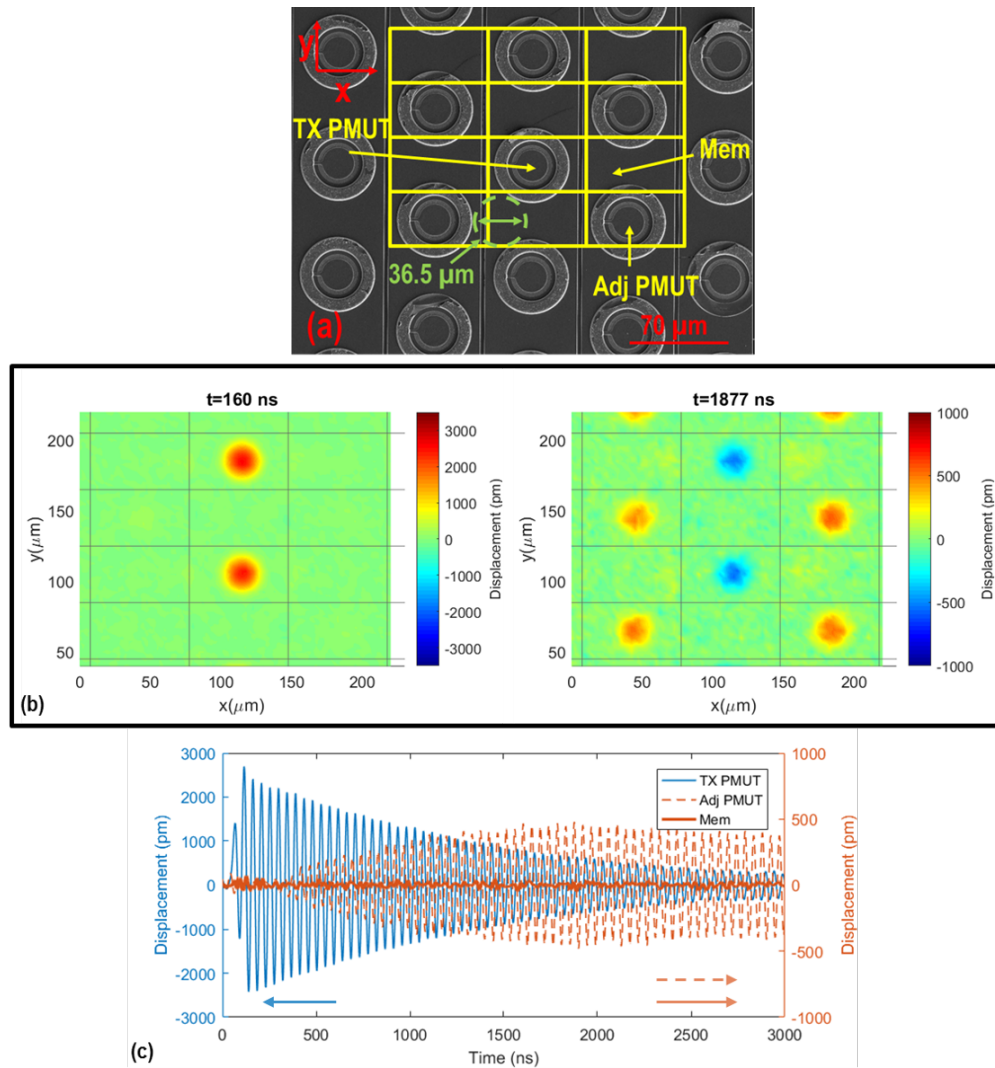
Figure 6.12: The motion of the transmit PMUT, adjacent PMUT, and the unsupported membrane
between the two PMUTs in air were characterized. (a) The locations were labeled on the SEM
image (b) The 2D displacement at the end of the second drive pulse (t=160 ns) and the peak dis-
placement of the adjacent PMUT (t=1877 ns) (c) Displacements of the transmit PMUT, adjacent
PMUT, and the unsupported membrane
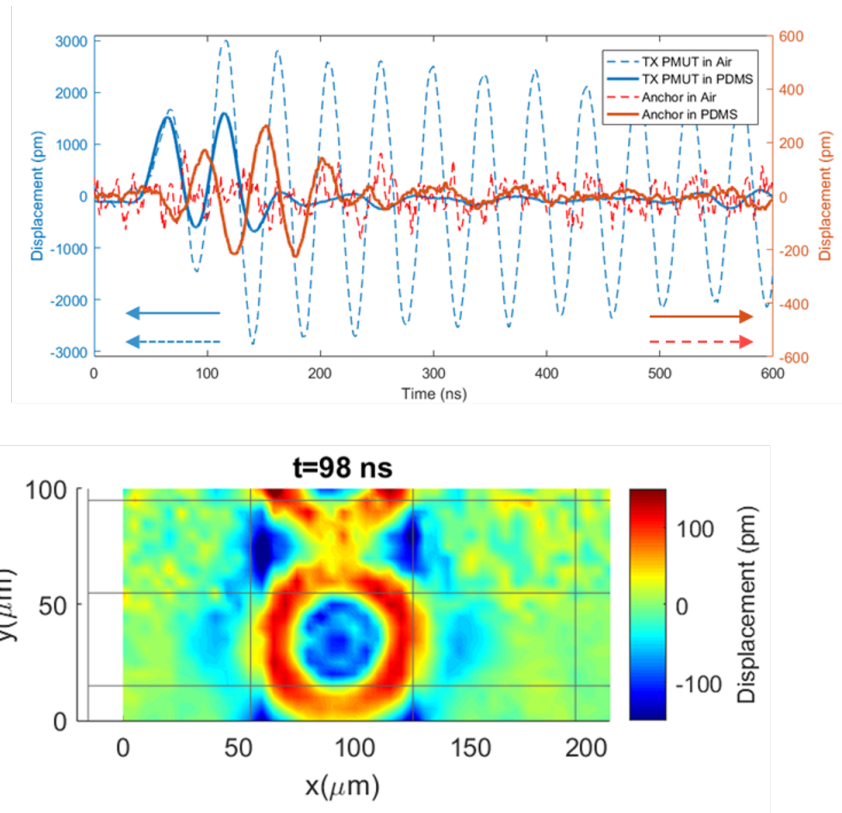
Figure 6.13: The anchor motion is discovered for PMUTs operating in PDMS. Top: The transmit
and anchor displacements in air and in PDMS. Bottom: The 2D displacement at the anchor peak
displacement (t=98 ns).

6.4 Conclusion

PMUTs based ultrasound fingerprint transducer requires a case by case time domain simulation,
because the pulsed acoustic sources were used to image in the near field as well as the size of the
PMUT acoustic source is comparable to the acoustic wavelength and package thickness. Here,
k-wave MatLab toolbox is used to model the time domain near field pressure field. The two-
dimensional pressure field mapping based on displacement measurements using scanning LDV
have been used to validate the model and demonstrated as a powerful technique to characterize the
time domain 2D pressure output of packaged high frequency miniaturized transducers. Moreover,
the measured motions on the silicon plane suggested motions of the adjacent PMUTs and unsup-
ported membrane resulting from crosstalk, which demands careful consideration for miniaturized
transducer design.

Chapter 7

Improving PMUT Transmit Performance via Sub-Micron Thickness Scaling

7.1   Introduction

The development of AlN PMUTs have enabled new applications such as gesture recognition and ultrasonic fingerprint sensor. The signal to noise ratio and penetration depth requirements in these applications gave rise to extensive efforts in improving the transmit performance of the PMUT. A various of piezoelectric materials, PMUT device design, microfabrication process, and device thickness have been explored to improve the PMUT array performance. Piezo material, such as Scandium-doped AlN and PZT, have been used on PMUTs for their high piezo coefficients [35, 55]. Dual-electrode bimorph and dome shaped PMUTs designs have been investigated to improve the electromechanical coupling [56, 57]. New microfabrication process, such as surface micromachining, has been developed to improve the fill factor of the transducer array [58]. The effects of thickness scaling have been explored in previous work by comparing the transmit performance of two different PMUT thicknesses that are thicker than 2 μm [59]. In this chapter, analytical model and experiment measurements were used to demonstrate that individual PMUT's transmit sensitivity at a given frequency is inversely proportional to the device thickness. Sub-micro thick piezoelectric layer devices were fabricated to further improve the transmit performance. At the end of this chapter, the constraints of the thickness scaling will be discussed.

7.2   Design and Modeling

7.2.1   Acoustic Modeling

The classical axial far field pressure field $P_{ax}(r)$ from a circular piston assuming the distance is much larger than the Rayleigh distance ($R_0 = A/\lambda$) is [24]

$$P_{ax}(r) = \rho c v_0 \frac{A_{cir}}{\lambda r}, \tag{7.1}$$

where ρ and c are the density and speed of sound of the acoustic medium, v_0 and A_{cir} are the vibration velocity and the area of the circular piston, λ is the wavelength, and r is the distance from the source. However, as the MUTs device size and package height are comparable to the wavelength, their performance cannot be captured by the classical axial far field pressure analytical model. In this case, the classical model only provides an intuitive understanding of the factors impacting the pressure output. Based on equation (1), the pressure output of pulsed MUTs array is assumed to be determined by the individual device performance, array size, and fill factor ($FF = \frac{(active\ area)}{(total\ area)}$). Time domain finite element simulation with k-Wave MATLAB Toolbox is used to understand the effect of these factors [14]. 50 μm wide rectangular piston acoustic sources with 10 pulse 5 MHz 1 nm displacement were simulated with different spacing and array area in PDMS (density ρ_0= 1040 kg/m^3 and speed of sound c_0= 1000 m/s). Firstly, 300 $\mu m \times$ 300 μm array with different fill factor were simulated by changing the total number and spacing of the rectangular piston sources. The far field pressure output in the simulation is within 10% of the analytical calculation from equation (1). As shown in Figure 7.1, the peak pressure generated by the same array size with different fill factor were at the same distance away from the array. This is consistent with that the Rayleigh distance only depends on source area and wavelength. On-axis peak pressure and far field pressure at 800 μm away is used to understand the relationship between fill factor and on-axis pressure output. As there is no pressure output without any transducers, a linear fit to data with intercept at origin is used in the analysis. Both the peak and far field pressure showed a linear relationship ($R^2 > 0.98$) with the fill factor. Based on the linear relationship, pressure output from transducer array with a 100% fill factor is consistent with that from an individual piston transducer. Meanwhile, the effect of the array area is investigated. 45% fill factor array with different array sizes were simulated. As shown in Figure 6.2, the on-axis peak pressure is at different distance due to the different array area. The axial far field pressure at 800 μm away showed a linear relationship to the area array with $R^2 > 0.98$. In these simulations, the PMUTs' displacement is assumed to be independent of the fill factor. However, the fill factor will change the mutual acoustic impedance of the array, which results in a change in PMUT velocity [60]. There effects are not discussed in this chapter. At this point, we have demonstrated the axial far field pressure output linearly scales with array area, fill factor (FF), and the transducer peak displacement w_p. Most of the time, the array area is determined by the application requirement, while the fill factor is limited
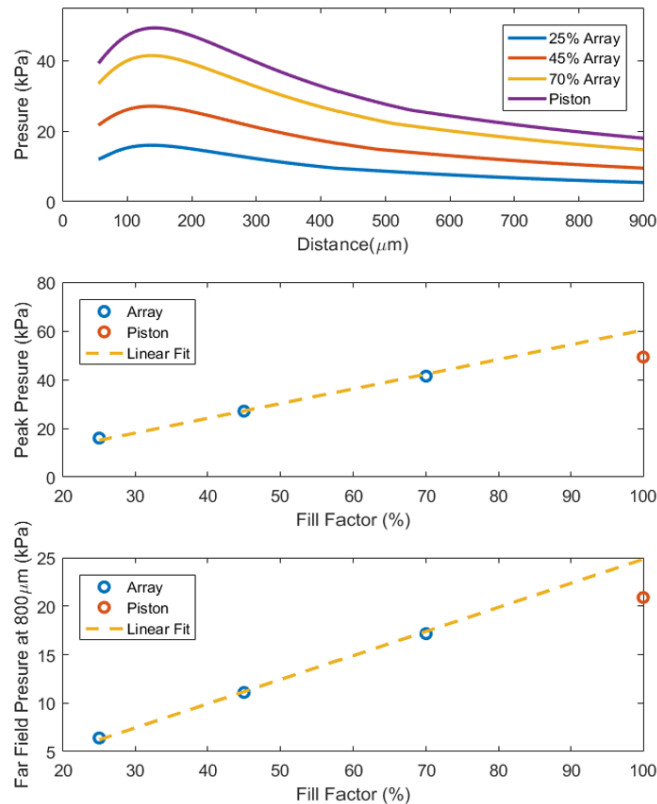
Figure 7.1: Simulated pressure field (top) using 50 μm rectangular piston acoustic sources with
10 pulse 5 MHz 1 nm displacement with same area but different spacing in PDMS. Extracted
peak pressure (middle) and far field pressure at 800 μm away (bottom) linearly scales with the
fill factor of the array.

by the minimal spacing requirement of the microfabrication process. Therefore, we will focus on
the thickness optimization of the individual PMUT to improve the PMUT displacement in this
chapter. The impact of minimal spacing requirements on the fill factor as thickness scales down
will be discussed in the end.

7.2.2 Device analytical Modeling

The equivalent circuit model for PMUT has been studied [23]. For ultrasonic application, the oper-
ating frequency is determined by the application's requirement on axial resolution and penetration
depth. Therefore, the performance optimization for circular PMUTs at a given resonant frequency
is needed. Here the static displacement per input voltage w_s, defined as peak displacement w_p
normalized by Q, is used as the figure of merit to eliminate the effect of Q. For a PMUT with AlN
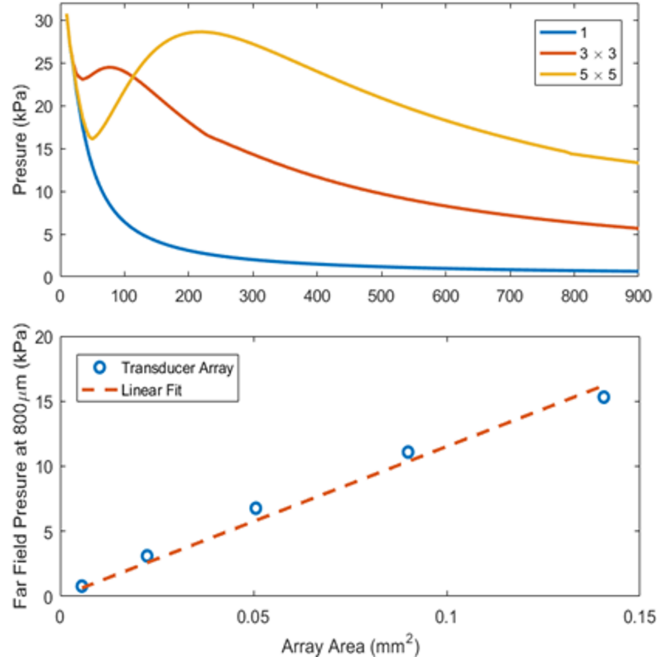
Figure 7.2: Simulated pressure field (top) with different array area in PDMS. Extracted far field
pressure at 800 μm away (bottom) linearly scales with the area of the transducer array.

as both the active and piezoelectric layer, the resonant frequency f is

$$f = K \frac{t}{a^2}, \tag{7.2}$$

where t is the total device thickness and a is the radius of the circular PMUT and

$$K = \frac{10.327}{2\pi} \sqrt{\frac{E}{3\rho}}, \tag{7.3}$$

is a constant defined by the young's modulus E and density ρ of AlN. Based on equation 7.2, the
ratio of $\dfrac{t}{a^2}$ is fixed at a given frequency. Then the static displacement w_s at a given frequency can
be simplified as

$$\frac{w_s}{V_{in}} = \frac{\eta}{k} \propto \frac{\gamma^2(\gamma^2 - 1)e_{31,f}K}{ft} \tag{7.4}$$

where $e_{31,f}$ is the transverse effective piezoelectric coefficient and γ is the electrode coverage.
Based on this, for PMUT, the static displacement at a given frequency linearly scales with trans-
verse effective piezoelectric coefficient, while it is inversely proportional to the frequency and total
device thickness, as shown in Figure 7.3. This suggests the transmit performance improves as the
thickness scales down for a given piezoelectric material and operating frequency.
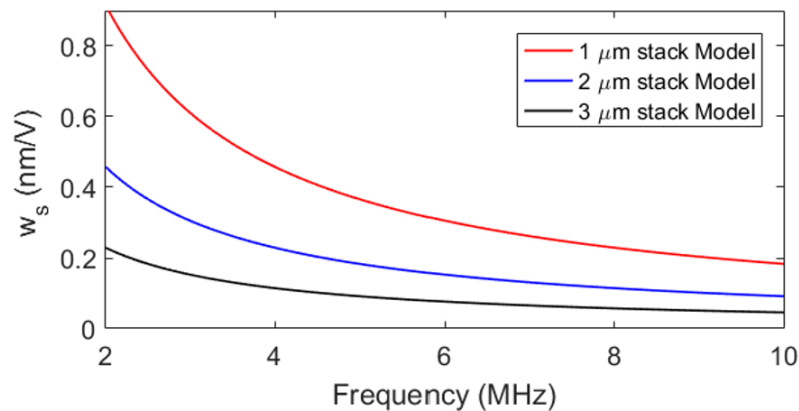
Figure 7.3: The analytically modeled static displacement at a given frequency is inversely proportional to the total film thickness and frequency.

7.3 Device Characterization

7.3.1 Fabricated Device

As shown in Figure 7.4, 29 μm and 40 μm radius PMUTs with 1.4 μm and 2.4 μm thick AlN films were fabricated on a surface micromachining process to compare the transmit performance at similar frequencies [61]. Rocking curve measurements were done on the AlN piezoelectric layer. The FWHM is $2.2°$ and $1.68°$ for the 0.7 μm and 1.2 μm thick piezoelectric layer respectively. Based on [62], the piezoelectric coefficient should be within 20% difference for the two piezoelectric films.

7.3.2 Device Measurement

The PMUTs' frequency response in air were measured with laser Doppler vibrometer (LDV). Curve fitting is used to extract the measured frequency in air, peak displacement, and Q. The static displacement is calculated as peak displacement normalized by Q. As shown in Figure 7.5, the measured displacement in air can be modeled as a second order linear system accurately. The extracted static displacement w_s is plotted as a function of frequency in Figure 7.5. The dotted lines are the modeled static displacement using 0.7 μm and 1.2 μm as the piezoelectric layer thicknesses. The measured static displacement are within 30% of that predicted by the model. For the 0.7 μm thick piezoelectric layer devices, the static displacement of 2.57 MHz device is 2.6 times that of 5.66 MHz, which is consistent with the 2.2 times difference in the frequency. While for the
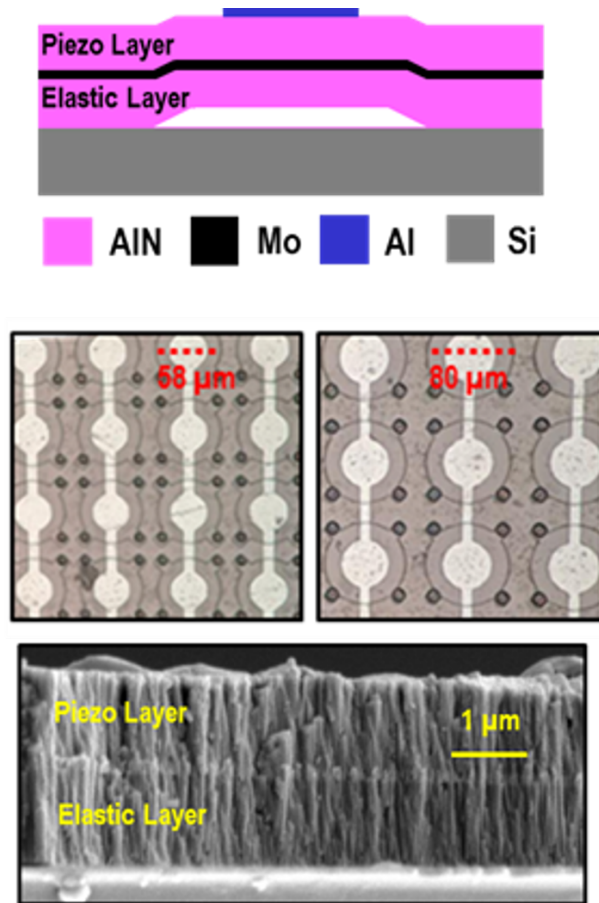
Figure 7.4: Schematics of the fabricated PMUT (top). The optical image of the fabricated 29 μm and 40 μm radius PMUTs (middle). The cross-section SEM of the fabricated 1.2 μm thick piezoelectric layer device (bottom).

1.2 μm thick piezoelectric layer devices, the static displacement of 6.88 MHz device is 1.7 times that of 12.1 MHz, which is consistent with the 1.8 times difference in the frequency. The resonant frequency in air of the 40 μm radius PMUTs on 1.2 μm thick piezoelectric layer is 20% larger than 29 μm radius PMUTs on 0.7 μm thick piezoelectric layer. As the pressure output linearly scales with velocity $P \propto v = 2\pi f w_p$, a figure of merit for transmit performance is defined as $FOM = w_s f$, where $FOM \propto e_{31,f}/t$ based on Equation 7.4. As shown in Figure 7.5, the figure of merit FOM of the PMUTs with 0.7 μm piezoelectric layer is about 1.5 to 1.7 times better than that with 1.2 μm piezoelectric layer. This matches the model considering that the FWHM measurements suggest 20% difference of the piezoelectric coefficient for the two films. The variation of the FOM of the devices on the 0.7 μm thick piezoelectric layer is roughly 20%. This can be attributed to the mechanical boundary condition of the PMUT, as the device performance is more sensitivity to the boundary condition with smaller radius.
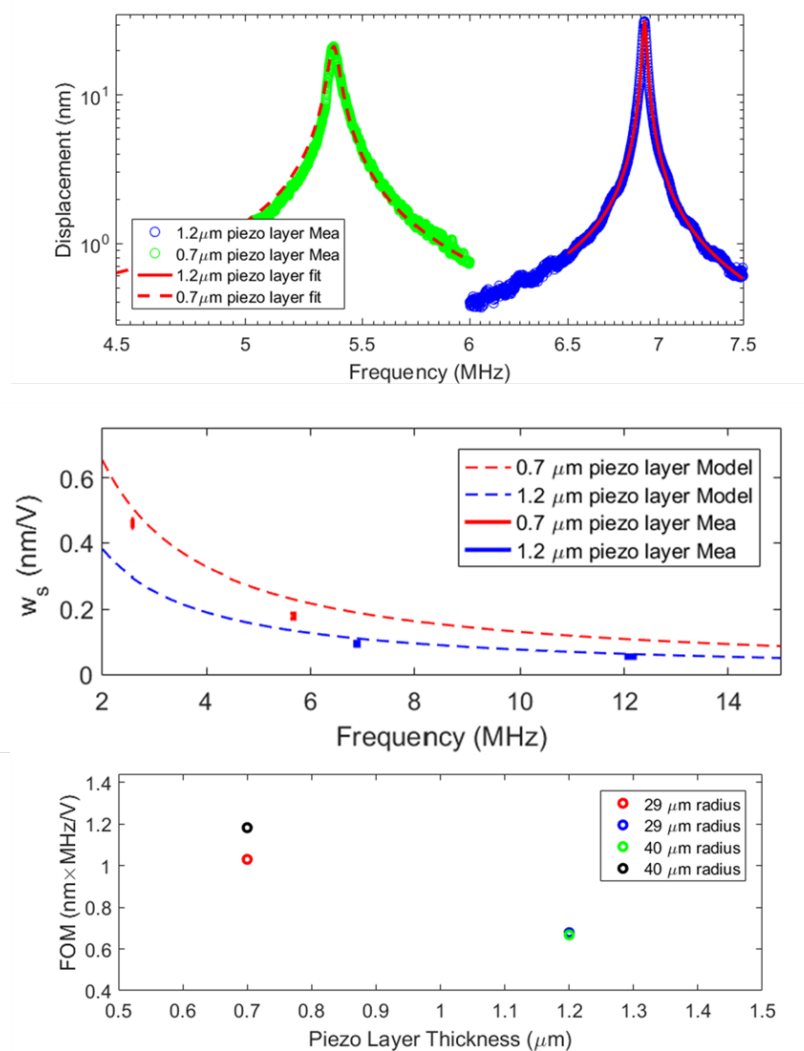
Figure 7.5: The PMUTs' measured and curve fitted frequency responses in air (top). The modeled and measured static displacement plotted as a function of frequency (middle). The measured figure of merit of the transmit performance with 0.7 μm piezoelectric layer is about 1.5 1.7 times better than that with 1.2 μm piezoelectric layer.

Difference in Q factor for PMUTs with different radius and thickness is observed and analyzed. Based on [63], the acoustic loss in air is the dominant energy loss mechanism for large radius MUTs and the quality factor from acoustic loss in air $Q_{air} \propto tf$. Q_{air} is modeled and measured in Figure 7.6. For devices with smaller frequency, the Q linear scales with thickness and frequency. The 12 MHz devices with 29 μm radius and 1.2 μm piezoelectric layer did not follow the trend of Q from acoustic loss in air, as the anchor loss starts to dominate
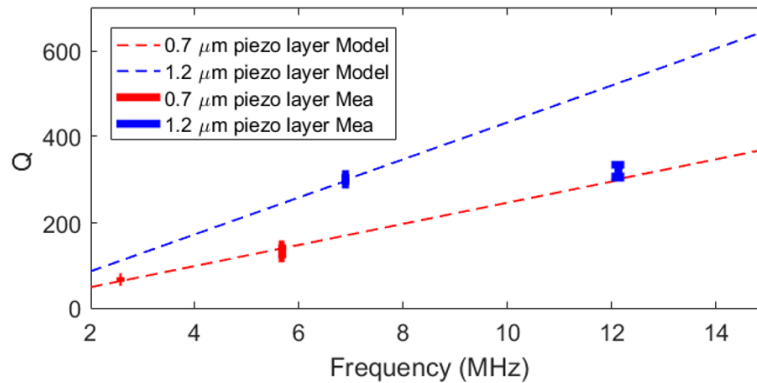
Figure 7.6: Modeled and measured quality factor.

7.3.3 Thickness Scaling Limitation

The limitation of improving AlN PMUT transmit performance via scaling down the total device thickness will be discussed in this session. As explained earlier, at a given frequency, the pressure output of a PMUT array linearly scales with fill factor and transducer displacement. As $w_s \propto 1/t$, the pressure output $P_{ax}(r) \propto FF e_{31,f}/t$. Therefore, the impact of device thickness's scaling on the array fill factor and piezoelectric coefficients need to be discussed. As the piezoelectric layer thickness scales down, the individual circular PMUT's radius will reduce to maintain the frequency, which leads to a decrease in the fill factor with certain minimal spacing requirement from the microfabrication process. Meanwhile, thinner piezoelectric layer will impact the crystal quality of the AlN and therefore the piezoelectric coefficient. For instance, the $e_{31,f}$ will decrease two times when AlN thickness decreases from 1000 nm to 50 nm [62]. Using the piezoelectric coefficient reported for different AlN thickness [62], a transmit performance figure of merit of the circular PMUT array, defined as $FOM_a = FF\ e_{31,f}/t$, can be calculated at 10 MHz for different minimal spacing requirements and piezoelectric layer thicknesses. As shown in Figure 7.7, with no piezoelectric coefficient degradation, there will be about 30 times transmit performance improvement from 1 μm thick piezoelectric layer with 40 μm minimal spacing process to 50 nm thick piezoelectric layer with 5 μm minimal spacing process. Taking account into the current piezoelectric material process capabilities, the FOM_a roughly inversely scales with the piezoelectric layer thickness until being affected by the piezoelectric coefficient degradation below 100 nm thick AlN. While for more than 10 μm minimal spacing requirement, scaling down the piezoelectric layer thickness to below 500 nm can only have less than 1.5 times improvement. Therefore, to take advantage of the thickness scaling below 500 nm thick AlN piezoelectric layer, future process development to fabricate good quality nm thick AlN films with less than 10 μm spaced PMUT array is required.
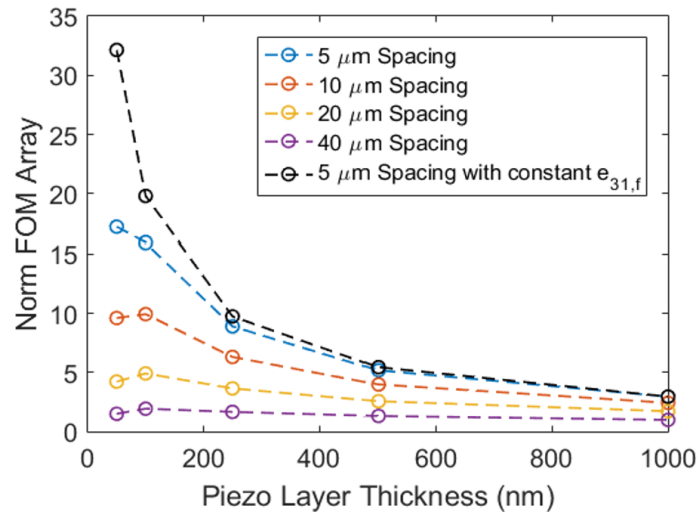
Figure 7.7: Normalized transmit performance of the circular PMUT array versus piezoelectric layer thickness with different minimal spacing requirements.

7.3.4 Conclusion

In this session, simulation and analytical model were used to demonstrate that the axial far field pressure linearly scales with area, fill factor, and transducer peak displacement. The individual PMUT's transmit sensitivity at a given frequency is demonstrated to be inversely proportional to the device thickness. Future process development to fabricate closely spaced PMUTs arrays with good quality nm thick AlN film is required to take advantage of the thickness scaling below 500 nm thick AlN piezoelectric layer.

Chapter 8

Conclusions and Future Works

8.1 Conclusions

This thesis has been focusing on the the modeling and characterization of piezoelectric micromachined ultrasonic transducers (PMUTs) based ultrasonic fingerprint sensors. Analytical model and finite element methods have been demonstrated as a reliable tool to predict the mechanical and acoustic performance. Non-idealities of dense PMUT array, such as mechanical crosstalk, acoustic surface waves, and anchor motion, has been identified for future studies. Scanning laser Doppler vibrometer (LDV) has been proved to be a powerful tool for 2D time domain acoustical and mechanical performance characterization tool. Real-time epidermis and dermis layer fingerprint imaging have been demonstrated. Last but not least, utilizing equivalent circuit model of circular PMUTs at the same resonance frequency in air, PMUT displacement is proved to be inversely proportional to the device thickness. This thickness scaling benefit together with process development for higher fill factor arrays suggest further potential improvement of the pressure output from PMUT arrays.

8.2 Future Works

Piezoelectric micromachined ultrasonic transducers (PMUTs) based fingerprint sensor in this dissertation research has been a continuation of the previous work from our lab [64]. In this dissertation research, PMUT device analysis using equivalent circuit model and acoustic modeling using MatLab k-wave toolbox have been demonstrated to give a good first order estimation of the ultrasonic fingerprint sensor's mechanical and acoustic performance. Specific FEM models will be needed to understand the second order effects' impact on the device performance. Taking advantage of these validated tools, the key performance indicators of the ultrasonic fingerprint sensors,

such as the signal to noise ratio, could be further optimized. Moreover, careful considerations of the PMUT array design, such as the PMUT shape and array spacing, can reduce the identified non-idealities.

The performance of the PMUT array could be further improved utilizing different PMUT device design for better acoustic transduction, thin film piezoelectric material (ScAlN or PZT) for better piezoelectric coefficients, and surface micromachining process for higher array fill factor. With the improved performances from PMUT array, applications taking the full advantage of MEMS technology's benefits (power consumption, size, cost, and complexity) will keep emerging.

Bibliography

[1] Butrus T Khuri Yakub and Omer Oralkan. "Capacitive micromachined ultrasonic transducers for medical imaging and therapy". In: *Journal of Micromechanics and Microengineering* 21.5 (2011), pp. 4004–4014.

[2] P Muralt et al. "Piezoelectric micromachined ultrasonic transducers based on PZT thin films". In: *Transactions on Ultrasonics, Ferroelectrics, and Frequency Control* 52.12 (2005), pp. 2276–2288.

[3] GG Yaralioglu et al. "Calculation and measurement of electromechanical coupling coefficient of capacitive micromachined ultrasonic transducers". In: *Transactions on Ultrasonics, Ferroelectrics, and Frequency Control* 50.4 (2003), pp. 449–456.

[4] Qiming M. Zhang and Jianzhong Zhao. "Electromechanical properties of lead zirconate titanate piezoceramics under the influence of mechanical stresses". In: *Transactions on Ultrasonics, Ferroelectrics, and Frequency Control* 46.6 (1999), pp. 1518–1526.

[5] X. Jiang et al. "Monolithic 591 × 438 DPI ultrasonic fingerprint sensor". In: *International Conference on Micro Electro Mechanical Systems (MEMS)*. IEEE. 2016.

[6] H.-Y. Tang et al. "3D Ultrasonic Fingerprint Sensor on a Chip". In: *Journal of Solid-State Circuits* 51.11 (2016).

[7] J. K. Schneider and S. M. Gojevic. "Ultrasonic imaging systems for personal identification". In: *Ultrasonics Symposium*. IEEE. 2001.

[8] R. M. Schmitt et al. "Ultrasonic imaging of fingerprints using acoustical impediography". In: *Ultrasonics Symposium*. IEEE. 2004.

[9] A. Savoia et al. "Design and fabrication of a cMUT probe for ultrasound imaging of fingerprints". In: *International Ultrasonics Symposium*. IEEE. 2010.

[10] Cheng CH, Ergun A, and Khuri-yakub BT. "Electrical through-wafer interconnects with 0.05 picofarads parasitic capacitance on 400 μm thick silicon substrates". In: *Solid-State Sensors, Actuators, and Microsystems Workshop*. IEEE. 2002.

[11] Anshuman Bhuyan et al. "Integrated circuits for volumetric ultrasound imaging with 2D CMUT arrays". In: *Transaction on Biomedical Circuits and Systems* 7 (2013), pp. 796–804.

[12] J.M. Tsai et al. "Versatile CMOS-MEMS integrated piezoelectric platform". In: *International Conference Solid-State Sensors, Actuators and Microsystems*. IEEE. 2015, pp. 2248–2251.

[13] Y. Lu et al. "Ultrasonic fingerprint sensor using a piezoelectric micromachined ultrasonic transducer array integrated with complementary metal oxide semiconductor electronics". In: *Applied Physics Letters* 106.26 (2015).

[14] B. E. Treeby et al. "Modelling elastic wave propagation using the k-Wave MATLAB toolbox". In: *International Ultrasonics Symposium*. IEEE. 2014.

[15] Paul Muralt. "Piezoelectric Thin Films for MEMS". In: *Integrated Ferrorelectrics* 17 (1997), pp. 297–307.

[16] Klaus Prume et al. "Piezoelectric Thin Films Evaluation of Electrical and Electromechanical Characteristics for MEMS Devices". In: *Transactions on Ultrasonics, Ferroelectrics, and Frequency Control* 54.1 (2007), pp. 8–14.

[17] Doo-Man Chun, Masashi Sato, and Isaku Kanno. "Precise measurement of the transverse piezoelectric coefficient for thin films on anisotropic substrate". In: *Journal of Applied Physics* 113 (2013).

[18] A. Mazzalai et al. "Simultaneous piezoelectric and ferroelectric characterization of thin films for MEMS actuators". In: *International Symposium on Applications of Ferroelectric and Workshop on Piezoresponse Force Microscopy (ISAF/PFM)*. IEEE. 2013.

[19] S. Sivaramakrishnan et al. "Concurrent wafer-level measurement of longitudinal and transverse effective piezoelectric coefficients $(d_{33,f} and e_{31,f}) by double beam laser interferometry$". In: *Journal of Applied Physics* 123 (2018).

[20] Katherine Smyth and Sang-Gook Kim. "Experiment and simulation validated analytical equivalent circuit model for piezoelectric micromachined ultrasonic transducers". In: *Transactions on Ultrasonics, Ferroelectrics, and Frequency Control* 62 (2015), pp. 744–765.

[21] P. Muralt and J. Baborowski. "Micromachined Ultrasonic Transducers and Acoustic Sensors Based on Piezoelectric Thin Films". In: *Journal of Electroceramics* 12 (2004).

[22] D. A. Horsley et al. "Ultrasonic fingerprint sensor based on a PMUT array bonded to CMOS circuitry". In: *International Ultrasonics Symposium*. IEEE. 2016.

[23] David Horsley, Yipeng Lu, and Ofer Rozen. "Flexural Piezoelectric Resonators". In: *Piezoelectric MEMS Resonators*. Ed. by Harmeet Bhugra and Gianluca Piazza. Swizerland: Springer, 2017. Chap. 6, pp. 153–173.

[24] Lawrence E. Kinsler et al. *Fundamentals of Acoustics*. John Wiley and Sons, Inc., 2000.

[25] Abdullah Atalar, Hayrettin Koymen, and H. Kagan Oguz. "Rayleigh Bloch Waves in CMUT Arrays". In: *Transactions on Ultrasonics, Ferroelectrics, and Frequency Control* 61.12 (2014), pp. 2139–2148.

[26] Jinying Zhu and John S. PopovicsFrank Schubert. "Leaky Rayleigh and Scholte waves at the fluid solid interface subjected to transient point loading". In: *Journal of the Acoustical Society of America* 116 (2004).

[27] Greg Wojcik et al. "Time Domain Models of MUT Array Cross-talk in Silicon Substrates". In: *International Ultrasonics Symposium*. IEEE. 2000.

[28] H. Tang et al. "Pulse-echo ultrasonic fingerprint sensor on a chip". In: *International Conference on Solid-State Sensors, Actuators and Microsystems (TRANSDUCERS)*. IEEE. 2015, pp. 674–677.

[29] H.-Y. Tang et al. "3D ultrasonic fingerprint sensor-on-a-chip". In: *International Solid-State Circuits Conference (ISSCC)*. IEEE. 2016.

[30] JN. Reddy. *Mechanics of laminated composite plates Theory and analysis*. CRC Press, 1997.

[31] P. Muralt et al. "Piezoelectric actuation of PZT thin film diaphragms at static and resonant conditions". In: *Sensors and Actuators A: Physical* 53 (1996), pp. 398–404.

[32] W. P. Mason. *Electromechanical Transducers and Wave Filters*. New York, D. Van Nostrand Co., 1948.

[33] Martin Greenspan. "Piston radiator : Some extensions of the theory". In: *Journal of the Acoustical Society of America* 65 (1979).

[34] DA Horsley et al. "Piezoelectric micromachined ultrasonic transducers for human-machine interfaces and biometric sensing". In: *Sensors*. IEEE. 2015.

[35] Y Lu and DA Horsley. "Modeling, fabrication, and characterization of piezoelectric micromachined ultrasonic transducer arrays based on cavity SOI wafers". In: *Journal of Microelectromechanical Systems* 24 (2015), pp. 1142–1149.

[36] Nimrod MT. *Basic physics of ultrasonographic imaging*. Geneva World Health Organization, 2005.

[37] D. T. Blackstock. *Fundamentals of Physical Acoustics*. Wiley-Interscience, 2000.

[38] K. Tsubouchi Mikoshiba. and et al. "Zero-temperature-coefficients saw devices on AlN epitaxial films". In: *Transactions on Sonics and Ultrasonics* 32 (1985).

[39] EH Holder, LO Robinson, and JH. Laub. *The fingerprint sourcebook*. National Institute of Justice, Washington, D.C., 2011.

[40] Y. Lu et al. "Pulse-Echo Ultrasound Imaging Using an AlN Piezoelectric Micromachined Ultrasonic Transducer Array With Transmit Beam-Forming". In: *Journal of Microelectromechanical Systems* 25.1 (2016), pp. 179–187.

[41] I. O. Wygant et al. "An Integrated Circuit With Transmit Beamforming Flip Chip Bonded to a 2D CMUT Array for 3D Ultrasound Imaging". In: *Transactions on Ultrasonics, Ferroelectrics, and Frequency Control* 56.10 (2009), pp. 2145–2156.

[42] X. Jiang et al. "Inter-element coupling effects in pulse-echo ultrasonic fingerprint sensors". In: *International Conference on Micro Electro Mechanical Systems (MEMS)*. IEEE. 2017.

[43] D.-S. Lin et al. "Encapsulation of Capacitive Micromachined Ultrasonic Transducers Using Viscoelastic Polymer". In: *Journal of Microelectromechanical Systems* 19.6 (2010), pp. 1341–1350.

[44] K. K. Park and B. T. Khuri-Yakub. "Dynamic response of an array of flexural plates in acoustic medium". In: *Journal of the Acoustical Society of America* 132 (2012), pp. 2292–2303.

[45] S. H. Wong et al. "Evaluation of waver bonded CMUTs with rectangular membranes featuring high fill factor". In: *Transactions on Ultrasonics, Ferroelectrics, and Frequency Control* 55.9 (2008), pp. 2053–2065.

[46] A. Freedman. "Transient Fields of Acoustic Radiators". In: *Journal of the Acoustical Society of America* 48 (1970), pp. 135–138.

[47] W. L. Beaver. "Sonic nearfields of a pulsed piston radiator". In: *Journal of the Acoustical Society of America* 56.4 (1974), pp. 1043–1048.

[48] R. Tancrell et al. "Near-Field, Transient Acoustic Beam-Forming with Arrays". In: *Ultrasonics Symposium*. IEEE. 1978.

[49] F. Foster and J. Hunt. "The design and characterization of short pulse ultrasound transducers". In: *Ultrasonics* 16.3 (1978), pp. 116–122.

[50] M. C. Ziskin and P. A. Lewin. *Ultrasonic Exposimetry*. CRC Press, 1993.

[51] A. Hanafy and C. Zanelli. "Quantitative real-time pulsed Schlieren imaging of ultrasonic". In: *Ultrasonics Symposium*. IEEE. 1991.

[52] K. K. Shung. *Diagnostic Ultrasound*. CRC Press, 2004.

[53] X. Jiang et al. "Ultrasonic Fingerprint Sensor With Transmit Beamforming Based on a PMUT Array Bonded to CMOS Circuitry". In: *Transactions on Ultrasonics, Ferroelectrics, and Frequency Control* PP.99 (2017), pp. 1–1.

[54] A. Atalar, H. Koymen, and H. K. Oguz. "Rayleigh-bloch waves in CMUT arrays," IEEE Transactions on Ultrasonics, Ferroelectrics, and Frequency Control". In: *Journal of Microelectromechanical Systems* 61.12 (2014), pp. 2139–2148.

[55] Q. Wang et al. "Design, fabrication, and characterization of scandium aluminum nitride-based piezoelectric micromachined ultrasonic transducers". In: *Journal of Microelectromechanical Systems* 26.5 (2017), pp. 1132–1139.

[56] S. Akhbari et al. "Bimorph piezoelectric micromachined ultrasonic transducers". In: *Journal of Microelectromechanical Systems* 25.2 (2016), pp. 326–336.

[57] A. Hajati. "Three-dimensional micro electromechanical system piezoelectric ultrasound transducer". In: *Applied Physics Letters* 101.25 (2012).

[58] G.-L. Luo et al. "High fill factor piezoelectric micromachined ultrasonic transducers on transparent substrates". In: *Solid-State Sensors Actuators and Microsystems (TRANSDUCERS)*. IEEE. 2017.

[59] Q. Wang and D. A. Horsley. "Thickness-Optimized Piezoelectric Micromachined Ultrasonic Transducer Arrays". In: *piezoMEMS Workshop*. IEEE. 2018.

[60] B. T. Eovino. ""Ring shaped and Dual-electrode Bimorph Piezoelectric Micromachined Ultrasonic Transducers"". Ph.D. Thesis. University of California Berkeley, 2018.

[61] G.-L. Luo, Y. Kusano, and H. D.A. Horseley. "Immersion PMUTs Fabricated with a Low Thermal-Budget Surface Micromachining Process". In: *International Ultrasonics Symposium*. IEEE. 2018.

[62] P. Muralt. "AlN Thin Film Processing and Basic Properties". In: *Piezoelectric MEMS Resonators*. Ed. by Harmeet Bhugra and Gianluca Piazza. Swizerland: Springer, 2017. Chap. 1, pp. 3–37.

[63] K. . K. Park et al. "Optimum design of circular CMUT membranes for high quality factor in air". In: *International Ultrasonics Symposium*. IEEE. 2008.

[64] Yipeng Lu. "Piezoelectric micromachined ultrasonic transducers for fingerprint sensing". Ph.D. Thesis. University of California Davis, 2015.